

**THERMAL AND RADIATIVE ENERGY/ EXERGY
ANALYSES OF PARABOLIC TROUGH COLLECTOR
SYSTEMS**

A Dissertation

by

Hayder Noori Mohammed Mohammed

Submitted to the

Graduate School of Sciences and Engineering
In Partial Fulfillment of the Requirements for
the Degree of

Doctor of Philosophy

in the

Department of Mechanical Engineering

Özyeğin University

August 2018

**THERMAL AND RADIATIVE ENERGY/ EXERGY
ANALYSES OF PARABOLIC TROUGH COLLECTOR
SYSTEMS**

Approved by:

Prof. Dr. M. Pinar Mengüç, Advisor,
Department of Mechanical
Engineering
Özyeğin University

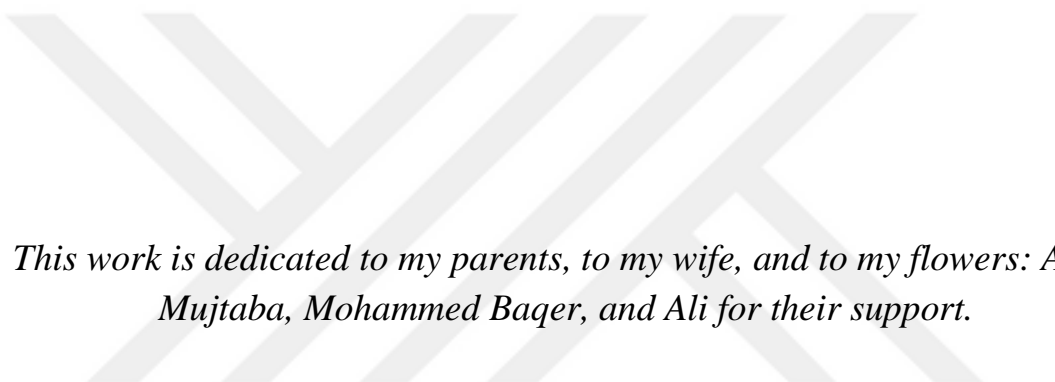
Asst. Prof. Dr.-Ing. Özgür Ertunç,
Department of Mechanical
Engineering
Özyeğin University

Asst. Prof. Dr. Altuğ Başol,
Department of Mechanical
Engineering
Özyeğin University

Prof. Dr. Ali Koşar,
Department of Mechatronics
Engineering
Sabancı University

Prof. Dr. Kurşat Şendur,
Department of Mechatronics
Engineering
Sabancı University

Date Approved: August 2018



*This work is dedicated to my parents, to my wife, and to my flowers: Ayat,
Mujtaba, Mohammed Baqer, and Ali for their support.*

ABSTRACT

The concept of exergy is used to determine the maximum energy that can be extracted from a system. It is based on both the first and the second laws of thermodynamics and allows us to determine the irreversibilities throughout a process and the losses from the system. In this dissertation, the fundamentals of spectral radiative exergy are developed and applied to determine the maximum conversion of solar energy in concentrated solar power (CSP) systems.

There are five primary objectives of this study. First, a new formulation is developed for the maximum efficiency of the solar radiation conversion by considering the radiative energy transfer between two surfaces at different temperatures for a constant volume system. Exergy of spectral radiative transfer is determined, and the formulation for the exergy efficiency maximization is presented in a direct and practical manner. For the calculation of maximum efficiency, the mean temperature of the environment and the sink temperature are used. Second, a new methodology is presented for spectral radiative energy and radiative exergy calculations to evaluate the performances of CSP systems. Spectral radiative properties and the operating temperature of selective surfaces, along with the temperature of the environment, are considered in these analyses. The fundamental quantities needed for the spectral radiative energy and radiative exergy formulations are introduced, and then the spectral performances of five selective coatings are assessed. The spectral analysis is performed in the wavelength range of 250 nm to 20,000 nm, while thermal analysis is carried out for the temperature range of 325 K to 800 K.

The third objective is to introduce a new approach for estimating the exergy value of the monthly average daily horizontal global radiation, including several parameters,

such as the monthly average daily value of the horizontal extraterrestrial radiation, the number of sunny hours, the day length, the mean temperature and the mean wind velocity. Seven statistical parameters are used to validate the accuracy of all models. The concept is applied to four locations in Iraq and Turkey, to help predicting the maximum available solar radiation based on different weather parameters.

The fourth objective is to outline a comprehensive energy analysis for a parabolic trough collector (PTC) system. The analysis considers all heat transfer modes, optical components, and the details of spectral absorption and reflection of solar radiation on the glass envelope. The energy performance of the PTC system is investigated using five gases in an annular space, five selective coatings of the absorber surface, and four common heat transfer fluids following a two-dimensional approach. A model is built using Engineering Equation Solver (EES). The results obtained are compared against the available results from experimental tests and analytical models. This analysis shows the effects of the properties of the absorbing gas, the selective coating and the working fluid on the energy performance of PTC as the key parameters of energy for various operating conditions.

The fifth objective of the study is to establish a methodology to analyze PTC systems using the principles of spectral radiative exergy. The fundamental relations for spectral exergy analyses are derived starting from the first and second law of thermodynamics, and the key performance parameters, including exergy losses, destructions, consumption and efficiency are determined using the same parameters mentioned above in the fourth objective. It is noted that the exergy destruction is directly related to irreversibility throughout processes while the exergy losses are due to the thermal and optical losses. Based on these findings, an improvement of PTC design parameters are discussed.

ÖZETÇE

Ekserji kavramı, sistemlerden çıkarılabilecek maksimum enerjiyi belirlemek için kullanılır. Bu kavram, termodinamiğin birinci ve ikinci yasalarına dayanır, ve bir enerji türünün bir iğere en etkin olarak dönüşümünü belirler. Ekserji, bu sistemlerdeki süreçler ve kayıpların hesaplanmasına yardım eder.

Bu tez çalışmasında beş ana hedef vardır: Birincisi, sabit bir sistem için farklı sıcaklıklarda iki yüzey arasındaki ışımsal enerji transferi göz önüne alınarak, ışımsal ısı transferinin dönüşümünün maksimum verimi için yeni bir formülasyon geliştirilmiştir. Maksimum verimin hesaplanmasında radyasyon transfer kavramının ekserji, güvenilir sonuçların elde edilmesi için ortam sıcaklığının çevre sıcaklığını dikkate alınmalıdır. Formülasyon ekserji verimliliği maksimizasyonu daha doğrudan ve pratik bir şekilde sunmaktadır.

Tezin ikinci amacı konsantre güneş enerjisi (CSP) sistemlerinin performanslarını değerlendirmek için spektral (dalga boyuna bağlı) ışımsal enerji ve ekserji hesaplamaları için yeni bir metodoloji gerçekleştirmektir. CSP analizlerinde spektral ışımsal ısı transferi özellikleri ve ortamın sıcaklığı ile birlikte seçici yüzeylerin çalışma sıcaklığı dikkate alınmıştır. Burada önce temel tanımlar verilmekte, ve bilahare iki gaz, beş seçici kaplamaların spektral performansını değerlendirmek için kullanılmıştır. Birinci yaklaşım için, güneş ve soğurucu yüzey iki kara cisim olarak kabul edilmiştir. İkinci yaklaşım, doğrudan güneş spektral ışımsalından elde edilen verilere dayanmaktadır. Spektral analiz, 250 nm ila 20.000 nm dalga boyu aralığında gerçekleştirilirken, 325 K ila 800 K sıcaklık aralığında da termal analiz gerçekleştirilmiştir.

Üçüncü amaç, atmosfer dışından gelen ışı nım miktarının aylık ortalama günlük değeri, gün boyunca gerçekleşen güneşli saatlerin sayısı, gün sayısı gibi birçok parametre dahil olmak üzere, aylık ortalama günlük yatay küresel radyasyonun ekserji değeri ni tahmin etmek için yeni bir yaklaşım geliştirilmiştir. Tüm modellerin doğruluğunu onaylamak için yedi istatistiksel parametre kullanılmıştır. İki yeni modelin sonuçları, diğer modellerden elde edilen sonuçlardan daha güvenilir bulunmuştur. Irak ve Türkiye'de dört yer için yürütülen bu çalışma, hava durumu parametrelerine dayanarak güneş ışı nımının maksimum kullanılabilirliğini tahmin etmekte yardımcı olacaktır.

Dördüncü ve beşinci amaçlar, hali hazırda kurulu bir parabolik oluklu kolektör (PTC) sistemi için kapsamlı bir enerji ve ekserji analizi gerçekleştirmektir. Bu analizler, detaylı ısı transfer modlarını, optik parametrelerini ve güneş ışı nımının spektral absorpsiyon ve cam zarfı üzerindeki yansımalarını dikkate alarak yapılmıştır. PTC sisteminin enerji ve ekserji performansı, iki boyutlu bir yaklaşımı izleyerek, dairesel bir boşlukta beş gaz, beş seçici kaplama ve dört ısı transfer sıvısı kullanılarak incelenmiştir. Analiz modeli Mühendislik Denklem Çözücü (Engineering Equation Solver, EES) kullanılarak oluşturulmuştur. Elde edilen sonuçlar deneysel testler ve analitik modellerden elde edilen diğer sonuçlarla karşılaştırılmıştır. Bu analiz, gazın, seçici kaplamanın ve çalışma akışkanının PTC'nin enerji ve ekserji performansı üzerindeki özelliklerinin enerji ve ekserji parametrelerinin çeşitli çalışma koşullarında etkilerini göstermektedir. Bu analizler, ilerde benzeri PTC sistemlerinin daha etkin tasarımı ve operasyonu için kullanılabilir olacaktır.

ACKNOWLEDGMENTS

I gratefully acknowledge my advisor Professor Dr. M. Pinar Mengüç for his advice and contributions for providing an encouraging environment throughout the study. He has always assisted and supported me, especially during the difficult times and at the early stages. Through his recommendations and valuable comments, my view on science and research has changed.

I also thank to the Ph.D. Committee Members, Asst. Prof. Dr.-Ing. Özgür Ertunç and Asst. Prof. Dr. Altuğ Başol, as well as to Prof. Dr. Ali Koşar and Prof. Dr. Kurşat Şendur, for their suggestions, which have improved the quality of this dissertation.

I wish to acknowledge the assistance and the financial support of the Ministry of Higher Education and Scientific Research in Iraq.

I would like to express special appreciation for the support from all members of the Centre for Energy, Environment, and Economy (CEEE) of Özyeğin University, especially to Yasemin Somuncu, Dilek Saygi, and Azadeh Didari.

I am indebted to the members of the EU-FP7-BRICKER project, Soltigua staff, especially Luca Ancarani, Energy Efficiency Services staff, especially to Onur Gündürü, and to Asst. Prof. Dr. Yunus Cerci and Asst. Prof. Dr. Atilla Donuk of Adnan Menderes University in Aydın for their diligent help in gathering the data from the CSP system there.

Finally, I extend gratitude to family and colleagues for their help and encouragement during my Ph.D. journey.

TABLE OF CONTENTS

ABSTRACT	i
ÖZETÇE	iii
ACKNOWLEDGMENTS	v
list of tables	x
LIST OF FIGURES	xi
NOMENCLATURE	xv
I INTRODUCTION	1
1.1 Solar Energy	1
1.2 Concentrating Solar Power Systems.....	1
1.3 Motivation for the Dissertation	4
1.4 Outline of the Dissertation	6
II LITERATURE REVIEW	9
2.1 Energy and Exergy.....	9
2.2 Availability of Solar Radiation.....	9
2.3 Exergy of Selective Surfaces for CSP Systems	11
2.4 Global Solar Radiation Exergy.....	13
2.5 Energy Approaches of CSP Systems.....	14
2.6 Exergy-Based Methodology for CSP Systems.....	17
III SPECTRAL ENERGY AND EXERGY EXPRESSIONS FOR RADIATION TRANSFER	20
3.1 Radiative Energy	20
3.2 Relation between Internal Energy and Radiation Entropy	22
3.3 Expression of Maximum Efficiency for Solar Radiation.....	24
3.4 Validations and Comparisons.....	29
3.4.1 The Comparison of Four Formulations for Maximum Radiation Efficiency.....	30
3.4.2 The Effect of Operating Conditions on Maximum Efficiency	31
IV RADIATIVE ANALYSES OF SPECTRALLY-SELECTIVE SURFACES FOR CSP SYSTEMS	34
4.1 Radiative Properties of Spectrally Selective Surfaces	34
4.1.1 Radiative Energy Analysis	35
4.1.2 Radiative Exergy Analysis	38

4.2	Properties of Different Coatings Used for CSP Systems	40
4.3	Results and Discussion	42
4.3.1	Spectral radiative analysis of blackbodies and solar radiation.....	42
4.3.2	Spectral Analysis of the Selective Coatings for the Surface Absorber.....	45
4.3.3	Thermal Analysis for the Selective Coatings	52
4.4	Summary	55
V	SOLAR RADIATION EXERGY AND QUALITY PERFORMANCE FOR IRAQ AND TURKEY	56
5.1	Solar Radiation Exergy Calculations.....	56
5.2	Locations Considered for the Analysis	59
5.3	Statistical Assessment Models	61
5.4	Results and Discussions	64
5.4.1	Maximum Efficiency for Solar Radiation	64
5.4.2	The Empirical Models for Solar Radiation Exergy	67
5.5	Summary	71
VI	THERMAL AND RADIATIVE PERFORMANCE ANALYSES OF A PTC SYSTEM.....	73
6.1	Description of the PTC System.....	73
6.2	Optical Analysis	76
6.2.1	Geometry of PTC.....	77
6.2.2	Solar Radiation Input.....	79
6.2.2.1	Intercept Factor	80
6.2.2.2	The Miscellaneous Loss Factors	81
6.2.2.3	Incident Angle Modifier.....	81
6.2.2.4	Collector Geometric Factor.....	83
6.2.2.5	Optical Efficiency	83
6.3	Energy Analysis	84
6.3.1	Heat Transfer between the Fluid and the Inner Surface of Absorber.....	88
6.3.2	Heat Transfer through the Wall of Absorber.....	90
6.3.3	Heat Transfer through the Annular Space.	91
6.3.3.1	Convection Heat Transfer through the Annular Space	91

6.3.3.2	Radiation Heat Transfer through the Annular Space	94
6.3.4	Heat Transfer through the Glass	95
6.3.5	Heat Transfer between the Outer Surface of the Glass Envelope and the Surroundings	95
6.3.5.1	Convection Heat Transfer from the Outer Surface of the Glass Envelope	96
6.3.5.2	Radiation Heat Transfer from the Outer Surface of the Glass Envelope	97
6.3.6	Thermal Efficiency	101
6.4	Validation of The Numerical Approach.....	102
6.5	Results and Discussions	104
6.5.1	Gases Used in Annular Space.....	105
6.5.2	Selective Coatings of Absorber Surface.....	106
6.5.3	Useful Energy	109
6.5.4	Effect of Heat Transfer Fluids	111
6.5.5	Effect of Operating Conditions.....	113
6.6	Summary	116
VII	RADIATIVE EXERGY PERFORMANCE ANALYSES OF A PTC SYSTEM.....	118
7.1	Exergy Model	118
7.1.1	Exergy Balance for Reflector Subsystem.....	120
7.1.2	Exergy Balance for Receiver Subsystem.....	122
7.1.3	Exergy Balance for PTC.....	127
7.2	Results and Discussion.....	128
7.2.1	Gases Used in Annular Space.....	129
7.2.2	Selective Coatings of Absorber Surface.....	132
7.2.3	Dimensionless fractions of exergy consumption.....	136
7.2.4	Heat Transfer Fluids	138
7.2.5	Operating Conditions.....	140
7.3	Summary	142
VIII	CONCLUSIONS AND RECOMMENDATIONS FOR FUTURE STUDIES.....	144
8.1	Maximum Efficiency for Solar Radiation.....	145

8.2 Radiative Performance of Spectrally Selective Coatings for CSP Systems	145
8.3 The Prediction of Solar Radiation Exergy	147
8.4 Thermal and Radiative Performance of a PTC System.....	148
8.5 Thermal and Radiative Exergy Performance of a PTC System.....	150
8.6 Recommendations Future Works	152
LIST OF REFERENCES	153
APPENDIX A: SURFACE AREAS	159
VITA	161



LIST OF TABLES

Table 3.1 The four formulations of maximum radiation efficiency presented by various researchers [11, 12, 18, 22].	30
Table 4.1 The optical properties of several selective coatings at different temperatures [35, 37, 38, 64]......	41
Table 4.2 Emittance expressions of selective coatings.	42
Table 5.1 Empirical models used in this paper to predict the energy and exergy values of the monthly average daily horizontal global radiation [48, 51, 53, 55].	58
Table 5.2 Location, altitude and data collection period information of the studied sites.....	60
Table 5.3 Regression coefficients of five conventional and present models for four locations studied.....	60
Table 5.4 Statistical parameters of five models for the sites in Iraq and Turkey.	63
Table 6.1 Characteristics and operational limits of PTC model PTMx-36 by Soltigua [108]......	76
Table 6.2 Estimation of the miscellaneous loss factors [64]......	81
Table 6.3 Molecular diameter and molecular weight of suggested gases [121].	93
Table 7.1 Dimensionless exergy fractions of exergy consumption for PTC.....	128

LIST OF FIGURES

Figure 1.1 Schematic of PTC system.	2
Figure 1.2 Receiver and reflector for PTC system (This project is at the campus of Adnan Menderes University, Aydin, Turkey, which was built with the help of the European Union FP7 BRICKER project and manufactured by Soltigua of Italy).	3
Figure 3.1 Radiation incident on a surface [6].	21
Figure 3.2 Schematic to discuss the exergy content of constant volume.	25
Figure 3.3 Comparison of the maximum efficiency values of radiation exergy.	31
Figure 3.4 Effect of environmental temperature on maximum efficiency.	32
Figure 4.1 Schematic of radiative energy flow for a CSP system.	36
Figure 4.2 Spectral reflectance of the various selective coatings [37, 38, 94].	41
Figure 4.3 Spectral radiative energy, spectral radiative exergy and maximum spectral radiative efficiency corresponding to two blackbodies at $T=5800$ K and $T=700$ K.	43
Figure 4.4 Spectral radiative energy and spectral radiative exergy of the direct normal solar spectrum and blackbody radiation at $T=700$ K.	44
Figure 4.5 Spectral radiative energy efficiencies of selective coatings based on blackbody radiation at temperature of the Sun ($T=5800$ K) and operating temperature ($T=700$ K).	46
Figure 4.6 Spectral radiative exergy efficiencies of selective coatings based on blackbody radiation at temperature of the Sun ($T=5800$ K) and operating temperature ($T=700$ K).	46
Figure 4.7 Radiative energy gains of selective coatings based on blackbody radiation at temperature of the Sun ($T=5800$ K) and operating temperature ($T=700$ K).	47
Figure 4.8 Radiative exergy gains of selective coatings based on blackbody radiation at temperature of the Sun ($T=5800$ K) and operating temperature ($T=700$ K).	48
Figure 4.9 Radiative energy and radiative exergy efficiencies of selective coatings based on the data from direct normal solar spectral radiation and operating temperature ($T=700$ K).	49
Figure 4.10 Radiative energy and radiative exergy gains of selective coatings based on the data from direct normal solar spectral radiation and operating temperature ($T=700$ K).	50
Figure 4.11 Emittance curves of the commercial and experimental selective coatings versus operating temperature.	52

Figure 4.12 Radiative energy efficiencies of the commercial and experimental selective coatings versus operating temperature.....	53
Figure 4.13 Radiative exergy efficiencies of the commercial and experimental selective coatings versus operating temperature.....	54
Figure 5.1 Maximum efficiency of average solar radiation (Petela, Spanner, Jeter, and Present Approach, see Table 3.1) at mean temperatures for the site in Karbala, Iraq.	65
Figure 5.2 Maximum efficiency of average solar radiation (Petela, Spanner, Jeter, and Present Approach, see Table 3.1) at mean temperatures for the site in Shatra, Iraq.....	65
Figure 5.3 Maximum efficiency of average solar radiation (Petela, Spanner, Jeter, and Present Approach, see Table 3.1) at mean temperatures for the site in Istanbul, Turkey.	66
Figure 5.4 Maximum efficiency of average solar radiation (Petela, Spanner, Jeter, and Present Approach, see Table 3.1) at mean temperatures for the site in Aydin, Turkey.....	66
Figure 5.5 Estimated and measured exergy values of the global radiation in Karbala, Iraq. (Based on the information provided in Tables 5.1 and 5.3).	69
Figure 5.6 Estimated and measured exergy values of the global radiation in Shatra, Iraq. (Based on the information provided in Tables 5.1 and 5.3).	70
Figure 5.7 Estimated and measured exergy values of the global radiation in Istanbul, Turkey. (Based on the information provided in Tables 5.1 and 5.3).	70
Figure 5.8 Estimated and measured exergy values of the global radiation in Aydin, Turkey (Based on the information provided in Tables 5.1 and 5.3).	71
Figure 6.1 Scheme of the solar field layout at ADU Campus, Aydin, Turkey.....	73
Figure 6.2 A-the connection absorbers, B-the tracking system, and C-the solar field.	75
Figure 6.3 Geometry of parabolic trough collector.	77
Figure 6.4 Incident angle modifier of PTC model PTMx-36 [108].	83
Figure 6.5 Scheme for the heat transfer mechanism through heat transfer collector element.....	84
Figure 6.6 Thermal resistance model for the parabolic trough collector system.	85
Figure 6.7 Schematic side view of the receiver.	87
Figure 6.8 Geometry for PTC for calculation of shape factors and surface areas.	98

Figure 6.9 Radiation network between the right side of glass and both of sky and reflector.	100
Figure 6.10 Useful energy of the PTC system and monthly average temperature for city of Aydin, Turkey throughout the year.	103
Figure 6.11 Comparison of thermal efficiency for present model and the other models.	104
Figure 6.12 Convection losses through annular space for five gases along line of each loop.	105
Figure 6.13 Emissivity of outer absorber surface for five selective coatings along line of each loop.	107
Figure 6.14 Radiation losses through annular space for five selective coatings along line of each loop.	107
Figure 6.15 Outer surface temperature of absorber for five selective coatings along line of each loop.	108
Figure 6.16 Inner surface temperature of glass envelope for five selective coatings along line of each loop.	109
Figure 6.17 Useful energy and components of losses energy along line of each loop.	110
Figure 6.18 The amount and percentage of useful energy and components of losses energy along line of each loop.	111
Figure 6.19 The energy losses (convection and radiation) and pressure losses for four type of heat transfer fluid.	112
Figure 6.20 The thermal efficiency for four heat transfer fluids along line of each loop.	113
Figure 6.21 The useful energy, losses energy, increasing temperature and pressure losses for four inlet temperatures.	114
Figure 6.22 The useful energy, losses energy, increasing temperature and pressure losses for four flow rates.	115
Figure 6.23 The thermal efficiency for four values of wind velocity along line of each loop.	116
Figure 7.1 Exergy balance for receiver subsystem.	119
Figure 7.2 Schematic of exergy balance for the receiver.	123
Figure 7.3 Exergy losses through annular space for five gases along the line of each loop.	130
Figure 7.4 Exergy destruction through annular space for five gases along the line of each loop.	131
Figure 7.5 Exergy consumption through annular space for five gases along the line of each loop.	131
Figure 7.6 Exergy efficiency through annular space for five gases along the line of each loop.	132

Figure 7.7 Exergy losses through annular space for five selective coatings along the line of each loop.....	134
Figure 7.8 Exergy destruction through annular space for five selective coatings along the line of each loop.	134
Figure 7.9 Exergy consumption through annular space for five selective coatings along the line of each loop.	135
Figure 7.10 Exergy efficiency through annular space for five selective coatings along the line of each loop.	135
Figure 7.11 Exergy fraction along the line of each loop.	137
Figure 7.12 The percentages of fraction exergy.	137
Figure 7.13 Exergy consumption s for four types of heat transfer fluid.....	139
Figure 7.14 Exergy efficiency for four heat transfer fluids along the line of each loop.	139
Figure 7.15 Exergy efficiency for four values of temperature along the line of each loop.	141
Figure 7.16 Exergy efficiency for four values of flow rate along the line of each loop.	141
Figure 7.17 Exergy efficiency for four values of solar irradiance along the line of each loop.	142
Figure 8.1 Methodology for the dissertation.	144

NOMENCLATURE

A	Area, m^2
a	Accommodation coefficient; Universal constant, $a = 7.5646 \times 10^{-16} \text{ J m}^{-3} \text{ K}^{-4}$
A_f	Geometric factor,
b	Interaction coefficient,
C	Concentrating ratio; constant
c	Speed of radiation in a vacuum, $c = 2.9979 \times 10^8 \text{ m s}^{-1}$
c_p	Specific heat at constant pressure, $\text{J kg}^{-1} \text{ K}^{-1}$
d	Diameter, m
E	Energy, W m^{-2}
e	Specific energy, J kg^{-1}
Ex	Exergy, W m^{-2}
F	Focal length, m ; shape factor
F_{cyl}	Geometric factor
f	Friction factor,
g	Gravitational constant, m s^{-2}
H	Monthly average daily horizontal global radiation, $\text{W m}^{-2} \text{ day}^{-1}$
h	Planck's constant, $h = 6.626069 \times 10^{-34} \text{ J s}$; convection heat transfer coefficient, $\text{W m}^{-2} \text{ K}^{-1}$; specific enthalpy, $\text{J kg}^{-1} \text{ K}^{-1}$
H_o	Monthly average daily horizontal extraterrestrial radiation, $\text{W m}^{-2} \text{ day}^{-1}$
H_{sc}	Solar constant, W m^{-2}
I	Incident solar radiation, W m^{-2}
L	Length of absorber, m ; entropy intensity, $\text{W m}^{-2} \text{ K}^{-1}$
k	Boltzmann's constant, $k = 1.38 \times 10^{-23} \text{ J K}^{-1}$; thermal conductivity, $\text{W m}^{-1} \text{ K}^{-1}$
$K(\theta)$	Incident angle modifier,
M	Molecular weight, g mole^{-1}
m	Mass flow rate, kg s^{-1}
N	The number of sunny hours, hr day^{-1}
n	The number of the day as counted starting from January 1st, day
N_o	Day length, hr day^{-1}
Nu	Nusselt number,
p	Pressure, Pa
Pr	Prandtl number,
q	Rate of heat transfer, W
R	Thermal resistance, K W^{-1}
R^2	Coefficient of determination,
Ra	Rayleigh number,
Re	Reynolds number,

r	Radius, m
S	Solar radiation input, W; surface areas per unit length, m; Entropy, J K ⁻¹
s	Specific entropy, J kg ⁻¹ K ⁻¹
T	Absolute temperature, K
t_{st}	The t-statistic,
U	Internal energy, J
u	Energy density of radiation, J m ⁻³ ; Kinematic viscosity of the fluid m ² s ⁻¹
V	Velocity, m s ⁻¹ ; volume, m ³
v	Frequency, s ⁻¹ ; kinematic viscosity, m ² s; specific volume, m ³ kg ⁻¹
W	Width of parabolic trough collector, m
z	High, m

Greek symbols

α	Absorptivity,
α_s	Azimuth angle, rad
β	volume expansion coefficient, k ⁻¹
γ	Intercept factor; ratio of specific heats for the annulus gas
Δ	Change,
δ	Solar declination angle, rad; molecular diameter of annulus gas, cm
ε	Emissivity; miscellaneous
η	Efficiency,
θ	Incident angle, rad
θ_z	Zenith angle, rad
λ	Mean-free-path between collisions of a molecule, cm; wavelength, nm
μ	Ratio of molecular weight of gas to molecular weight of absorber surface
ρ	Reflectivity, density
σ	Stefan-Boltzmann constant, 5.669×10^{-8} W m ⁻² K ⁻⁴ ; random error
τ	Transmissivity,
ϕ	Latitude angle, rad
ϕ_m	Acceptance angle, rad
φ_r	Rim angle, rad
ψ	Maximum efficiency,
ω	Hour angle, rad

Subscripts

1	Centerline of fluid stream
2	Inner surface of absorber
3	Outer surface of absorber
4	Inner surface of glass envelope

<i>5</i>	Outer surface of glass envelope
<i>a</i>	Aperture; air
<i>abs</i>	Absorber
<i>amb</i>	Ambient
<i>atm</i>	Atmosphere
<i>b</i>	Beam; blackbody
<i>c</i>	Characteristic
<i>cond</i>	Conduction
<i>cons</i>	Consumption
<i>conv</i>	Convection
<i>eff</i>	Effective
<i>en</i>	Energy
<i>est</i>	Estimated
<i>ex</i>	Exergy
<i>d</i>	Destruction
<i>dir</i>	Direct
<i>f</i>	Fluid
<i>g</i>	Glass; gas
<i>gain</i>	Gain
<i>in</i>	Inlet
<i>l</i>	Loss
<i>mes</i>	Measured
<i>op</i>	Optical
<i>out</i>	Outlet
<i>r</i>	Rim
<i>rad</i>	Radiation
<i>rec</i>	Receiver
<i>ref</i>	Reflector
<i>s</i>	Solar; surface
<i>sky</i>	Sky
<i>st</i>	Standard
<i>t</i>	Total
<i>th</i>	Thermal

Abbreviations

BR	Blackbody radiation
CSP	Concentrated solar power
ECU	Energy conversion unit
EDU	Energy distribution unit

EES	Engineering Equation Solver
EGU	Energy generation unit
HCE	Heat collector element
HTF	Heat transfer fluid
MABE	Mean absolute bias error
MAPE	Mean absolute percentage error
MBE	Mean bias error
MPE	Mean percentage error
NREL	National Renewable Energy Laboratory
PLC	Programmable logic controller
PTC	Parabolic trough collector
UVAC	Universal vacuum collector



CHAPTER I

INTRODUCTION

1.1 Solar Energy

One of the current challenges in today's world is to find alternative and renewable energy sources to meet growing global energy demands [1, 2]. At the same time, there is a pressing need to protect all our resources which naturally puts more emphasis on energy efficiency. The Sun is the obvious source for energy, yet its effective use requires advanced technologies, including energy conversion and storage systems, which need to be further advanced to be compatible with solar energy requirements [3]. The amount of solar energy that arrives at the surface of the Earth every hour is greater than the total energy consumed by the world population over the entire year [4]. The solar energy flux incident on the Earth's surface can be further enhanced by using concentrating technologies, which utilize more sophisticated materials [5]. It is obvious that any effort to use solar energy will have a long-lasting impact to the energy problem we face, and the CSP systems are among the best candidates to achieve the goal of clean and renewable energy at many parts of the World.

1.2 Concentrating Solar Power Systems

In future applications of solar energy conversion, new technological improvements are necessary [1]. In the CSP systems, after solar radiation is incident on a surface, it is partially absorbed by the spectrally selective surfaces. This thermal energy is transferred to heat transfer fluid at high temperature, which is then used in conventional power cycles based on steam or organic fluids to generate electricity [2].

To concentrate solar radiation, most systems use glass mirrors, which continuously follow the path of the Sun [3]. A schematic of one of these systems is a PTC system as shown in Figure 1.1.

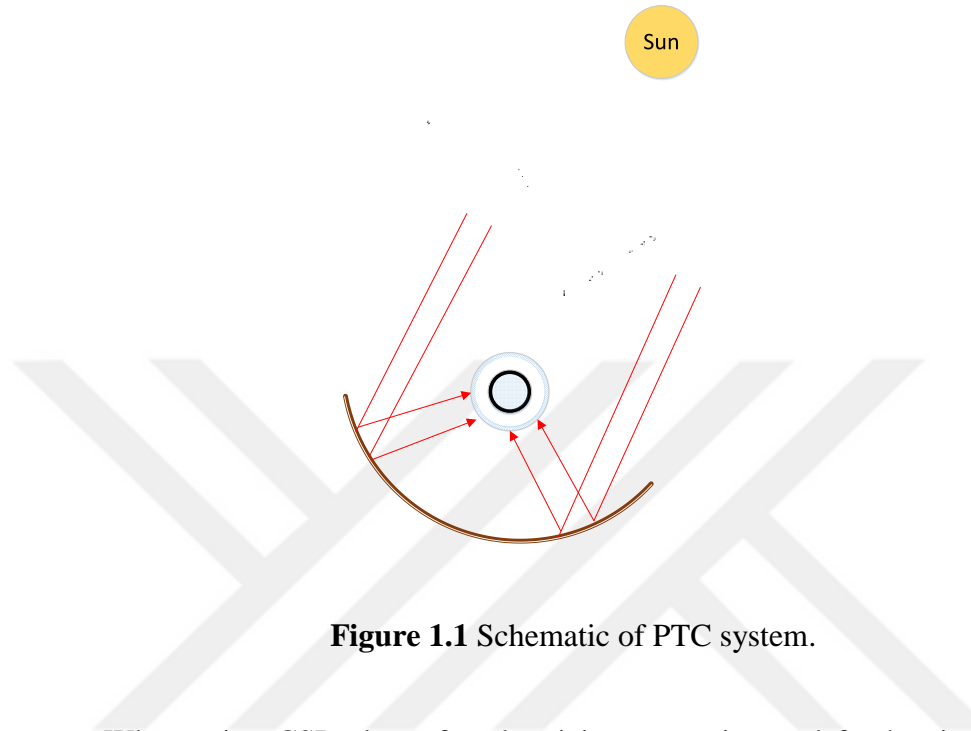


Figure 1.1 Schematic of PTC system.

When using CSP plants for electricity generation and for heating/cooling, its components and subsystems in the power plant should be considered in tandem to optimize the conversion of the solar energy to other energy forms [4]. In CSP systems, the incident solar radiation can be concentrated on a receiving surface to achieve twenty to one hundred times of the influx of Sun's energy. This enhanced radiative energy is transferred to a heat transfer fluid (HTF) in an absorber tube [5]. The thermal energy obtained at high temperatures is usually used for electricity generation through conventional conversion processes. Thermal power plants use thermodynamic cycles, such as a Rankine cycle, which is a heat engine.

One of the most important parts of the solar plant is the PTC, that is a parabolic trough collector. The fundamental principle governing the capturing of solar energy states that when the radiation from the sun hits a PTC, a tracking mechanism is operated

to rotate the PTC and follow the sun. Aluminum or thin silver coatings are generally applied to the mirrors. Their reflectivity is mainly dependent on the surface properties, which is also affected by the decomposition, the growth or polishing process during installation. Aluminum has an 88% reflectivity, whereas silver can have 98% reflectivity [6, 7].

Concentrating solar radiation reduces the surface area of the absorber with respect to the aperture area, thereby generating a temperature of approximately 400°C at the wall of the absorber [8]. An absorber is usually covered with a solar evacuated glass envelope to deal with the energy loss to the ambient. The absorber is fabricated from materials with high thermal conductivity, such as aluminum or stainless steel. It is coated with a selective coating for high absorption within the range of the solar radiation wavelengths. Figure 1.2 gives an example of the receiver and the reflector.



Figure 1.2 Receiver and reflector for PTC system (This project is at the campus of Adnan Menderes University, Aydin, Turkey, which was built with the help of the European Union FP7 BRICKER project and manufactured by Soltigua of Italy).

1.3 Motivation for the Dissertation

Global energy consumption has been increasing more rapidly than the population growth. Moreover, the use of fossil fuels causes a significant amount of CO₂ emission to the atmosphere, which exerts a negative influence on the climate change problem [9]. Therefore, exploring alternative energy sources, systems, and technologies for sustainable development is important to find substitutes for conventional energy sources and thus to mitigate their negative effects [10]. In addition to their ecological benefits, renewable sources present valuable economic alternatives in the long run. Many areas of the world have abundant and free solar energy [4]. Solar energy is more dominant than all the other renewable energies and the energy generated from fossil fuels, combined [6].

However, it is important to determine the economical viability of any CSP system. This necessitates to determine how much work potential is available from solar radiation and what fraction of it can be extracted as useful work. Although several studies have discussed the maximum radiative efficiency, none of these studies have reported an approach that includes the temperature of the environment in energy terms in order to obtain an expression for maximum efficiency. Also, one of the major obstacles for the maximum efficiency expressions given by Spanner [11] and Jeter [12] is that they consider a piston-cylinder system to verify their results. Since most real systems are not represented by piston-cylinder models, significant uncertainties may result in the actual application of the available exergy models.

In CSP systems, or in any solar energy system for that matter, spectral analysis of radiative transfer is essential. Such spectral analysis should also be extended to exergy calculation methodologies. In order to quantify the ability of a surface to convert

absorbed spectral solar energy to other forms of useful energy, we must introduce the concept of spectral radiation exergy. None of the previous studies have considered the impact of spectral radiative properties when analyzing a spectral selective surface. In addition, the temperature difference between a selective coating surface and the environment is usually much less than the temperature difference between the Sun and the environment. Proper use of the environmental temperature is needed to determine the maximum spectral radiative efficiency, which has not been done to date.

For solar radiation absorption estimations in CSP systems, empirical models cannot be used reliably because of their low accuracy and their neglect of changing weather conditions. The daily mean temperature, and daily mean wind velocity are the two parameters of weather that play an important role in predicting the energy and the exergy of global radiation and should be accounted for in the analysis. In energy analysis, the reflected radiation on the outer surface of the absorber and the inner glass surfaces are usually neglected. In addition, the effects of radiation transfer between the receiver, the reflector and the sky are omitted. A new analysis should include these details as well.

Finally, although exergy analysis has been extensively conducted in studying the performance of a PTC, no studies are available for evaluating exergy performance, including the details of all components. In addition, the effects of modern working fluids, selective coatings of the absorber, and gases in the annular space are not considered. Moreover, most analyses used for PTC are usually based on one-dimensional models. Limited research exists on comprehensive two-dimensional analyses, which considers pressure drop in the HTF, or PTMx types of PTCs.

1.4 Outline of the Dissertation

Following, is a brief outline of the Dissertation. In Chapter 1, a general review of solar energy and concentrating solar power technologies are presented. The reasons for studying the energy and exergy approach in solar systems are also outlined.

The literature review is given in Chapter 2. Several approaches are investigated for the calculations of the maximum energy that can be extracted from a system efficiency. The exergy concept is used to assess the quality of system. Most studies are available in the literature which discussed in the performance of the selective coatings, prediction of global solar radiation, and the energy and exergy PTC models.

Chapter 3 outlines a new formulation of maximum efficiency derived by considering the radiative energy transfer between two surfaces at different temperatures for a constant volume system. The exergy of the system, which can be produced by a change in internal energy and entropy, can be transformed into useful work. Maximum efficiency can be determined by using the definition of efficiency based on the second law of thermodynamics. The formulation for the exergy efficiency maximization is presented in a direct and practical manner. The change in internal energy due to radiation transfer is also considered.

Chapter 4 presents a new methodology for radiative energy and radiative exergy analyses that include the effect of spectral radiative properties for different coatings. In the literature, the spectral radiative exergy analysis of selective surfaces has not been carried before. Furthermore, in most analyses, only the energy emitted from a source such as blackbody radiation is discussed and most analyses omit the energy emitted from the sink in the calculations. This omission can be justified only in cases where a relatively small temperature difference exists between the selective coating surface of the absorber

and the environment. The work presented here provides the necessary foundation to advance the understanding of the concept of quality when converting solar energy into useful work.

Chapter 5 presents a new approach for estimating the exergy value of the monthly average daily horizontal global radiation, including many parameters, such as the monthly average daily values of the horizontal extraterrestrial solar radiation, the number of sunny hours, the length of the day when the sun is shining, the mean temperature, and the mean wind velocity. These data obtained for four locations in Iraq and Turkey. The results of such an analysis help in predicting the maximum availability of global solar radiation based on detailed weather parameters.

In Chapter 6, the presented model is investigated to analyze radiation and convection heat transfer in an actual PTC system. The model is applied to a specific solar field of PTMx-36 concentrating solar collectors at the campus of Adnan Menderes University, Aydin, Turkey, which was built with the help of the European Union FP7 BRICKER project [13]. This project was coordinated by Acciona of Spain, and the PTC system and PTMx-36 solar collectors were manufactured by Soltigua of Italy [14]. The Turkish part of the project was coordinated by the Center for Energy, Environment, and Economy (CEEE), Özyeğin University, Istanbul, and the project was carried out with CEEE, along with Onur Energy, Izmir, and Adnan Menderes University, Aydin, both in Turkey.

The energy analysis considers the solar radiation received by all components of PTC, including the absorber and the glass envelope. The performance of the PTC system is conducted using a two-dimensional model with detailed correlations. Moreover, the model employs detailed spectral reflective properties of coatings and the temperature-

dependent values of radiative emissivity/absorptivity. These details are considered to provide practical results to specify the actual performance of the PTC system under working conditions.

In Chapter 7, the model introduced in Chapter 6 is used to give a comprehensive exergy analysis based on a two-dimensional approach. The exergy analysis considers the solar radiation received by both the absorber and the glass envelope. The key performance parameters, including exergy consumption, losses, destructions and efficiency, are evaluated. Moreover, different operating parameters are considered using a two-dimensional approach, including five gases in the annular space, five selective coatings of absorber surfaces, and four working fluids, for various operating conditions.

Finally, the findings of this dissertation are summarized, and the recommendations for future studies are presented in Chapter 8.

CHAPTER II

LITERATURE REVIEW

2.1 Energy and Exergy

One of the evaluation criteria for the performance of thermal processes is the exergy analysis. Along with the energy analysis, exergy calculations provide a clear and highly effective understanding of the performance of a system. The quantity of system is obtained by energy approach, whereas the exergy approach can be evaluated by the quality of the system. Exergy analysis cannot substitute the energy analysis, but it considers a significant approach as a complementary tool to determine the useful work and unrecoverable losses, that can lead to improve the system. When analyzing such systems, exergy analysis is highly appropriate for studying the quality of the conversion of solar to thermal energy

In such complex systems, the concept of exergy is employed to determine the maximum energy that can be extracted from a system based on the first and the second laws of thermodynamics [15]. Exergy is directly related to irreversibilities throughout processes and the losses from the system [16]. Along with energy analysis, exergy calculations provide a clear and highly effective understanding of the performance of a system [17].

2.2 Availability of Solar Radiation

There are various approaches to specify the availability of solar energy which are based on the second law of thermodynamics and the entropy/exergy analysis [12, 18-22]. However, exergy transfer by thermal radiation has still not been formulated in detail and

unambiguously for complicated systems. Heat transfer textbooks usually take into account heat transfer by three modes conduction, convection, and radiation, but these procedures do not adapt into consideration exergy transfer from solar energy.

The analysis of solar radiation by using the exergy approach has the potential to show how much energy can be converted to work effectively [23]. Petela [18] one of the original researchers who outlined the formulation for the exergy of heat radiation. He expressed that the ratio of exergy to energy from radiation is directly proportional to the exergy of a substance and its temperature. He also briefly highlighted the potential applications of the impact of radiation energy on exergy analyses.

Parrott [19] presented the analytical upper bound expression for the efficiency of solar energy conversion. In this case, the theoretical expression for optimum useful work from solar energy was computed with respect to the directional solar radiation. Jeter [12] has demonstrated the optimal conversion of solar power and evaluated the performance. The solar radiation is assumed to be constant, and the exergy of the systems was computed accordingly. He also showed that the steady flow rate was constrained by the constant temperature value used in the analysis.

When all the exergy is properly converted to work, it is possible to reverse the work flow; then, it is possible to obtain the optimum extraction work from the thermodynamic viewpoint. Gribik et al. [20] presented a controversial analysis for the second law of solar power conversion by drawing conclusions on the correct expression resulting from Spanner. Based on this method, he proposed a generalized thermodynamic expression. With the reflection taken into account, the fall in exergy efficiency due to the atmospheric scattering was also presented.

Wright et al. [21] presented a concise and simpler analysis of the problems to explain the concept of exergy analysis when dealing thermodynamic systems where the radiative heat transfer is dominant through the use and proper application of the general exergy balance equation. The results show that Petela's thermodynamic approach, which is applicable for the exergy flux of blackbody radiation (BR), provides the upper bound performance for the conversion of solar radiation (SR) through (BR) estimation. Petela [22] also derived an expression for the study exergy of solar radiation for three groups and discussed the details. The formulation was improved for the understanding of exergy analysis of solar radiation and included the discussion of the formulas by the Petela, Spanner, and Jeter with analysis of thermal radiation under specific conditions. Their proposed expressions relied on models that involved a system of radiating surfaces on which emission and absorption were occurring.

2.3 Exergy of Selective Surfaces for CSP Systems

To utilize concentrated solar energy, a receiver or absorber tube is fabricated from steel which is covered with a spectrally selective coating; this coating must have high absorption capabilities for irradiation within the solar spectrum [2]. The transport phenomena in these complex systems is dominated by the radiative heat transfer, which necessitates a more thorough analysis than the conventional approaches. CSP systems are expensive, and any small improvement in their performances can easily be justified [6]. Here, we present a new analysis based on the definition of spectral radiative exergy. As we show below, this approach can allow us to evaluate the radiative performance of the coatings of the CSP mirrors in a more clear way.

For CSP systems, the most critical spectral range for the absorption of solar radiation is between the wavelengths of 300 nm to 2500 nm. As expected, the maximum

absorption can be obtained by a blackbody [6, 24]. However, for the maximum efficiency of a CSP system, we do not want the tubes to emit energy at longer wavelengths. Therefore, the emissivity of these surfaces at longer wavelengths should be very low. This can be obtained by using spectrally selective surfaces. For a typical surface used in a practical CSP system, the power gain is always less than that for an ideal selective surface [25]. Preferred surfaces should have high reflection particularly at wavelengths greater than 2500 nm to ensure that the infrared absorption/emission is low, which yield reduced energy loss and exergy destruction [6].

Radiative exergy was originally formulated as an expression for an arbitrary spectrum of electromagnetic radiation by Karlsson, who applied it to a blackbody [26]. Candau proposed an optimal efficiency expression for convertible solar radiation and applied it to a simple grey surface [27]. A detailed formula was introduced by Petela to determine the radiative effectiveness of a grey surface [28]. Wien et al. derived an exergy formula by using statistical thermodynamics, demonstrating that it corresponds to an expression based on classical thermodynamics [29].

Spectral radiative analysis of the selective coating surface is important when researching these materials to achieve higher absorptivity in solar radiation wavelength range, and higher reflectivity in the infrared range, thus decreasing emission losses. A large body of research studies is available about coatings used in CSP systems [30-34]. Several studies have investigated potential improvements in the performance of selective coating properties, such as optical and energy efficiency, durability against environmental conditions, cost of materials and operational stability at a range of temperatures [35, 36]. Some attempts have also been made to develop efficient coatings that remain stable at temperatures of more than 450°C [37, 38], while Zheng et al.

demonstrated the importance of the volume fractions of layers to optimize the performance [39]. Ning et al. developed a novel coating which has high absorptivity and low emissivity at 500°C [40].

Using a spectral beam splitter approach, Hu et al. have performed radiative energy and radiative exergy analyses to determine the optimal wavelength and operating temperature for selective coatings [41]. Using the same approach, exergoeconomic analysis has been applied to combined systems [42].

2.4 Global Solar Radiation Exergy

In solar power plants, the local solar radiation data are significant in designing a solar energy conversion system. The averages of hourly, daily, and monthly measured solar radiation are mainly available from many national agencies and can be considered in the analysis [43]. However, such detailed data remains scarce because of the high initial and running costs of weather stations and the restrictions due to local variations [44]. The solar radiation data may also be questionable if the solar energy systems are built far away from the measurement stations [45]. For solar radiation estimations, many studies have used alternative solutions to obtain different empirical models based on the available data [46].

In the literature, several empirical models to obtain global solar radiation have relied on the horizontal extraterrestrial radiation, the number of sunny hours, and the day length, without taking into account other parameters of weather such as the environment temperature and the wind velocity.

One of the first solar radiation models was developed by Angstrom [47], which was linear in nature. Prescott subsequently modified the empirical model of Angstrom

for more details [48]. For Turkey, the empirical coefficients of the Angstrom–Prescott model were reported by Tiris [49]. Page presented the coefficients of a linear model, which could be applied anywhere on the Earth [50]. Ögelman and Ecevit correlated in a second-order polynomial form [51], and later Akinoğlu and Ecevit obtained a solar radiation model for Turkey using a second-order polynomial equation [52]. A third polynomial model was developed by Bahel [53]. Later Samuel estimated the empirical coefficients of Bahel’s equation for Sri Lanka [54]. We must also mention that the only paper for calculations of the exergy value of solar radiation was based on the Angstrom–Prescott approach and was given for Turkey [55].

2.5 Energy Approaches of CSP Systems

The ultimate goal of a small-scale CSP plant is to maximize the conversion of solar energy to thermal energy [8]. The thermal energy obtained at high temperature is then used for direct and indirect applications. Direct applications include industrial heating and air conditioning systems, and indirect applications include conversion processes for electricity generation systems based on a thermodynamic cycle [10].

A small-scale solar plant with ORC was previously studied when the performance of the solar ORC system for different types of working fluids for single- and dual-stage system architectures were considered [56]. Also, a performance analysis was presented for a solar-powered ORC system with a compound parabolic collector based on off-design conditions [57]. A novel small-scale configuration scheme was proposed for CSP with built-in ORC for industrial applications [58]. On the basis of simulations, performance evaluation was conducted for a solar power plant with two different cycles, based on oil or steam as a working fluid [59]. Another study was compared between different models of solar collectors. Where water, steam or molten salt was used as a

working fluid. However, thermal oil is so far the most widely used fluid, as reported in [5].

Given the fluctuation in the solar radiation, building a collector field that can produce more energy than the capacity of turbine under normal conditions is important. The surplus of the energy entering the turbine can be channeled to charge the storage system. This system can be used as the energy source provider when solar radiation is deficient [60]. Several studies reported details for improvements in the performance of the spectrally selective coating surface, such as efficient solar- thermal conversion, resistance against environmental conditions, cost of coatings and stability at operating temperature [6].

Researchers have shown that the performance and the thermal stability for new coating can be improved above 450°C [37, 61]. A number of other studies suggest the association of coating, thereby showing the importance of the volume fraction of particles in layers in optimizing the performance of selective coating surface [39]. Investigators recently examined a novel coating and found high absorptance and low emittance at 500°C [40]. Which is very important for spectral performance of coating.

The objective of a PTC is to convert solar energy to thermal energy and channel it to HTF. The performance of any HTF depends on the equilibrium of energy between HTF and the surroundings [62]. The analysis of a PTC system is performed in two steps. The first step is the optical analysis to compute radiation gain and optical losses. The second step is the energy analysis to deliver useful energy and energy losses. In optical analysis, the optical performance of all components of a PTC system is evaluated. Under ideal case, the incident solar radiation should be totally absorbed by a receiver.

However, in actual status, the receiver does not absorb all incident solar radiation due to several factors, such as tracking operation, geometric imperfection and because of the real optical properties of surfaces. Thus, the optical analysis is necessary to calculate the optical efficiency, which is defined as the ratio of solar energy that reaches the receiver to the incident on the collector [63]. For energy analysis of the PTC, the absorbed energy by HTF and the energy losses from a heat collector element (HCE) to the surroundings need to be determined [2]. The energy balance model has two main parts. One is the advantageous heat as a useful energy to working fluid, and the other is disadvantageous heat as an energy loss from a HCE.

The National Renewable Energy Laboratory approach is commonly used in studying the performance of PTC system [64]. Wang presented a well-detailed literature survey on commonly used solar collectors and highlighted their respective applications [65]. A comparative analysis on the benefit and drawback of collectors is firstly performed [66]. A system model for the analysis of heat transfer in a PTC system was also proposed and used to validate the experimental results with the theoretical results [67]. The underlying mathematical model for a PTC system is developed so that the system performance can be evaluated and system parameters can be defined. A graphical user interface built using the VB.NET software tool is also employed to control these parameters and observe their impact on the PTC system performance [68].

Another work was evaluated the thermal and optical efficiencies of PTC solar field on the basis of instantaneous data collection. Results reveal a significant improvement in optical efficiency [69]. Several studies have assessed the performance of PTC, but certain drawbacks are associated with the published methodology [2, 5, 62, 67].

2.6 Exergy-Based Methodology for CSP Systems

The exergy analysis can have a crucial purpose when analyzing CSP systems in specifying the ability of the systems to convert solar energy into other forms of useful energy. In the literature, one can find a number of studies PTC systems; the most relevant ones will be briefly highlighted here.

In one of these studies, the use of nanoparticles (carbon nanotubes) within the working fluid (Therminol-VP1) as a nanofluid is explored [70]. Using a computational fluid dynamics (CFD) approach, the exergy efficiency of PTC was determined for different wind velocities was found to be inversely proportional to the wind velocity [71]. Another study has explored the importance of the concentrating ratio and operating conditions for PTC performance optimization; the CFD approach is used to determine optimum conditions [72]. Two other studies reported the exergy performance of PTC and discussed the advantages and drawbacks associated with using nanoparticles [73, 74].

Performance analysis was also presented for a solar power system based on supercritical carbon dioxide used, and various design and operating conditions were considered [75]. Using the same working fluid, the analysis was also expanded to different values of pressure and temperature [76]. Another work was performed the energy and the exergy analyses of a PTC system to examine the experimental results against the theoretical results [77]. Several models based on the energy and exergy analysis have been considered, including a comprehensive approach for the analysis and evaluation of a PTC receiver by considering conduction, convection and radiative heat transfer in tandem. The mathematical model was validated with existing data results and applied to assess the thermal performance of a PTC system [78]. In another study, a comprehensive thermal model for the exergy analysis and the evaluation of a PTC

receiver was discussed recently by considering liquid (Therminol-VP1) and gas (air) as heat transfer fluids (HTFs). This model was validated against the available results from the literature and used to evaluate the performance analysis of the PTC. The results showed that exergy destructions were more significant in the liquid case, whereas the exergy losses were more valuable in the gas case [79].

Another work evaluated the performance analysis in terms of the energy and exergy efficiencies of PTC using a genetic algorithm. These efficiencies at the output of the system were optimized based on the average temperatures of the working fluid and the absorber wall. The exergy efficiency was found to be proportional to these parameters [80]. A detailed exergy performance analysis of the combined thermal power plant was investigated using Rankine and organic Rankine cycle (ORC) coupled with a PTC system. Seven distinct refrigerants were considered in evaluating the exergy performance. The results showed that the refrigerant R134a had the optimum exergy performance, followed by R152a. However, the refrigerant R600a presented the lowest exergy performance for the combined cycle system [81].

Kalogirou et al. presented a brief literature survey on the exergy analysis of solar thermal systems, covering the types of solar collectors, solar thermal system, and their respective implementations and processes [82]. Parameters, such as inlet temperature, mass flow rate, and solar irradiance with or without vacuum in the annulus space in the presence of wind, were used to evaluate system performance. Results showed the system considered, the effects of wind speed and mass flow rate were relatively small [83].

The hourly solar radiation to evaluate the performance analysis of CSP systems is important for the calculation of the exergy efficiency. Usually, the exergy efficiency is determined at the output of the system using the inlet temperature. The parameters

used in the performance evaluation increase with the increase of solar intensity [84]. A detailed analysis based on the energy and exergy performance of a direct steam generation system with a PTC was presented and validated against the experimental results, and the optimum design parameters were investigated [85].

In the literature, a novel configuration has been proposed for small-scale CSP with a built-in ORC in industrial applications. This configuration is built by feeding the power block, which is used for charging the thermal storage unit. It considers all factors, including the meteorological aspects of the site, the constraints due to the control operations, and a realistic load profile. The findings reveal that the direct feeding storage configuration is more reliable in terms of storage size compared with the conventional configuration. Moreover, the exergy and energy efficiencies of the thermal storage system improve with the decrease of solar radiation. The energy and exergy efficiencies are degraded to increase in incident solar radiation; however, the performance of the system can be improved by transforming waste heat into a heat source [58].

Alternative designs were considered for the configuration of the heat collector element, to improve the performance of a PTC system, including a novel cavity absorber for a PTC [86]. The model was validated against the experimental results, and found that the bulk temperature of the HTF could reach 570 K. Another study proposed a new design of a PTC based on pump and thermosiphon systems. The design was experimentally examined, and the performance of PTC was assessed by estimating the energy and exergy efficiencies. The maximum exergy efficiency was found for 70°C [87].

CHAPTER III

SPECTRAL ENERGY AND EXERGY EXPRESSIONS FOR RADIATION TRANSFER

3.1 Radiative Energy

Radiation intensity is characterized by the rate in which emitted energy in the way per unit area normally does this orientation and per unit solid angle as [6]:

$$I = \frac{dq}{dA \cos \theta_z \sin \theta_z d\theta_z d\alpha_s} \quad (3.1)$$

where I is the radiation intensity expressed as the rate of radiant energy emitted in (θ_z, α_s) per area normal to the direction and per unit solid angle about this orientation. q is the rate of radiant energy, dA is the differential area element of the surface, the zenith angle, θ_z is the angle formed by incident ray and the surface normal, α_s is the azimuth angle, as shown in Figure 3.1.

One of the assumptions made in most solar radiation analyses is that scattering and absorption can be neglected in the medium between the sun and the receiving surface [20], meaning that the solar intensity remains constant until it is incident on a surface.

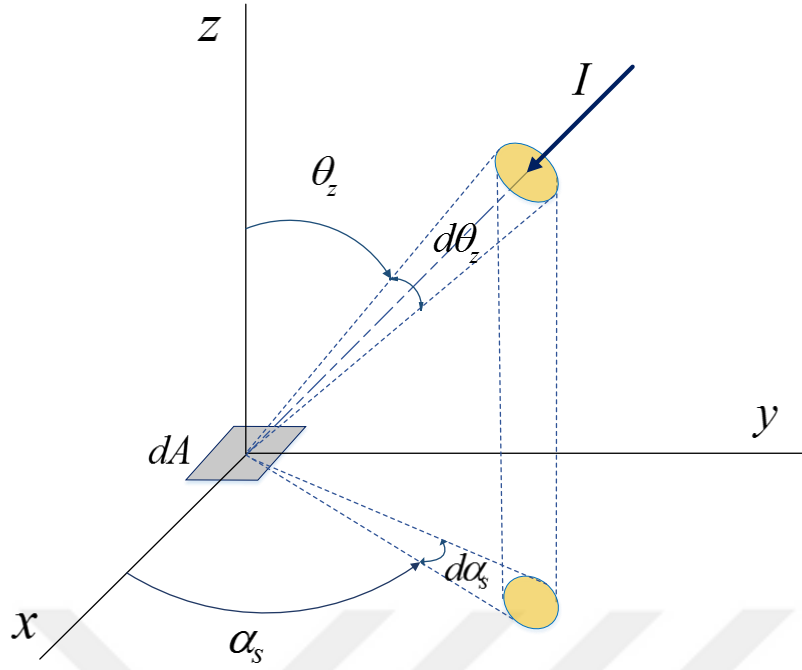


Figure 3.1 Radiation incident on a surface [6].

Radiative energy incident on a surface is defined as [6]:

$$dE = \frac{dq}{dA} = I \cos \theta_z \sin \theta_z d\theta_z d\alpha_s \quad (3.2)$$

If the radiation is isotropic, then the radiation intensity is constant in any direction. In this case, the integration of radiative energy over a hemisphere above the surface point can be computed by the following equation [6]:

$$E = \int dE = \int_0^{2\pi} \int_0^{\pi/2} I \cos \theta_z \sin \theta_z d\theta_z d\alpha_s = I \int_0^{2\pi} \int_0^{\pi/2} \cos \theta_z \sin \theta_z d\theta_z d\alpha_s = I\pi \quad (3.3)$$

A universal constant can be calculated by [88]:

$$a = \frac{8\pi^5 k^4}{15c^3 h^3} = 7.5646 \times 10^{-16} (Jm^{-3} K^{-4}) \quad (3.4)$$

where, c is known as the speed of radiation in a vacuum, h is the Planck's constant, and k is the Boltzmann's constant. Thus, the Stefan–Boltzmann constant can be expressed in terms of this universal constant and the speed of radiation in vacuum [88],

$$\sigma = \frac{1}{4}ac \quad (3.5)$$

3.2 Relation between Internal Energy and Radiation Entropy

In internally reversible processes, the differential expression of the second principle of thermodynamics in a closed system is the sum of the energy radiation and energy of bodies, which is assumed to remain constant. This expression is also known as the Gibbs equation [88]:

$$TdS = dU + pdV \quad (3.6)$$

where T , S , U , p , V represent to the temperature, the entropy, the internal energy, the pressure, and the volume, respectively.

The change in entropy can be obtained by dividing the Eq. (3.6) on the temperature as:

$$dS = \frac{dU + pdV}{T} \quad (3.7)$$

The internal energy as a function of temperature and volume can be considered as follows:

$$U = f(T, V) \quad (3.8)$$

The partial derivative of the internal energy can be applied to a change in the entropy equation, and it can be written as:

$$dS = \frac{1}{T} \left(\frac{\partial U}{\partial T} \right)_V dT + \frac{1}{T} \left(\frac{\partial U}{\partial V} \right)_T dV + \frac{pdV}{T} \quad (3.9)$$

The entropy equation can be applied at constant volume:

$$dS = \frac{1}{T} \left(\frac{\partial U}{\partial T} \right) dT \quad (3.10)$$

For the radiation of a black surface, a certain amount of energy at constant volume, undergoes a small change in energy δU . Hence, from equation above, the change in entropy can be computed [88]:

$$\frac{\delta S}{\delta U} = \frac{1}{T} \quad (3.11)$$

The entropy includes all the entropies of the monochromatic radiations, and because the types of rays are separate from one another, the entropy can be obtained by equation [88]:

$$\delta S = \int_0^\infty V \delta s dv = V \int_0^\infty \frac{\partial s}{\partial u} \delta u dv = \frac{\partial s}{\partial u} V \int_0^\infty \delta u dv = \frac{\partial s}{\partial u} \delta U \quad (3.12)$$

where $\delta s dv$ indicates the infinite change in the entropy of the radiation that confines modes with frequencies between ν and $\nu + d\nu$. Equation above consists of the change in energy. By substituting Eq. (3.11) into Eq. (3.12), it can be given as:

$$\frac{\delta S}{\delta U} = \frac{\partial s}{\partial u} = \frac{1}{T} \quad (3.13)$$

The integration of entropy intensity over all angles can be calculated as [20]:

$$S = \int dS = \int_0^{2\pi} \int_0^{\pi/2} L \cos \theta_z \sin \theta_z d\theta_z d\alpha_s = L \int_0^{2\pi} \int_0^{\pi/2} \cos \theta_z \sin \theta_z d\theta_z d\alpha_s = L\pi \quad (3.14)$$

where L is the entropy intensity.

3.3 Expression of Maximum Efficiency for Solar Radiation

The exergy of a system, which depends on the energy and entropy, can guide us to determine the transformation of available energy into useful work. The maximum efficiency can be achieved based on the definition of efficiency provided by the second law of thermodynamics. In a closed system, the expression for the exergy of blackbody radiation at a constant volume can be determined by the exergy definition of a substance, which is given by the following equation [88]:

$$Ex = (E - E_a) - T_a (S - S_a) \quad (3.15)$$

The reference state of radiation exergy occurs at the environment temperature, which is zero at the dead state. Therefore, E_a , T_a , and S_a are system properties at the reference state. The exergy equation of solar radiation is applied for the source at T and the sink at T_a ; and it can be demonstrated for constant volume, as shown in Figure 3.2.

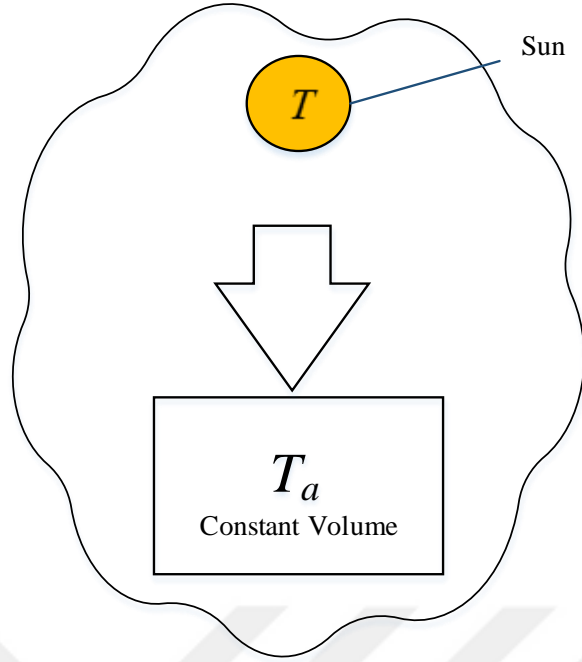


Figure 3.2 Schematic to discuss the exergy content of constant volume.

The spectral radiative energy density is computed by the Planck Law in terms of frequency or wavelength, as shown in Eq. (3.16) below [6]:

$$u_{b,\nu} = \frac{8\pi h\nu^3 / c^3}{e^{(h\nu/kT)} - 1} \quad \text{or} \quad u_{b,\lambda} = \frac{8\pi hc / \lambda^5}{e^{(h\lambda/kT)} - 1} \quad (3.16)$$

where ν is the frequency. The energy density can be computed by integrating Eq. (3.16) in term of frequency as:

$$u = \int_0^\infty u_{b,\nu} d\nu = \int_0^\infty \frac{8\pi h\nu^3 / c^3}{e^{(h\nu/kT)} - 1} d\nu \quad (3.17)$$

$$\text{Let} \quad x = \frac{h\nu}{kT} \quad dx = \frac{h}{kT} d\nu$$

$$u = \frac{8\pi k^4 T^4}{c^3 h^3} \int_0^\infty \frac{x^3 dx}{e^x - 1} \quad \text{by dividing on } e^x \text{ and it can note that } \frac{e^{-x}}{1 - e^{-x}} = \sum_{n=1}^\infty e^{-nx}$$

$$u = \frac{8\pi k^4 T^4}{c^3 h^3} \sum_{n=1}^{\infty} \int_0^{\infty} x^3 e^{-nx} dx \quad (3.18)$$

Integration by parts method $\int fdg = fg - \int gdf$

$$u = \frac{8\pi k^4 T^4}{c^3 h^3} \sum_{n=1}^{\infty} \frac{6}{n^4} = \frac{8\pi k^4 T^4}{c^3 h^3} \frac{\pi^4}{15} = \frac{8\pi^5 k^4}{15c^3 h^3} T^4 \quad (3.19)$$

The universal constant can be computed by Eq. (3.4). Thus, the energy density can be obtained as:

$$u = aT^4 \quad (3.20)$$

The spectral radiative entropy density in terms of spectral radiative energy density and frequency is obtained by [89]:

$$s_{b,v} = \frac{ku_{b,v}}{hv} \left[\left(1 + \frac{8\pi hcv^3}{u_{b,v}} \right) \ln \left(1 + \frac{8\pi hcv^3}{u_{b,v}} \right) - \left(\frac{8\pi hcv^3}{u_{b,v}} \right) \ln \left(\frac{8\pi hcv^3}{u_{b,v}} \right) \right] \quad (3.21)$$

A similar expression can also be written in terms of spectral radiative energy density and wavelength [89]:

$$s_{b,\lambda} = \frac{\lambda ku_{b,\lambda}}{hc} \left[\left(1 + \frac{8\pi hc}{\lambda^5 u_{b,\lambda}} \right) \ln \left(1 + \frac{8\pi hc}{\lambda^5 u_{b,\lambda}} \right) - \left(\frac{8\pi hc}{\lambda^5 u_{b,\lambda}} \right) \ln \left(\frac{8\pi hc}{\lambda^5 u_{b,\lambda}} \right) \right] \quad (3.22)$$

The integration of spectral entropy density gives:

$$s = \int_0^{\infty} s_{b,v} dv = \frac{8\pi k}{c^3} \int_0^{\infty} v^2 \left[\left(\frac{u_{b,v} c^3}{8\pi h v^3} + 1 \right) \ln \left(1 + \frac{8\pi hcv^3}{u_{b,v}} \right) - \ln \left(\frac{8\pi hcv^3}{u_{b,v}} \right) \right] dv \quad (3.23)$$

Substituting Eq. (3.16) in Eq. (3.23), the expression of entropy density can be written as:

$$s = \frac{8\pi k}{c^3} \int_0^\infty v^2 \left[\left(\frac{1}{e^{(hv/kT)} - 1} + 1 \right) \ln(1 + e^{(hv/kT)} - 1) - \ln(1 / (e^{(hv/kT)} - 1))^{-1} \right] dv \quad (3.24)$$

Eq. (3.24) can be simplified, and the following equation can be obtained:

$$s = \frac{8\pi k}{c^3} \left[\int_0^\infty \frac{(hv/kT)v^2}{e^{(hv/kT)} - 1} dv + \int_0^\infty v^2 \ln \left(\frac{1}{1 - e^{-(hv/kT)}} \right) dv \right] \quad (3.25)$$

$$\text{Let } x = \frac{hv}{kT} \quad dx = \frac{h}{kT} dv$$

$$s = \frac{8\pi k^4 T^3}{c^3 h^3} \left[\int_0^\infty \frac{x^3 dx}{e^x - 1} - \int_0^\infty x^2 \ln(1 - e^{-x}) dx \right] \quad (3.26)$$

By dividing the first part of the integral on e^x and noting $\frac{e^{-x}}{1 - e^{-x}} = \sum_{n=1}^{\infty} e^{-nx}$, we obtain:

$$s = \frac{8\pi k^4 T^3}{c^3 h^3} \left[\sum_{n=1}^{\infty} \int_0^\infty x^3 e^{-nx} dx - \int_0^\infty x^2 \ln(1 - e^{-x}) dx \right] \quad (3.27)$$

Then, it can be integrated by parts method as:

$$s = \frac{8\pi k^4 T^3}{c^3 h^3} \left[\left(\sum_{n=1}^{\infty} \frac{6}{n^4} \right) + \left(\frac{1}{3} \sum_{n=1}^{\infty} \frac{6}{n^4} \right) \right] \quad (3.28)$$

Thus,

$$s = \frac{8\pi k^4 T^3}{c^3 h^3} \left[\frac{\pi^4}{15} + \frac{\pi^4}{45} \right] = \frac{8\pi^5 k^4}{15c^3 h^3} \left[T^3 + \frac{1}{3} T^3 \right] = \frac{4}{3} aT^3 \quad (3.29)$$

The spectral energy intensity ($I_{b,v}$) and the spectral entropy intensity ($L_{b,v}$) for black surface are used to determine spectral exergy intensity. Both energy and entropy intensities can propagate in a given direction per unit of area, per unit of solid angle and

per unit of frequency. The corresponding blackbody radiation energy and entropy intensities are obtained by multiplying the spectral energy density ($u_{b,v}$) and the spectral entropy density ($s_{b,v}$) by $(c/4\pi)$ [20]. Spectral energy intensity and spectral entropy intensity, can then be written as:

$$I_{b,v} = \frac{cu_{b,v}}{4\pi} \quad \text{and} \quad L_{b,v} = \frac{cs_{b,v}}{4\pi} \quad (3.30)$$

The spectral energy ($E_{b,v}$) emitted by black surfaces at different temperatures can be determined using:

$$E_{b,v} = \pi(I_{b,v} - I_{b,a,v}) \quad (3.31)$$

The spectral exergy ($Ex_{b,v}$) of the selective coating surface, in terms of frequency, can be determined by the following equation:

$$Ex_{b,v} = \pi[(I_{b,v} - I_{b,a,v}) - T_a(L_{b,v} - L_{b,a,v})] \quad (3.32)$$

The spectral exergy-to-energy ratio is a useful parameter to help understanding the maximum conversion of solar radiation. This ratio is called the maximum spectral efficiency and is defined as:

$$\psi_{b,v} = \frac{Ex_{b,v}}{E_{b,v}} = \frac{(I_{b,v} - I_{b,a,v}) - T_a(L_{b,v} - L_{b,a,v})}{(I_{b,v} - I_{b,a,v})} \quad (3.33)$$

From the definition of exergy to energy ratio, the formula for the maximum efficiency of the black surface can be derived and computed by integrating Eq. (3.33):

$$\psi = \int_0^{\infty} \frac{(I_{b,v} - I_{b,a,v}) - T_o(L_{b,v} - L_{b,a,v})}{(I_{b,v} - I_{b,a,v})} dv = \int_0^{\infty} \frac{(c/4\pi)((u_{b,v} - u_{b,a,v}) - T_o(s_{b,v} - s_{b,a,v}))}{(c/4\pi)(u_{b,v} - u_{b,a,v})} dv \quad (3.34)$$

The integration of Eq. (3.34) is obtained by Substituting Eqs. (3.20) and (3.29) in Eq. (3.34), the maximum efficiency can be obtained as:

$$\psi = \frac{a(T^4 - T_a^4) - \frac{4}{3}aT_a(T^3 - T_a^3)}{a(T^4 - T_a^4)} = 1 - \frac{4T_a(T^3 - T_a^3)}{3(T^4 - T_a^4)} \quad (3.35)$$

This ratio is named “maximum efficiency” as it corresponds to the theoretical maximum, based on the second law of thermodynamics. In addition to the present approach, there are three main expressions for calculating maximum efficiency can be used to estimate maximum work from solar radiation such as Petela, Spanner, and Jeter, are compared in the next section.

3.4 Validations and Comparisons

Several models that comprise a cylinder-piston system have been used to analyze the maximum efficiency of solar radiation. However, concerns regarding the use of these models for validation are raised because of uncertainties in their actual applications. In addition, the change in the internal energy of radiation should be considered. In this Chapter, we give considerable attention to the system that includes a radiation source and an absorbing sink at a constant volume. This system undergoes a reversible process from the initial state to the final state (dead state), including a change in internal energy. The exergy of the system, which can be produced from a change in internal energy and entropy, can be transformed into useful work. Thus, the development of this model is doubtless, and the formula obtained using it can be considered for investigation. The validation of these analyses are utilized to assess the advantages, or obstacles, of the following two concepts: (1) The comparison of four formulations for maximum radiation efficiency, and (2) The effect of operating conditions on maximum efficiency.

3.4.1 The Comparison of Four Formulations for Maximum Radiation Efficiency

The ratio of radiation exergy to radiation energy is determined using the formulas presented in Table 3.1, and are compared in the Figures 3.3 and 3.4.

Table 3.1 The four formulations of maximum radiation efficiency presented by various researchers [11, 12, 18, 22].

Researcher	Input	Output	Maximum Efficiency
Petela	Radiation energy	Radiation exergy	$1 + \frac{1}{3} \left(\frac{T_a}{T} \right)^4 - \frac{4}{3} \frac{T_a}{T}$
Spanner	Radiation energy	Absolute work	$1 - \frac{4}{3} \frac{T_a}{T}$
Jeter	Heat	Network of a heat engine	$1 - \frac{T_a}{T}$
Present Approach	Radiation energy	Radiation exergy	$1 - \frac{4}{3} \frac{(T_a T^3 - T_a^4)}{(T^4 - T_a^4)}$

All the comparisons are focused on the ideal conversion of solar radiation into work. Although the use of several approaches is valid, doing so will prevent comparison with a perfect estimation of thermal radiation exergy. The difference between the formulas of Petela and Spanner emerges because Spanner's formula considers absolute work at maximum availability. The formula of Jeter is derived as the maximum efficiency for the conversion of thermal radiation into work using Carnot efficiency and assuming that the surface of the sun and the surface of an environment are directly in contact.

For maximum efficiency, the values are calculated using the four expressions provided in Table 3.1, and are plotted in Figure 3.3. The variations between Jeter's maximum efficiency formula, which considers heat transfer via conduction and convection, and the other expressions, which consider heat transfer via radiation, are presented. It is clear that, the maximum efficiency associated with radiation heat transfer

is consistently less than the maximum efficiency related to conduction and convection heat transfer. That is, the losses caused by radiation heat transfer are higher than those caused by other modes of heat transfer because energy transfer via radiation is proportional to the fourth power of the temperature. For example, at a radiation temperature of 2000 K, the efficiency with radiation effect is less than 6.3% of the efficiency without radiation effect. As shown in Figure 3.3, the models proposed by Petela, Spanner, and the current work exhibit highly similar behavior because these approaches deal with the effect of radiation heat transfer. By contrast, Jeter’s approach only focuses on conduction and convection heat transfer modes.

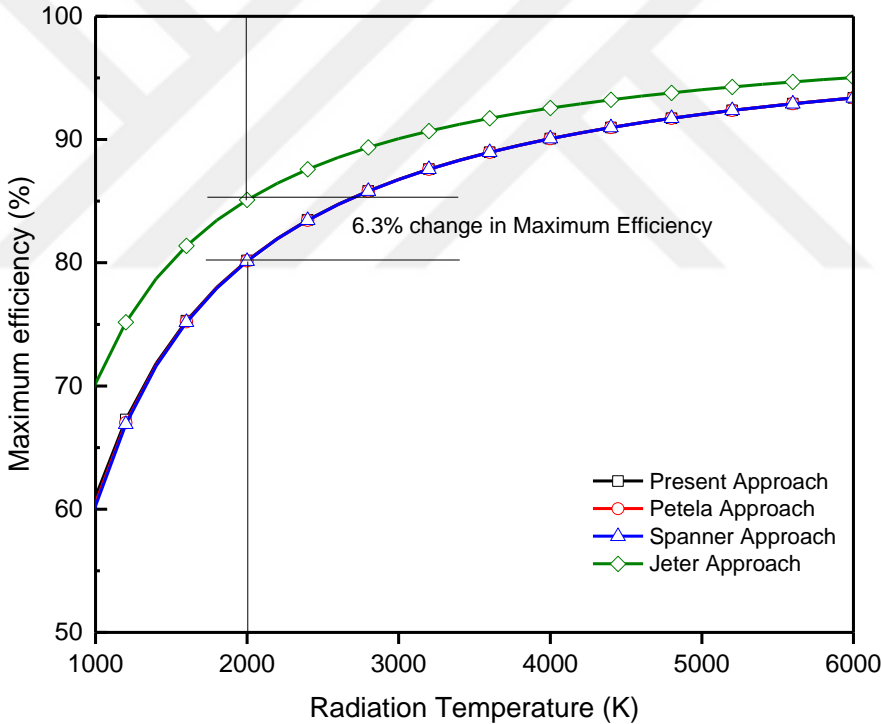


Figure 3.3 Comparison of the maximum efficiency values of radiation exergy.

3.4.2 The Effect of Operating Conditions on Maximum Efficiency

The purpose of various operating conditions was to specify the effect of each parameter on maximum efficiency. Figure 3.4 shows the effect of environmental

temperature on maximum efficiency. It is clear that an increase in ambient temperature reduces maximum efficiency. However, maximum efficiency is fully increased when radiation temperature increases.

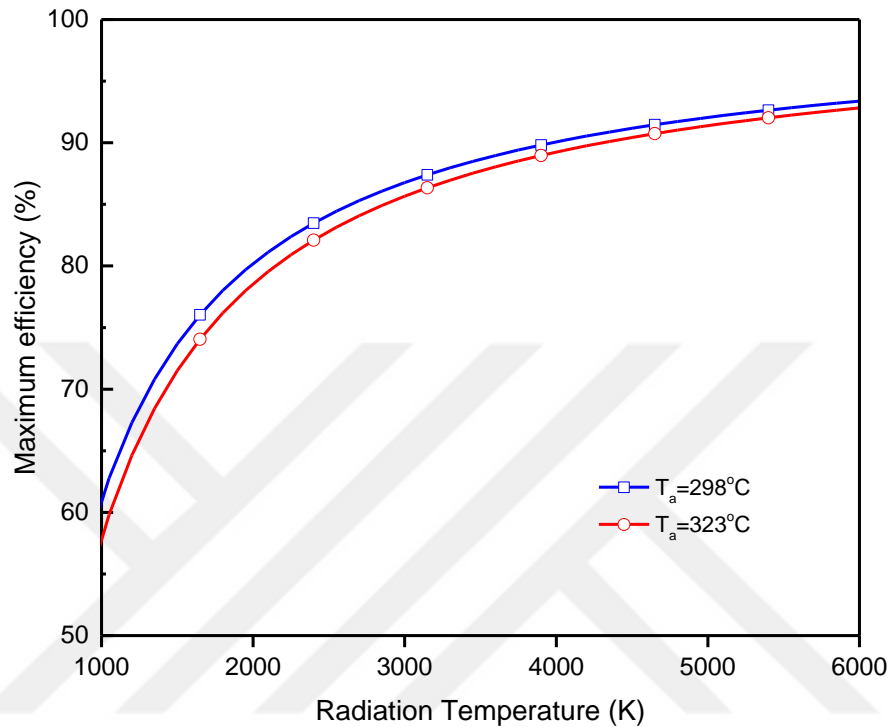


Figure 3.4 Effect of environmental temperature on maximum efficiency.

The theoretical explanation for exergy destruction and maximum efficiency as a function of radiation temperature, is shown in Figure 3.5. Maximum efficiency increases exponentially from 60% at 1000 K to 85% at 2500 K. Then, it increases gradually until it reaches 93% at 6000 K. By contrast, exergy destruction percentage decreases dramatically from 40% at 1000 K to 15% at 2500 K. Thereafter, it declines steadily to 7% at 6000 K. The maximum efficiency and exergy destruction percentage exhibit dissimilar trends because a reduction in exergy destruction is considered as a gain in maximum efficiency.

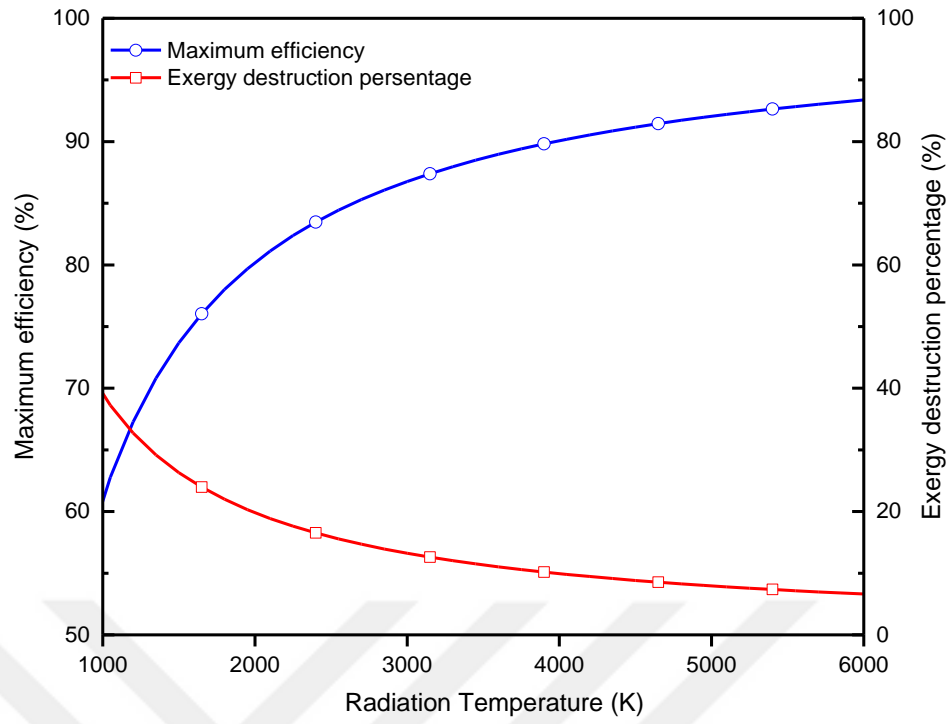


Figure 3.5 Effects of radiation temperature on maximum efficiency and exergy destruction.

CHAPTER IV

RADIATIVE ANALYSES OF SPECTRALLY-SELECTIVE SURFACES FOR CSP SYSTEMS

4.1 Radiative Properties of Spectrally Selective Surfaces

Spectral radiative properties are used to describe the behavior of materials which have been subject to electromagnetic waves at different wavelengths. The suffix -ivity is added for the properties of ideal surfaces, the suffix -ance is used for real properties at a constant temperature, which are defined for an isothermal layer and may depend on layer thickness [6]. These properties are necessary for the analysis of the optical efficiency of CSP systems.

Here, we present a more detailed analysis and includes the effect of environmental temperature, the spectral absorption/emission of the coatings, and operating temperature to determine the radiative energy and exergy efficiencies of a system. An ideal selective absorber must have maximum absorptivity within the wavelength range of solar radiation, i.e., 250 nm to 2500 nm. For an opaque material, the portion of the incident radiation that is not reflected is transmitted through the surface and then absorbed by a layer that extends below the surface.

Spectral directional absorptance can be expressed in terms of spectral directional reflectance ($\rho(\lambda, \theta)$) for opaque materials according to Kirchoff's law [6]:

$$\alpha(\lambda, \theta) = 1 - \rho(\lambda, \theta) \quad (4.1)$$

Coating spectral emittance ($\varepsilon(\lambda, T)$) depends on the wavelength of the radiative energy and the temperature of the outer surface of the absorber.

$$\varepsilon(\lambda, T) = \alpha(\lambda, T) \quad (4.2)$$

Details of energy and exergy analyses for selective coating of CSP systems, are given in the following sections.

4.1.1 Radiative Energy Analysis

In a CSP system, solar radiation is reflected and concentrated on a receiving surface by the reflector. A significant portion of this radiation absorbed by the coating on the receiver, the remaining is reflected. The absorbed portion is considered as useful radiative energy. The thermal system (heat engine) receives energy from the surface of the absorber (thermal receiver), which is partly converted to useful work, and the remainder is transferred to a low-temperature sink (thermal sink). The radiative energy balance of radiation incident on a selective coating surface is presented in Figure 4.1.

The wavelength range of solar radiation is 250 nm to 2500 nm, the thermal radiation emitted from the surface of the absorber above is 3000 nm; which represents the infrared segment of the electromagnetic wave spectrum [6]. Consequently, selective coatings should have high absorptivity within the solar radiation wavelength range, and low emissivity in the infrared electromagnetic spectrum.

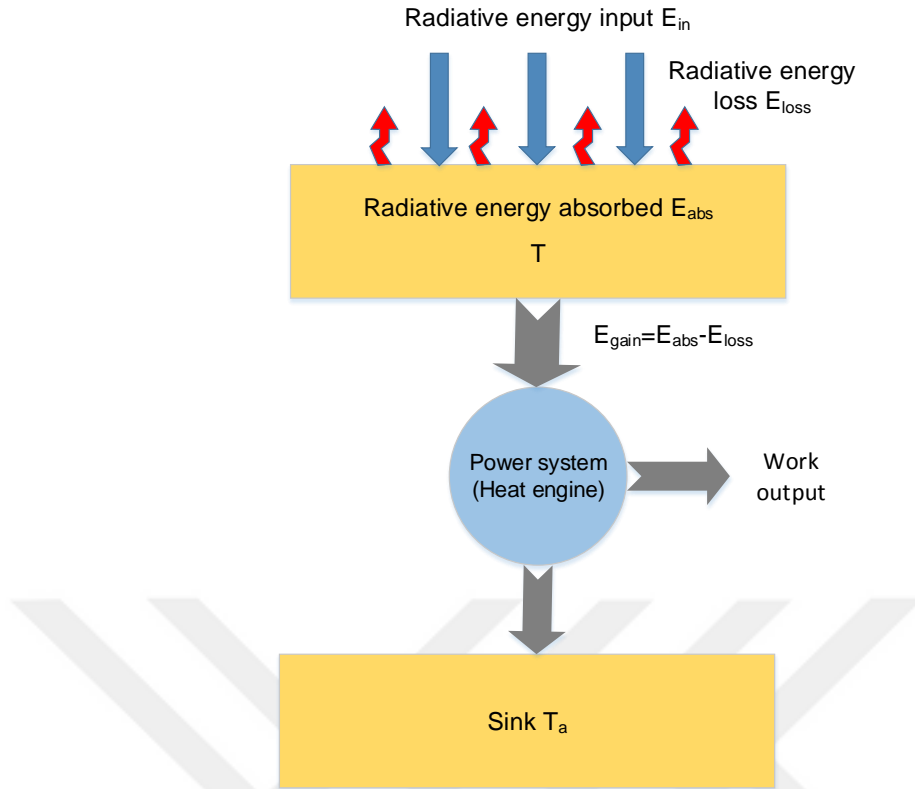


Figure 4.1 Schematic of radiative energy flow for a CSP system.

Spectral radiative energy gain is the energy flux transferred to the power system (heat engine) at a specific wavelength, determined by the following equation:

$$E_{gain,\lambda} = E_{abs,\lambda} - E_{l,\lambda} \quad (4.3)$$

where, $E_{gain,\lambda}$ is the spectral radiative energy gain, $E_{abs,\lambda}$ is the spectral absorbed radiative energy, and $E_{l,\lambda}$ is the spectrally emitted (lost) radiative energy.

Assuming that the source of radiation is a blackbody at $T=5800$ K, the absorbed portion of spectral blackbody radiative energy can be determined as:

$$E_{abs,\lambda} = E_{b,\lambda} \alpha(\lambda) = \frac{2\pi hc^2 \alpha(\lambda)}{\lambda^5 \left[e^{(h\lambda/kT)} - 1 \right]} \quad (4.4)$$

The total absorbed portion of blackbody radiative energy can be expressed after integrating Eq. (4.4) over all wavelength, as:

$$E_{abs} = \int_0^{\infty} E_{b,\lambda} \alpha(\lambda) d\lambda = \alpha \sigma T^4 \quad (4.5)$$

For CSP systems, the solar spectrum ($E_{dir,\lambda}$) with a concentrating ratio (C) can be applied to determine the amount of spectral radiative energy input to the system ($E_{in,\lambda}$). Then, the equation that describes the spectral absorbed radiative energy becomes:

$$E_{abs,\lambda} = CE_{dir,\lambda} \alpha(\lambda) = E_{in,\lambda} \alpha(\lambda) \quad (4.6)$$

After integration, the total absorbed portion is determined as:

$$E_{abs} = CE_{dir} \int_0^{\infty} \alpha(\lambda) d\lambda = \alpha CE_{dir} = \alpha E_{in} \quad (4.7)$$

where E_{dir} is direct solar radiation on earth, which is assumed to be 900 W/m² [90].

Spectral radiative energy loss emitted by a selective coating surface can be defined at a specific wavelength as:

$$E_{l,\lambda} = E_{b,\lambda} \varepsilon(\lambda) = \frac{2\pi hc^2 \varepsilon(\lambda)}{\lambda^5 \left[e^{(h\lambda/kT)} - 1 \right]} \quad (4.8)$$

The total emitted radiative energy loss is computed by integrating Eq. (4.8) over the entire wavelength range:

$$E_l = \int_0^{\infty} E_{b,\lambda} \varepsilon(\lambda) d\lambda = \varepsilon \sigma T^4 \quad (4.9)$$

Spectral radiative energy efficiency is the ratio of spectral radiative energy gain to the spectral radiative energy input at a specific wavelength. It can be defined as:

$$\eta_{en,\lambda} = \frac{E_{gain,\lambda}}{E_{in,\lambda}} \quad (4.10)$$

Radiative energy efficiency, over the entire wavelength spectrum becomes:

$$\eta_{en} = \frac{E_{gain}}{E_{in}} \quad (4.11)$$

where E_{gain} and E_{in} are total radiative energy gain and radiative energy input, respectively.

4.1.2 Radiative Exergy Analysis

Exergy analysis is based on the conditions of the environment and the state of the system. To analyze the spectral radiative exergy of a surface, we assume that the surface is coated with a thin layer of selective coating. Spectral radiative exergy can be expressed as:

$$Ex_{gain,\lambda} = Ex_{abs,\lambda} - Ex_{d,\lambda} \quad (4.12)$$

where, $Ex_{gain,\lambda}$ is the spectral radiative exergy gain, $Ex_{abs,\lambda}$ the spectral absorbed radiative exergy and $Ex_{d,\lambda}$ the spectral emitted radiative exergy destruction.

The spectral radiative exergy of the absorbed portion can then be determined by multiplying the spectral radiative exergy of a blackbody by the absorptivity at a specific wavelength:

$$Ex_{abs,\lambda} = Ex_{b,\lambda} \alpha(\lambda) \quad (4.13)$$

The total radiative exergy of an absorbed portion is calculated by the integration of Eq. (4.13), over the wavelength spectrum becomes:

$$Ex_{abs} = \int_0^{\infty} Ex_{b,\lambda} \alpha(\lambda) d\lambda = \int_0^{\infty} \psi_{\lambda} E_{b,\lambda} \alpha(\lambda) d\lambda = \psi \alpha \sigma T^4 \quad (4.14)$$

On the other hand, for a typical CSP system in a real situation, the radiative energy input (E_{in}) and maximum radiative efficiency (ψ), can be used to determine the radiative exergy input to the system as:

$$Ex_{in} = CEx_{dir} = C\psi E_{dir} = \psi E_{in} \quad (4.15)$$

The spectral radiative exergy of the absorbed portion of can be determined as:

$$Ex_{abs,\lambda} = CEx_{dir,\lambda}\alpha(\lambda) = C\psi_{\lambda}E_{dir,\lambda}\alpha(\lambda) \quad (4.16)$$

The total absorbed radiative exergy can be computed by integration of Eq. (4.16) over the entire spectrum:

$$Ex_{abs} = \int_0^{\infty} C\psi_{\lambda}E_{dir,\lambda}\alpha(\lambda)d\lambda = CE_{dir} \int_0^{\infty} \psi_{\lambda}\alpha(\lambda)d\lambda = \psi\alpha E_{in} \quad (4.17)$$

Part of the absorbed radiative exergy is destroyed because of emissions from the absorber surface, which is expressed as:

$$Ex_{d,\lambda} = \varepsilon(\lambda)Ex_{b,\lambda} \quad (4.18)$$

To obtain the total radiative exergy destruction (Ex_d), Eq. (4.18) should be integrated over the entire spectrum:

$$Ex_d = \int_0^{\infty} Ex_{b,\lambda}\varepsilon(\lambda)d\lambda = \int_0^{\infty} \psi_{\lambda}E_{b,\lambda}\varepsilon(\lambda)d\lambda = \psi\varepsilon\sigma T^4 \quad (4.19)$$

Spectral radiative exergy efficiency is the ratio of the radiative exergy gained by the absorber surface to the radiative exergy of the captured solar radiation, at a specific wavelength:

$$\eta_{ex,\lambda} = \frac{Ex_{gain,\lambda}}{Ex_{in,\lambda}} \quad (4.20)$$

The integration of spectral radiative exergy efficiency over the entire spectrum yields:

$$\eta_{ex} = \frac{Ex_{gain}}{Ex_{in}} \quad (4.21)$$

These fundamental concepts are applied to practical systems in the next section by studying the radiative properties of five different coatings extensively used for CSP systems.

4.2 Properties of Different Coatings Used for CSP Systems

In this Section, five different spectrally selective surfaces and coatings using the fundamental radiative exergy analysis presented above. We determine their spectral radiative energy and radiative exergy efficiencies and compare their performance for CSP systems.

One of the most commonly used commercial coatings for CSP systems is named Black Chrome (Cr–Cr₂O₃), fabricated by the electrodeposition method. Its substrates are Ni, Fe, Cu and stainless steel [64, 91, 92]. Another commercial product is Luz Cermet (Mo–Al₂O₃ Cermet on Ni and Al substrates) which has limited durability when exposed to air at operating conditions [64, 92]. The third coating, manufactured by Solel, is an attempt to produce an improved absorber, the Universal Vacuum Collector (UVAC) [93]. The UVAC has two samples, A and B, and is composed of a multilayer Al₂O₃-based Cermet but with no Mo [36]. The last selective coating material considered is manufactured by the National Renewable Energy Laboratory (NREL). It is a complex material with the code name NREL-6A [37, 38]. The spectral reflectance values of the

five selective coatings are shown in Figure 4.2. Note that the profile for an ideal selective coating is also shown here. The temperature-dependent, radiative properties of these coatings are listed in Table 4.1.

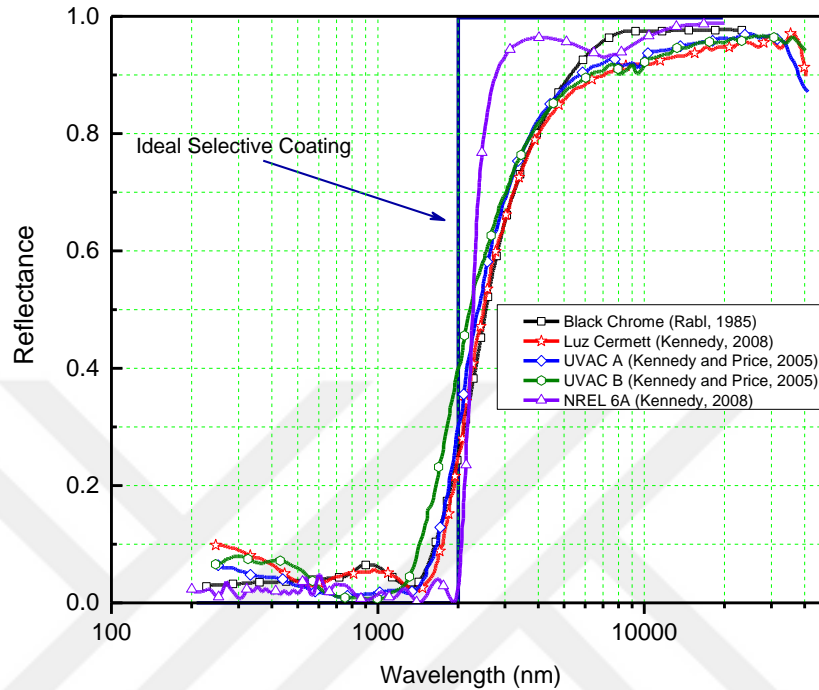


Figure 4.2 Spectral reflectance of the various selective coatings [37, 38, 94].

Table 4.1 The optical properties of several selective coatings at different temperatures [35, 37, 38, 64].

	Commercially Available Coatings				New Prototype by NREL
	Black Chrome	Luz Cermet	UVAC (Al ₂ O ₃ Cermet)		NREL
Function	Cr-Cr ₂ O ₃	Mo-Al ₂ O ₃ Cermet	Test-A	Test-B	6A
Absorptance α					
	0.916	0.938	0.954	0.935	0.959
Emittance ϵ					
25°C	0.081	0.061	0.052	0.069	0.018
100°C	0.109	0.077	0.067	0.084	0.022
200°C	0.146	0.095	0.085	0.103	0.031
300°C	0.183	0.118	0.107	0.125	0.047
400°C	0.220	0.146	0.134	0.150	0.071
450°C	0.239	0.162	0.149	0.164	0.087
500°C	0.257	0.179	0.165	0.178	0.104

Previous analyses have focused on radiative properties at a relatively constant temperature [64, 95, 96]. In this Chapter, emittance as a function of the receiver surface temperature was given, in the form of a second-order polynomial fit; as shown in Table 4.2. This functional form allows more flexibility when studying the performances of CSP systems.

Table 4.2 Emittance expressions of selective coatings.

Selective Coatings	Equations of Emittance as a function of temperature in °C
Cr-Cr ₂ O ₃	$0.0718 + 0.0004t - (1E - 9)t^2$
Mo-Al ₂ O ₃ Cermet	$0.0587 + 0.0001t + (2E - 7)t^2$
UVAC (Al ₂ O ₃ Cermet) Test-A	$0.0495 + 0.0001t + (2E - 7)t^2$
UVAC (Al ₂ O ₃ Cermet) Test-B	$0.0655 + 0.0002t + (1E - 7)t^2$
NREL-6A	$0.0189 - (2E - 5)t + (4E - 7)t^2$

4.3 Results and Discussion

To assess the performance of specific selective coatings of surface absorbers in a CSP system, spectral and thermal analyses, for both radiative energy and radiative exergy, were carried out using the expressions given in the preceding sections. The results of these analyses are used to evaluate the merits, or demerits, of the following three concepts: (1) The spectral analysis based on the theory of blackbody and direct normal solar radiation data, (2) The spectral analysis of the selective coatings of surface absorbers, and (3) The thermal analysis of the selective coatings of surface absorbers.

4.3.1 Spectral radiative analysis of blackbodies and solar radiation

Spectral radiative analysis can be implemented by using two blackbodies, one at the temperature of the sun ($T=5800$ K), the other at the operating temperature of an

absorber in CSP systems ($T=700$ K). The results of this spectral analysis are presented in Figure 4.3. Spectral radiative energy, spectral radiative exergy and the maximum spectral radiative efficiency can be computed by application of the equations presented above in the radiative energy and radiative exergy analyses of spectrally selective surfaces.

Results are shown in Figure 4.3 reveals that the radiative exergy is always lower than radiative energy, which implies that converting all radiative energy to useful work is not possible, as expected. The maximum radiative energy and radiative exergy for the first blackbody at temperature of $T=5800$ K were achieved in the visible wavelength region, while for the second blackbody ($T=700$ K), they are in the infrared region. Exact values of the corresponding peak points are determined from the Wien Law, $\lambda_{peak}=2874.6/T$ where T is the absolute temperature of the blackbody. Losses caused by emitted radiative energy and radiative exergy are, therefore, predominantly in the infrared region. For this reason, the maximum spectral radiative efficiency decreases from 94% in the visible region to 85% in the infrared wavelength region.

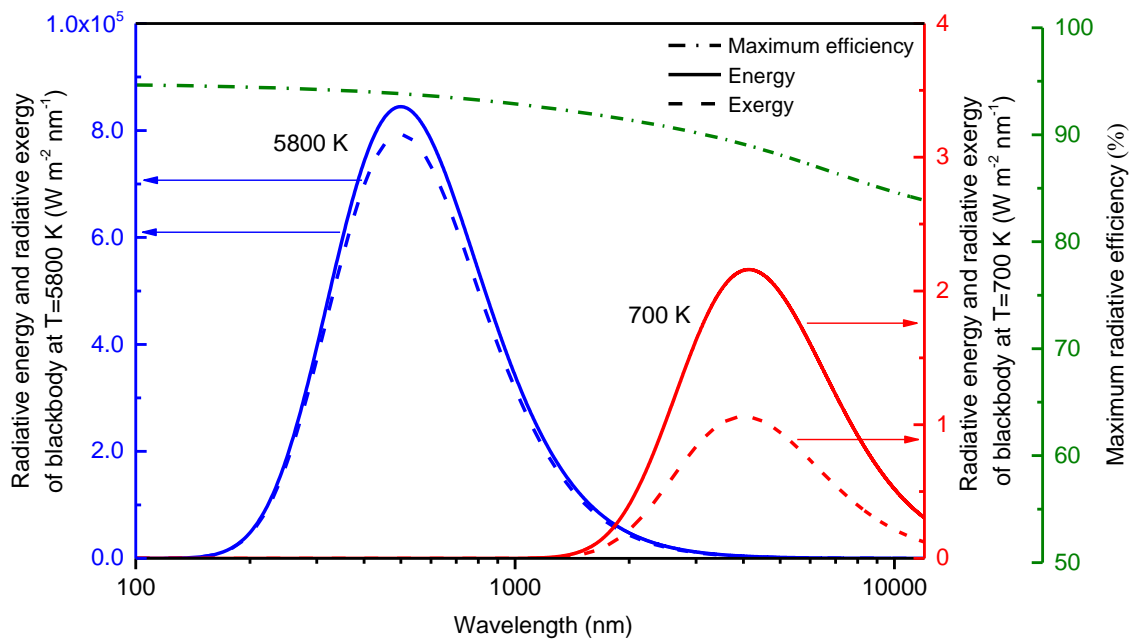


Figure 4.3 Spectral radiative energy, spectral radiative exergy and maximum spectral radiative efficiency corresponding to two blackbodies at $T=5800$ K and $T=700$ K.

Direct normal solar spectral radiation data were used to calculate radiative energy and radiative exergy. The radiative exergy of the spectrum is obtained via maximum radiative efficiency at a specific wavelength; again, as expected, radiative exergy is always lower than radiative energy at a given wavelength. Figure 4.4 shows the results obtained from the spectral radiative energy analysis and the radiative exergy analysis of the direct normal solar spectral radiation.

The radiative exergy profiles can be used to assess how much of incident radiative energy can be converted to useful work. Radiative properties of selective coatings change according to wavelength. An optimum profile of these coatings is needed to decrease radiative exergy destruction and to maximize the spectral radiative efficiency.

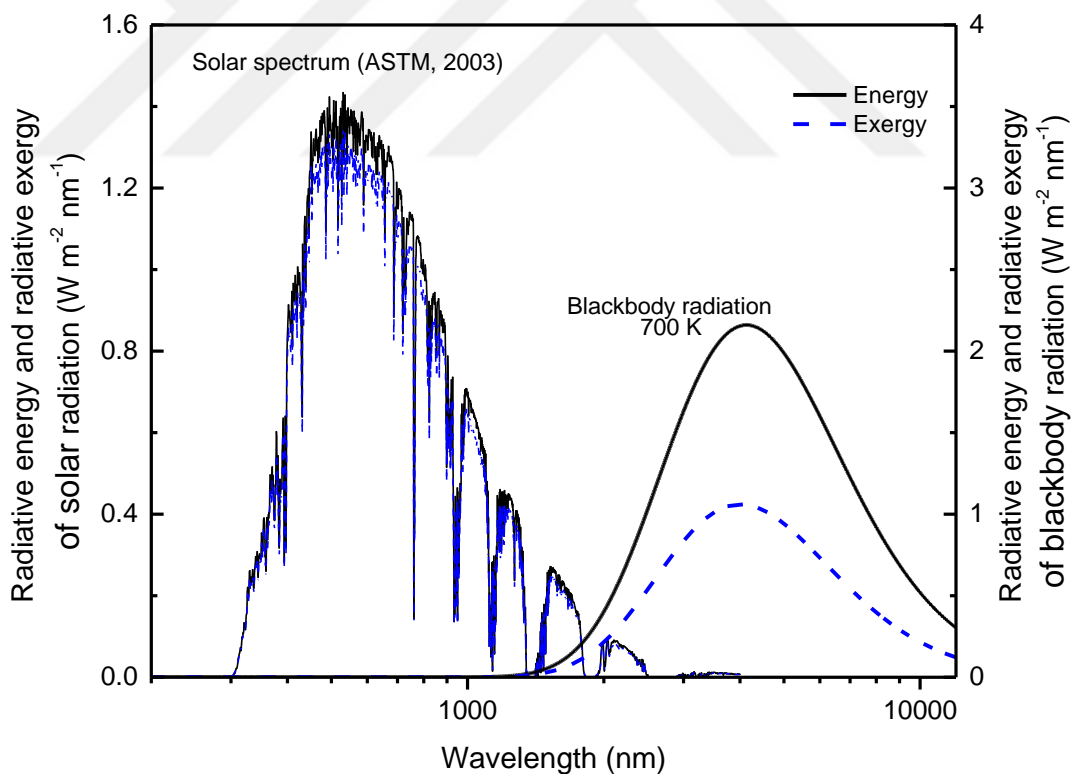


Figure 4.4 Spectral radiative energy and spectral radiative exergy of the direct normal solar spectrum and blackbody radiation at $T=700$ K.

4.3.2 Spectral Analysis of the Selective Coatings for the Surface Absorber

The two approaches were used to assess the spectral performance of five selective coatings. One approach considered two blackbodies for the temperatures of the sun and surface absorber. The second approach was based on the data obtained from direct solar spectral radiation.

The first approach based on blackbody radiation at the temperature of the Sun ($T=5800$ K) and operating temperature ($T_a=700$ K), are shown in Figures 4.5 to 4.8. In Figure 4.5 the spectral radiative energy efficiencies of selective coatings as functions of wavelength, are shown, which are calculated from Eq. (4.10). The radiative energy efficiency profiles of all coatings are similar, with the exception of NREL-6A, which behaves quite differently. The reflectance of NREL-6A is closer to an ideal selective coating. Its spectral radiative energy efficiency is high (close to 95%), due to the high spectral absorptance in the spectrum of solar radiation. On the other hand, the gross loss of spectral radiative energy efficiency in the infrared spectrum is due to the high reflectance of the coatings in this range. The sharp decrease in the value of radiative energy efficiency results from the rapid rise in reflectance. In addition, the spectral value of blackbody radiation above the wavelength 2000 nm, is low.

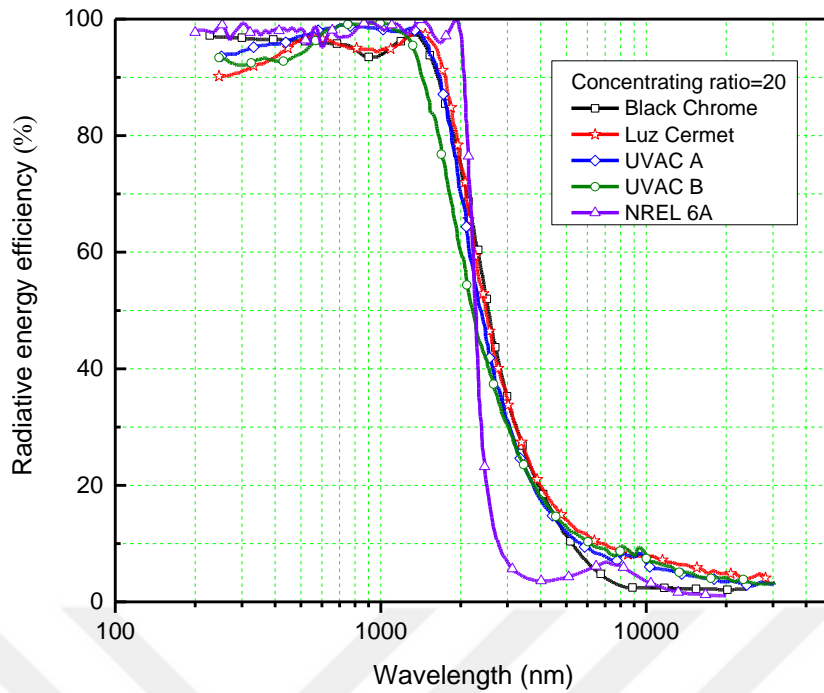


Figure 4.5 Spectral radiative energy efficiencies of selective coatings based on blackbody radiation at temperature of the Sun ($T=5800$ K) and operating temperature ($T=700$ K).

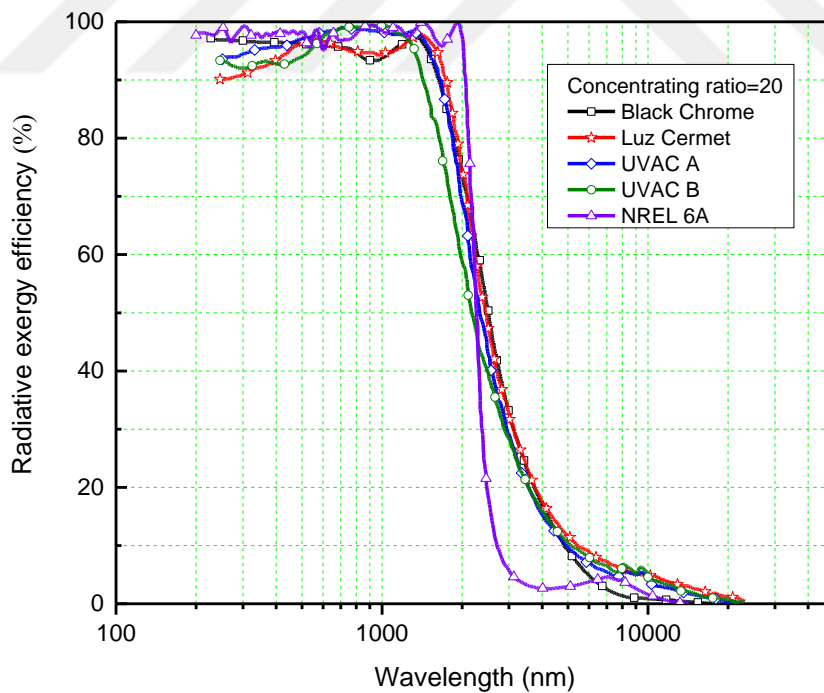


Figure 4.6 Spectral radiative exergy efficiencies of selective coatings based on blackbody radiation at temperature of the Sun ($T=5800$ K) and operating temperature ($T=700$ K).

As stated before, the spectral radiative exergy efficiency is an essential parameter used to determine the quality of selective coatings for converting radiative energy to useful work. Figure 4.6 presents the spectral radiative exergy efficiencies of the coatings as functions of wavelength based on Eq. (4.20). The trends shown indicate that spectral radiative exergy efficiencies have slight fluctuations above 90% until a wavelength of 1400 nm is reached for all selective coatings. Beyond this wavelength, a steep drop is observed in the radiative exergy efficiencies for all selective coatings except the new coating, which continues fluctuating until the wavelength of 2000 nm is reached. Then, there is a sharp drop in radiative exergy efficiency of NREL-6A coating from 99% at 2000 nm to 5% at 3000nm. There are two reasons for this decline: an increase in radiative exergy destruction and a decrease in radiative exergy absorption. The increase in radiative exergy destruction stems from emissions in the infrared region; the decrease in radiative exergy absorption is caused by low spectral blackbody radiation in this region.

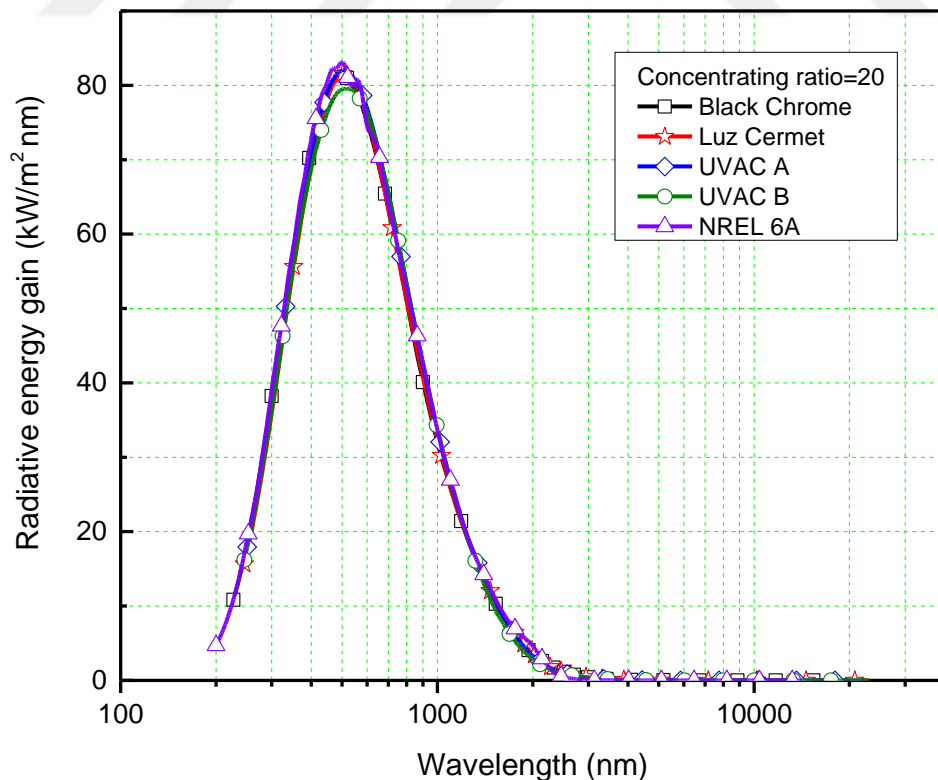


Figure 4.7 Radiative energy gains of selective coatings based on blackbody radiation at temperature of the Sun ($T=5800$ K) and operating temperature ($T=700$ K).

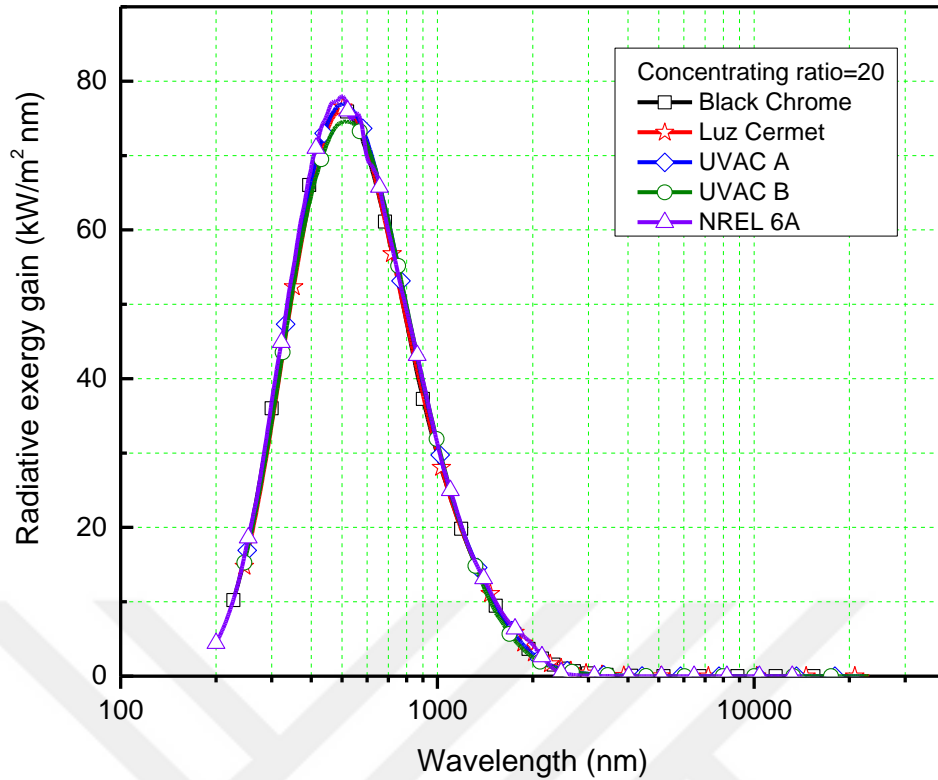


Figure 4.8 Radiative exergy gains of selective coatings based on blackbody radiation at temperature of the Sun ($T=5800$ K) and operating temperature ($T=700$ K).

The spectral radiative energy and radiative exergy gains for the five commercial and experimental selective coatings are shown in Figures 4.7 and 4.8, respectively. Spectral radiative energy and radiative exergy gains are calculated from Eq. (4.3) and Eq. (4.12), respectively. Note that almost all the radiative energy within the solar radiation spectrum is absorbed. By contrast, there is radiative energy loss and radiative exergy destruction caused by the emission from the surface. These losses occur in the infrared region of the electromagnetic spectrum. Figures 4.7 and 4.8 show a clear increasing trend of radiative energy and radiative exergy gains until a peak value is achieved at the wavelength of 500 nm for all selective coatings. NREL-6A coating achieved the highest radiative energy and radiative exergy gains of $83.1 \text{ kW/m}^2\text{nm}$ and $77.9 \text{ kW/m}^2\text{nm}$, respectively. By contrast, UVAC-B coating has the lowest radiative efficiency, and has peak values for radiative energy and radiative exergy gains of $79.5 \text{ kW/m}^2\text{nm}$ and $74.6 \text{ kW/m}^2\text{nm}$, respectively.

The present spectral analysis does not only attempt to determine which selective coating has the maximum radiative energy and radiative exergy efficiencies, but it is also useful for selecting the appropriate coatings by understanding the thermal behavior of a specific coating over the entire spectrum. Based on the analyses, we determined that NREL-6A coating has the best values for the spectral radiative energy efficiency, the spectral radiative exergy efficiency, the spectral radiative energy gain and the spectral radiative exergy gain in the solar radiation range.

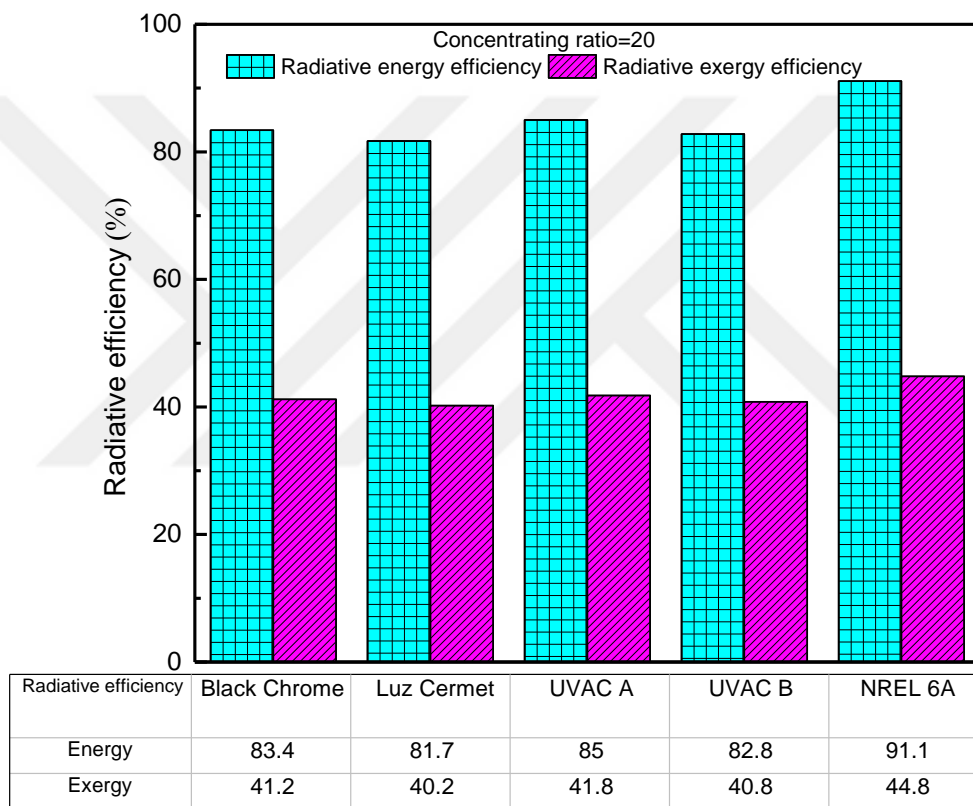


Figure 4.9 Radiative energy and radiative exergy efficiencies of selective coatings based on the data from direct normal solar spectral radiation and operating temperature ($T=700$ K).

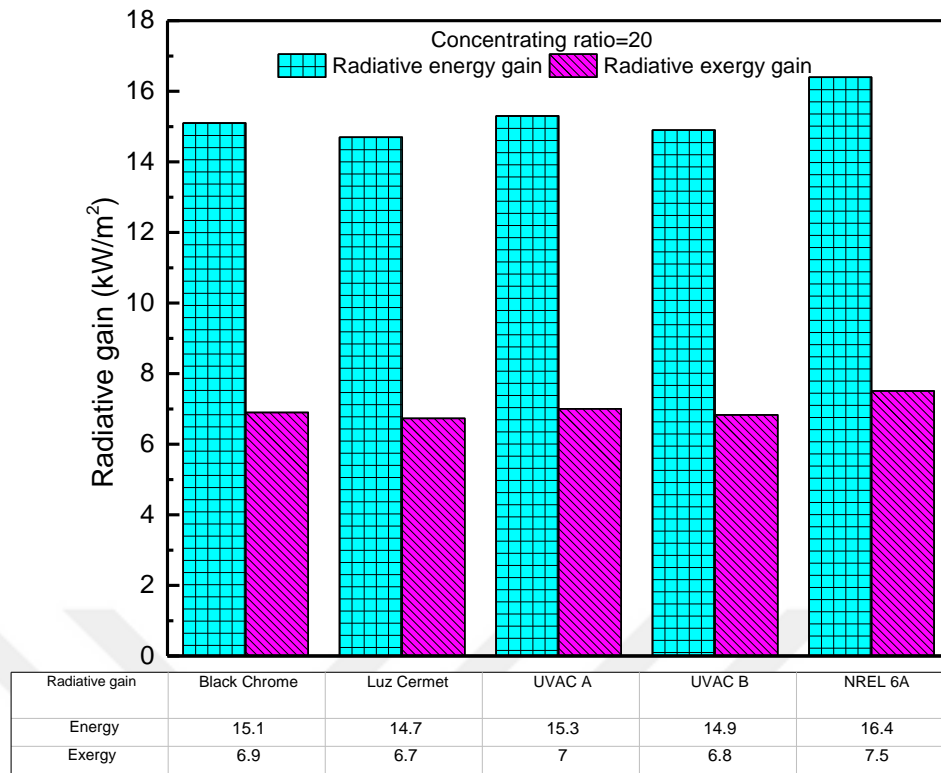


Figure 4.10 Radiative energy and radiative exergy gains of selective coatings based on the data from direct normal solar spectral radiation and operating temperature ($T=700$ K).

Direct normal solar spectral radiation data was used to evaluate the radiative efficiencies of the selective coatings by spectral analysis. This approach has a number of serious drawbacks: particularly, the spectral solar radiation profiles show sharp oscillations which increase computing time. To alleviate this problem, we followed a relatively simple numerical approach. The total solar energy contained in the wavelength range of 250 nm to 20,000 nm is determined by computing the area under the curve for each parameter in analysis. The area under the curve is divided into rectangle segments and estimated the area of each rectangle. The total area under the curve equal to the summation of all rectangles. This approach is used in calculating the efficiencies and gains in radiative energy and radiative exergy analyses to determine the performance of a given selective coating. As seen in Figure 4.9, the radiative energy and radiative exergy efficiencies of these coatings significantly change the performance of CSP system. The

highest energy and exergy radiative efficiencies, computed for NREL-6A coating, were 91.1% and 44.8%, respectively, while the lowest values of radiative energy efficiency (81.7%) and radiative exergy efficiency (40.2%) were obtained for Luz Cermet coating.

The radiative energy gain is the difference between the radiative energy absorbed and lost. Similarly, the radiative exergy gain can be computed as the difference between the radiative exergy absorbed and destroyed. The radiative energy and radiative exergy gains of the selective coatings are shown in Figure 4.10. The highest radiative energy gain (16 kW/m^2) and radiative exergy gain (7.5 kW/m^2) are obtained for the experimental coating while the lowest radiative energy and radiative exergy gains are for Luz Cermet coating which are 14.7 kW/m^2 and 6.7 kW/m^2 , respectively. The differences in the performances of selective coatings can be attributed to the variations in the spectral reflectance values.

No significant difference was observed neither between spectral radiative energy and radiative exergy efficiencies, nor between spectral radiative energy and radiative exergy gains using the first approach, which is based on radiation from the blackbodies at 5800 K (the temperature of the Sun) and 700 K (assumed operating temperature). This was because of the extreme differences between the values of the absorbed and emitted radiative energies. With the second approach, which depended on direct normal solar spectral radiation and operating temperature (700 K) data, a considerable difference between radiative energy and radiative exergy is observed. Although in the calculations there were unexpected obstacles caused by sharp oscillations in the solar radiation spectrum, the results are significant as they show how much radiative exergy is gained from total radiative exergy and thus provide more understanding about the responses of selective coatings.

4.3.3 Thermal Analysis for the Selective Coatings

Thermal analysis is important when investigating the performance of selective coatings. In Table 4.1, test results showing the effect of operating temperature on absorptance and emittance of the five selective coatings are given. Thermal stability should be considered when choosing a coating.

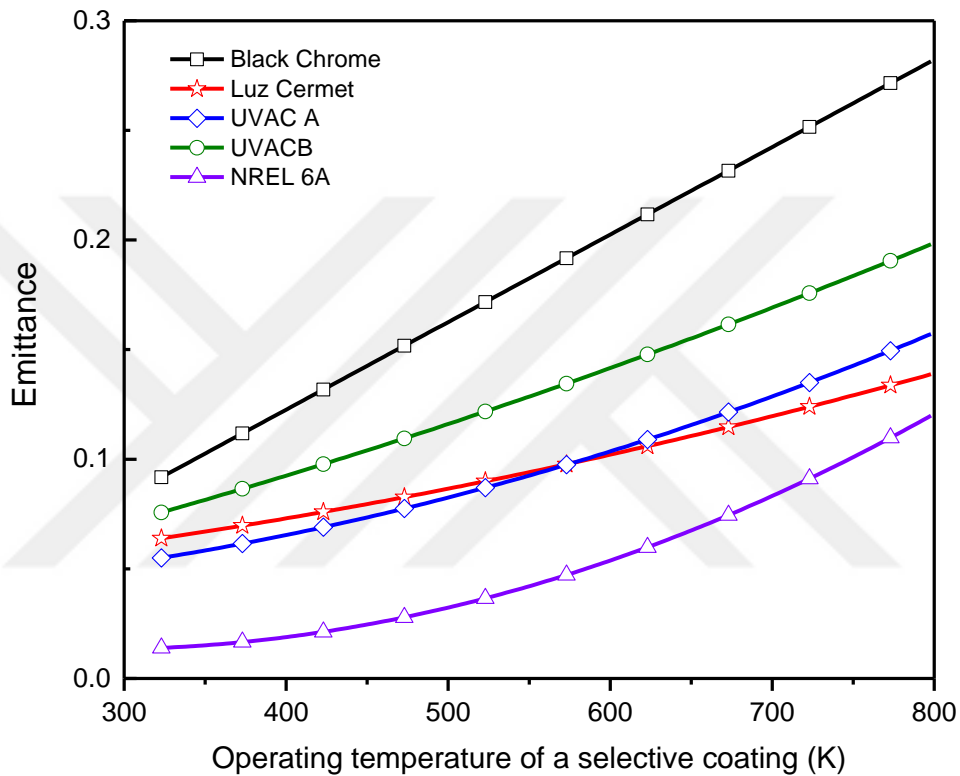


Figure 4.11 Emittance curves of the commercial and experimental selective coatings versus operating temperature.

Emittance is obtained as a function of operating temperature. The results in Figure 4.11 show that the new coating has the lowest emittance, although a slight increase in emittance is observed from 0.02 to 0.12 at 800 K. For Black Chrome coating, there is a marked increase in emittance from 0.09 to 0.285 at 800 K.

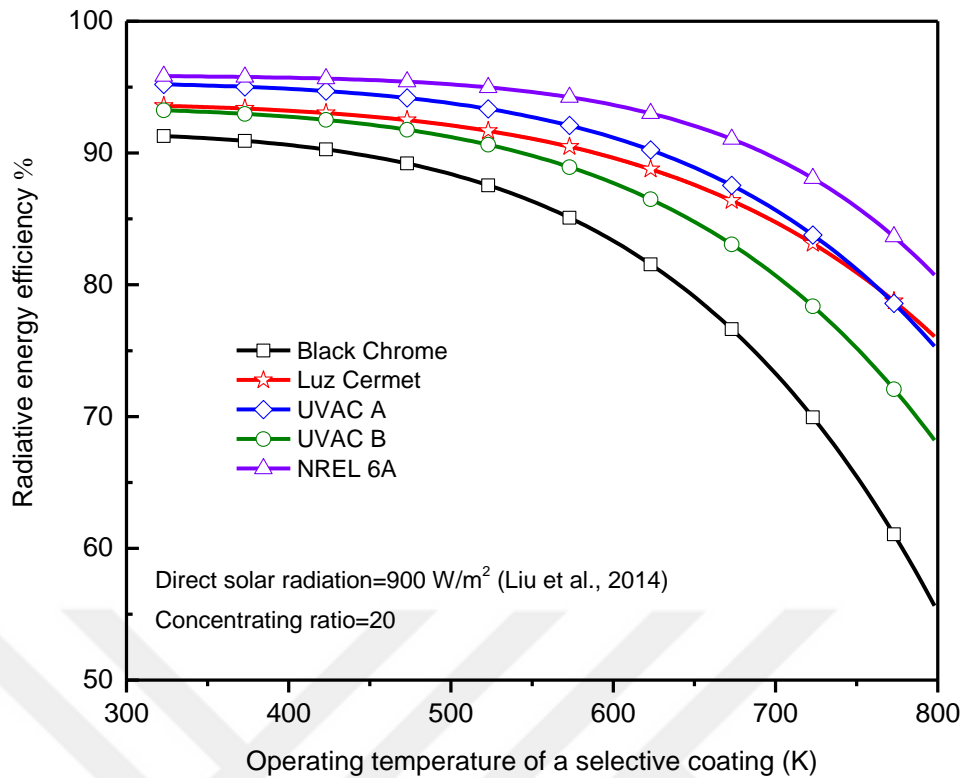


Figure 4.12 Radiative energy efficiencies of the commercial and experimental selective coatings versus operating temperature.

Thermal analysis investigates the effect of operating temperature on radiative energy efficiency. Direct solar radiation and concentrating ratio are assumed to be 900 W/m² [90] and 20, respectively. Figure 4.12 illustrates the radiative energy efficiencies as functions of the operating temperature of the surface absorber. With increasing operating temperature, radiative energy efficiency decreases for all selective coatings because of increasing emittance. Radiative energy loss is related to the emittance of the surface absorber. For this reason, the highest radiative efficiency is achieved by the experimental coating, while Black Chrome coating has the lowest radiative efficiency. For NREL-6A coating, the radiative energy efficiency is 96% at temperature of 325 K, which decreases to 80% at temperature of 800 K. For Black Chrome coating, the highest value of radiative energy efficiency is 91% at temperature of 325 K, while the lowest value is 55% at 800 K.

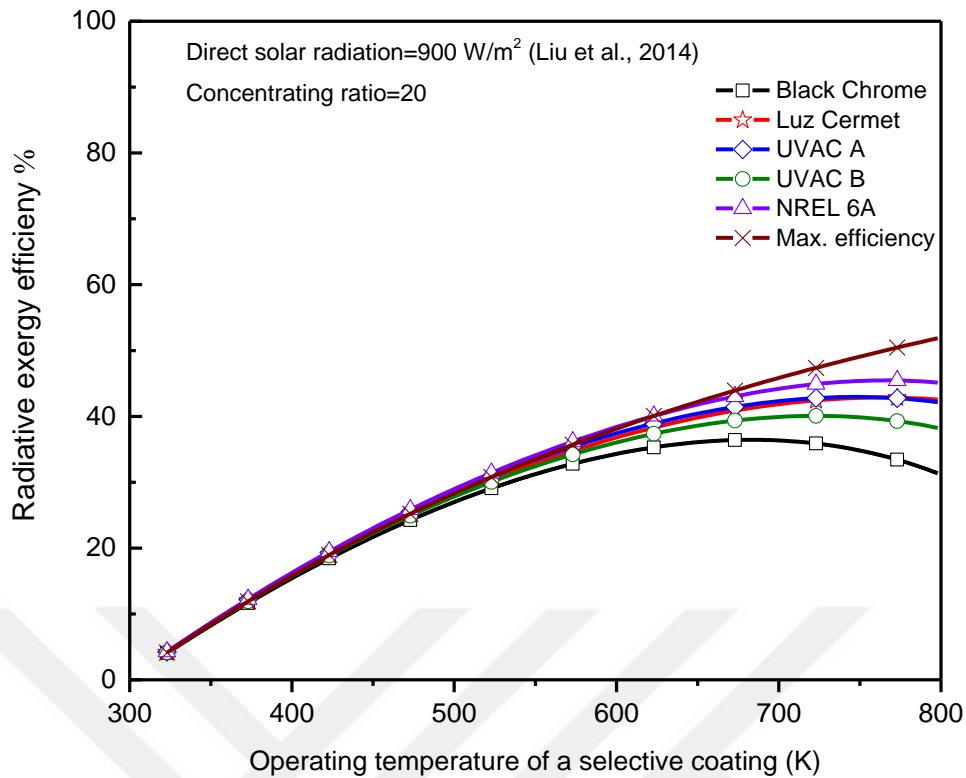


Figure 4.13 Radiative exergy efficiencies of the commercial and experimental selective coatings versus operating temperature.

It is also possible to calculate the radiative exergy efficiencies as functions of operating temperature of selective coatings by thermal analyses which are plotted in Figure 4.13. When the operating temperature increases, radiative exergy efficiency is enhanced. However, as the operating temperature is further increased radiative exergy destruction rises as a result of higher emitted radiation loss, leading to a decrease in radiative exergy efficiency. Maximum radiative exergy efficiency is lower than the maximum radiative energy efficiency for all selective coatings because it is not possible to convert all the available radiative energy into useful work. Best radiative exergy efficiency is achieved for NREL-6A coating, while the poorest efficiency is for Black Chrome coating. The NREL-6A coating has the highest radiative exergy efficiency of 45.5% at temperature of 768 K, Black Chrome coating reaching its highest radiative exergy efficiency value of 36.5% at 683 K. It is clear that the thermal analysis is capable

of providing the most suitable operating temperature to achieve the highest radiative exergy efficiency for a given coating.

4.4 Summary

The performances of five selective coatings are investigated for a CSP system using radiative energy and radiative exergy analyses. These analyses are carried out in a spectral sense, which was the very first time, to our knowledge. The results indicate that radiative exergy losses mostly occur in the infrared region for specific coatings used. This can be altered by changing the spectral absorption of coating. In addition, the quantity of radiative energy profit at a specific wavelength can be obtained by measuring spectral radiative energy efficiency; while the quality of this radiative energy is determined by spectral radiative exergy efficiency calculations. Also, it is noted that the results obtained under direct normal solar spectral radiation are more reliable and can be used for practical applications. The comparisons between the coatings highlighted an unexpected difference between radiative energy and radiative exergy results. The radiative exergy was less than half of the radiative energy regarding efficiency and gain values, showing the significance of how much availability of solar energy can be converted to useful work. Furthermore, we note that the irreversibility of coating surfaces can play an important role in the destruction of exergy. We note that for reliable results, the operating temperature should be used carefully, as it contributes significantly to achieve the thermal stability.

CHAPTER V

SOLAR RADIATION EXERGY AND QUALITY PERFORMANCE FOR IRAQ AND TURKEY

5.1 Solar Radiation Exergy Calculations

To date, several previous studies have proposed to set out models for estimating solar radiation in term of polynomials. Model 1 used is a linear equation approach [48]. A quadratic polynomial equation was put forward as Model 2 [51]. Model 3 was presented by a cubic polynomial equation [53].

All these models are based on the extraterrestrial horizontal radiation, the number of sunny hours, and the day length. However, certain drawbacks of the preceding models are noted because they do not consider the mean temperature, and the mean wind velocity. In this Chapter, an alternative hybrid methodology is derived to determine maximum efficiency, and new models that take into account the effect of changing climate is implemented.

The monthly average daily horizontal extraterrestrial radiation can be calculated as follows [46]:

$$H_o = \frac{24 \times 3600 H_{sc}}{\pi} \left[1 + 0.033 \cos \left(\frac{360n}{365} \right) \right] \left[\cos \phi \cos \delta \sin w + \frac{2\pi w}{360} \sin \phi \sin \delta \right] \quad (5.1)$$

where H_{sc} is the solar constant (1367 W/m^2), i.e., the solar radiation per unit area that is incident on a plane normal to the line connecting the Sun to the Earth [97]. n is the number of the day as counted starting from January 1st. ϕ is the latitude of the site, w is the mean sunrise hour angle, and δ is the declination angle which is the angle between the line connecting the Sun and the Earth, determined by [98]:

$$\delta = 23.45 \sin \left[\frac{360}{365} (n + 284) \right] \quad (5.2)$$

The mean sunrise hour angle w is calculated as [99]:

$$w = \cos^{-1} (-\tan \delta \tan \alpha_s) \quad (5.3)$$

The day length N_o can be obtained from the following equation [100]:

$$N_o = \frac{2w}{15} \quad (5.4)$$

As was mentioned in Chapter two, the maximum conversion efficiency for the solar radiation ψ is defined as the ratio of the maximum work obtained from solar energy to solar radiation energy. It is expressed as:

$$\psi = \frac{Ex_{rad}}{E_{rad}} \quad (5.5)$$

where Ex_{rad} is the exergy flux of solar radiation. It is assumed to be the exergy value of the monthly average daily global radiation on horizontal plane H_{ex} . E_{rad} is the energy flux of solar radiation, which is the energy of the monthly average daily horizontal global radiation H [55]. Therefore, the maximum efficiency of converting the monthly average daily radiation on a horizontal plane is given as:

$$\psi = \frac{H_{ex}}{H} \quad (5.6)$$

The models presented here is, therefore based on several climatic conditions:

$$\frac{H_{ex}}{H_o} = f(A, B, C, D, N, N_o, T_a, V) \quad (5.7)$$

where N , T_a , V represent the measured monthly mean values of the number of sunny hours, the mean temperature, and the mean wind velocity, respectively. A , B , C , D are the coefficients for the empirical models of solar radiation exergy. We introduce two variations of this approach.

Model 4 (present approach I) is based on the horizontal extraterrestrial radiation H_o , and includes the number of sunny hours N , the day length N_o , and the mean temperature T_a as follows:

$$\frac{H_{ex}}{H_o} = A + B \frac{N}{N_o} + CT_a \quad (5.8)$$

Model 5 (present approach II) account for the mean velocity v , in addition to the parameters considered in Model 4. The formulation is given as:

$$\frac{H_{ex}}{H_o} = A + B \frac{N}{N_o} + CT_a + DV \quad (5.9)$$

The models discussed here are summarised in Table 5.1.

Table 5.1 Empirical models used in this paper to predict the energy and exergy values of the monthly average daily horizontal global radiation [48, 51, 53, 55].

#	Models	Solar radiation equations	Solar radiation exergy equations	Independent parameters
1	Linear	$\frac{H}{H_o} = a + b \frac{N}{N_o}$	$\frac{H_{ex}}{H_o} = A + B \frac{N}{N_o}$	H_o, N, N_o
2	Quadratic	$\frac{H}{H_o} = a + b \frac{N}{N_o} + c \left(\frac{N}{N_o} \right)^2$	$\frac{H_{ex}}{H_o} = A + B \frac{N}{N_o} + C \left(\frac{N}{N_o} \right)^2$	H_o, N, N_o
3	Cubic	$\frac{H}{H_o} = a + b \frac{N}{N_o} + c \left(\frac{N}{N_o} \right)^2 + d \left(\frac{N}{N_o} \right)^3$	$\frac{H_{ex}}{H_o} = A + B \frac{N}{N_o} + C \left(\frac{N}{N_o} \right)^2 + D \left(\frac{N}{N_o} \right)^3$	H_o, N, N_o
4	Present I	$\frac{H}{H_o} = a + b \frac{N}{N_o} + cT_a$	$\frac{H_{ex}}{H_o} = A + B \frac{N}{N_o} + CT_a$	$H_o, N,$ N_o, T_a
5	Present II	$\frac{H}{H_o} = a + b \frac{N}{N_o} + cT_a + dV$	$\frac{H_{ex}}{H_o} = A + B \frac{N}{N_o} + CT_a + DV$	$H_o, N, N_o,$ T_a, V

5.2 Locations Considered for the Analysis

In this work, four different sites in Iraq and Turkey are considered to apply solar radiation exergy estimation. First, test data gathered from the four sites between January 1, 2010 and December 31, 2016 is used to evaluate the models. The two sites in Iraq are selected from the locations determined by the Ministry of Electricity in Iraq, where installation of solar power plants is planned to improve the country's electricity infrastructure. All information on climatic conditions for these two locations are taken from the databases of the State Meteorological Service in Iraq. The selected sites in Iraq are characterized as semi-desert region due to deterioration of plant cover and high mean temperature. The first location is Karbala, which is located 90 km southwest of Baghdad. The highest daily energy of solar radiation measured is 26.43 MJ/m²-day in July, whereas the lowest value of 10.08 MJ/m²-day is observed in December. The second location is Shatra, which is 320 km south of Baghdad. The highest daily solar radiation energy of 27.22 MJ/m²-day is indicated in June, whereas the lowest value is observed in December at approximately 10.8 MJ/m²-day.

The other two sites are in Turkey, and selected based on the ongoing research projects carried out under the supervision of Energy Research Centers in Turkey. All data on climatic conditions of the Turkish sites is measured by the State Meteorological Service in Turkey. These sites in Turkey are considered as wet regions due to their high rainfall rates and low mean temperatures. One of these locations is in Istanbul. The highest daily solar radiation energy in Istanbul is 24.94 MJ/m²-day in July, whereas the lowest value of 5.07 MJ/m²-day is recorded in December. Aydin, Turkey, is the fourth site considered in this paper. The highest daily solar radiation energy recorded is 27.60 MJ/m²-day in June, whereas the lowest value is 7.53 MJ/m²-day, as measured in

December. For these sites, the information on location, altitude and data collection period are shown in Table 5.2.

Table 5.2 Location, altitude and data collection period information of the studied sites.

City	Country	Latitude (°N)	Longitude (°E)	Elevation (m)	Duration of Data
Karbala	Iraq	32.55	43.97	29	2010-2016
Shatra	Iraq	31.45	46.19	3	2010-2016
Istanbul	Turkey	41.0	28.6	7	2010-2016
Aydin	Turkey	37.82	27.84	67	2010-2016

In addition, all values of the coefficients of five solar radiation exergy models are presented in Table 5.3.

Table 5.3 Regression coefficients of five conventional and present models for four locations studied.

Site	Function	Model 1 (Linear)	Model 2 (Quadratic)	Model 3 (Cubic)	Model 4 (Present I)	Model 5 (Present II)
Karbala	A	0.2672	0.9022	-4.3714	0.3710	0.3280
	B	0.4002	-1.3640	20.9840	0.1830	0.2150
	C		1.2083	-30.133	0.0022	0.0017
	D			14.542		0.0260
	R2	0.7990	0.8265	0.8379	0.8640	0.915
Shatra	A	0.1394	0.5708	22.534	0.3710	0.3280
	B	0.6113	-0.6263	-94.993	0.1830	0.2150
	C		0.8824	135.55	0.0022	0.0017
	D			-63.835		0.026
	R2	0.5980	0.6007	0.6286	0.8640	0.915
Istanbul	A	0.1733	0.2794	0.4245	0.22	0.306
	B	0.5114	0.0704	-0.8502	0.263	0.226
	C		0.4273	2.2986	0.0053	0.0068
	D			-1.2217		-0.048
	R2	0.8633	0.8696	0.8703	0.886	0.9015
Aydin	A	0.2889	0.1773	1.4629	0.367	0.405
	B		0.9237	-6.8846	0.093	0.048
	C	0.4829	-0.4112	14.73	0.0065	0.0074
	D			-9.5619		-0.051
	R2	0.9305	0.9361	0.9575	0.97	0.974

5.3 Statistical Assessment Models

In previous studies, many researchers have utilized numerous statistical parameters to measure the performance of solar energy estimation models [100-106]. In this work, the five empirical models are validated for seven statistical parameters. The coefficient of determination R^2 is a measure of closeness of the calculated exergy values of the empirical model to the recorded ones. R^2 should be as close as possible to a value of one to one for a model whose performance is enhanced. R^2 can be computed by the following equation [100]:

$$R^2 = \frac{\sum_{i=1}^n (H_{est,ex}(i) - H_{est,ex,avg})(H_{mes,ex}(i) - H_{mes,ex,avg})}{\sqrt{\left[\sum_{i=1}^n (H_{est,ex}(i) - H_{est,ex,avg})^2 \right] \left[\sum_{i=1}^n (H_{mes,ex}(i) - H_{mes,ex,avg})^2 \right]}} \quad (5.10)$$

where $H_{est,ex}$ and $H_{mes,ex}$ are the estimated and measured exergy values of the monthly average daily global radiation, respectively; $H_{est,ex,avg}$ and $H_{mes,ex,avg}$ are the average exergy values of the estimated and measured monthly average daily global radiation, respectively; and n refers to the number of entries.

The root mean square error $RMSE$ defined as an indicator of the short-term performance of the model. The best value of $RMSE$ is zero which indicates a perfect model. The equation that describes $RMSE$ is as follows [104]:

$$RMSE = \left[\frac{1}{n} \sum_{i=1}^n (H_{est,ex}(i) - H_{mes,ex}(i))^2 \right]^{\frac{1}{2}} \quad (5.11)$$

The mean bias error *MBE* gives information about the long-term performance of the model. For a perfect model, *MBE* is zero, and it can be written in the following form [106]:

$$MBE = \frac{1}{n} \sum_{i=1}^n (H_{est,ex}(i) - H_{mes,ex}(i)) \quad (5.12)$$

The mean absolute bias error *MABE* measures the average of absolute values of bias errors. The *MABE* value is zero for a perfect model. *MABE* can be calculated as [102]:

$$MABE = \frac{1}{n} \sum_{i=1}^n |H_{est,ex}(i) - H_{mes,ex}(i)| \quad (5.13)$$

The mean percentage error *MPE* indicates the average percentage variation between estimated and measured exergy values. *MPE* is zero for a perfect model. *MPE* is calculated as [105]:

$$MPE = \frac{1}{n} \sum_{i=1}^n \left(\frac{H_{est,ex}(i) - H_{mes,ex}(i)}{H_{mes,ex}(i)} \right) \times 100 \quad (5.14)$$

The mean absolute percentage error *MAPE* is defined as the average of absolute values of percentage variation between the values of estimated and measured exergy. For the ideal model, *MAPE* is zero. *MAPE* is expressed by [103]:

$$MAPE = \frac{1}{n} \sum_{i=1}^n \left(\left| \frac{H_{est,ex}(i) - H_{mes,ex}(i)}{H_{mes,ex}(i)} \right| \right) \times 100 \quad (5.15)$$

The t-statistic t_{st} assesses the performance of models. The performance of models is inversely proportional to its t_{st} value. t_{st} is obtained as [101]:

$$t_{st} = \sqrt{\frac{(n-1)MBE^2}{RMSE^2 - MBE^2}} \quad (5.16)$$

The performance assessment of the models computed from the statistical comparison methods is presented for four locations in Table 5.4.

Table 5.4 Statistical parameters of five models for the sites in Iraq and Turkey.

Site	Function	Model 1 (Linear)	Model 2 (Quadratic)	Model 3 (Cubic)	Model 4 (Present I)	Model 5 (Present II)
Karbala	RMSE	0.4513	0.4303	0.4140	0.3808	0.3766
	MBE	-0.0701	-0.0775	-0.0755	-0.0292	-0.0004
	MABE	0.2989	0.2900	0.3250	0.3074	0.3104
	MPE	0.1037	0.0744	0.0626	0.0039	0.0776
	MAPE	1.9468	1.9669	2.0835	1.9556	1.8603
	t_{st}	0.5213	0.6073	0.6148	0.2553	0.0032
Shatra	RMSE	0.8640	0.8768	0.8077	0.8788	0.7042
	MBE	-0.1352	-0.1361	-0.0512	-0.3943	-0.1328
	MABE	0.7217	0.7198	0.6237	0.7093	0.6289
	MPE	0.2185	0.2244	0.6187	-1.6849	-0.3329
	MAPE	4.1760	4.1156	3.6928	3.6152	3.4127
	t_{st}	0.5255	0.5210	0.2106	1.6650	0.6371
Istanbul	RMSE	0.8037	0.7921	0.8019	0.7839	0.7972
	MBE	0.0418	0.0366	0.038	0.0381	-0.0234
	MABE	0.6705	0.6449	0.6537	0.6173	0.5921
	MPE	0.4292	0.4234	0.4205	0.566	0.0542
	MAPE	5.8637	5.4370	5.3616	5.0789	4.7062
	t_{st}	0.1727	0.1534	0.1576	0.1616	0.0976
Aydin	RMSE	0.5463	0.496	0.365	0.329	0.2981
	MBE	-0.0459	-0.0325	-0.0279	-0.0256	-0.0027
	MABE	0.4005	0.4144	0.3169	0.2793	0.2533
	MPE	0.105	0.0872	0.0783	-0.0783	0.0287
	MAPE	2.3868	2.5894	2.1202	1.8224	1.6927
	t_{st}	0.2801	0.2181	0.2541	0.2595	0.0308

5.4 Results and Discussions

In this Chapter, we calculated radiation exergies of solar systems using the models given in Table 5.1. We have determined the methods to be used to judge the merits and demerits of the following two concepts: (1) the maximum efficiency for solar radiation and (2) the empirical models of solar radiation exergy. They are presented in the following subsections.

5.4.1 Maximum Efficiency for Solar Radiation

As pointed out in Table 5.1 in Chapter two, the monthly variations for the maximum efficiency of solar radiation results calculated by the expressions of Petela, Spanner, Jeter, and the present approaches are shown in Figures 5.1 to 5.4. In the calculations, mean temperatures are utilized for the four locations studied.

The current work shows similar predictions to Petela and Spanner's results because these approaches deal with the effect of radiation heat transfer. By contrast, Jeter's approach yields results in efficiency of approximately 2% higher.

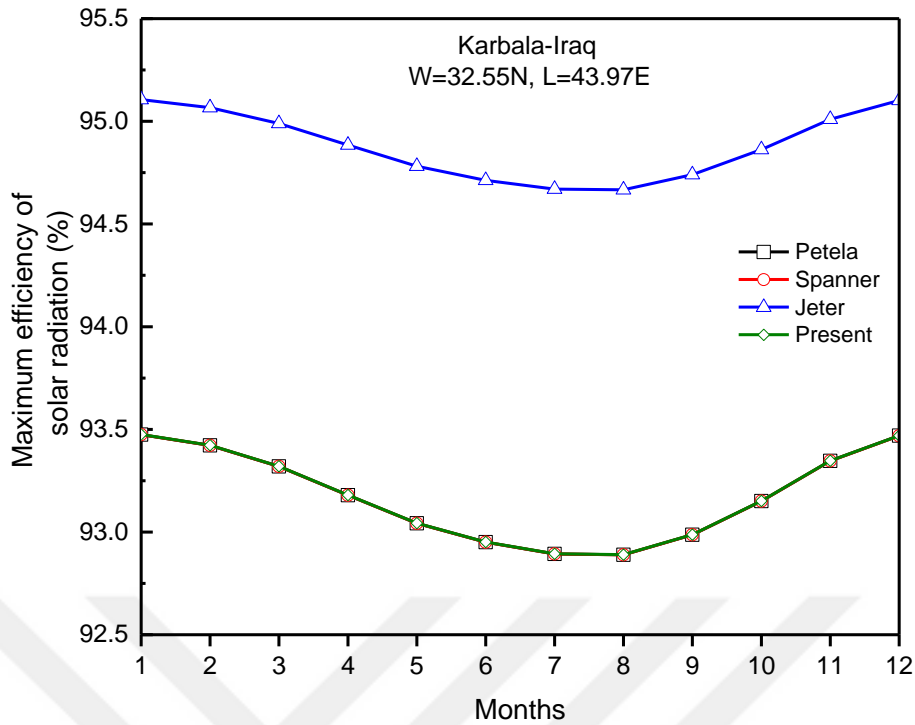


Figure 5.1 Maximum efficiency of average solar radiation (Petela, Spanner, Jeter, and Present Approach, see Table 3.1) at mean temperatures for the site in Karbala, Iraq.

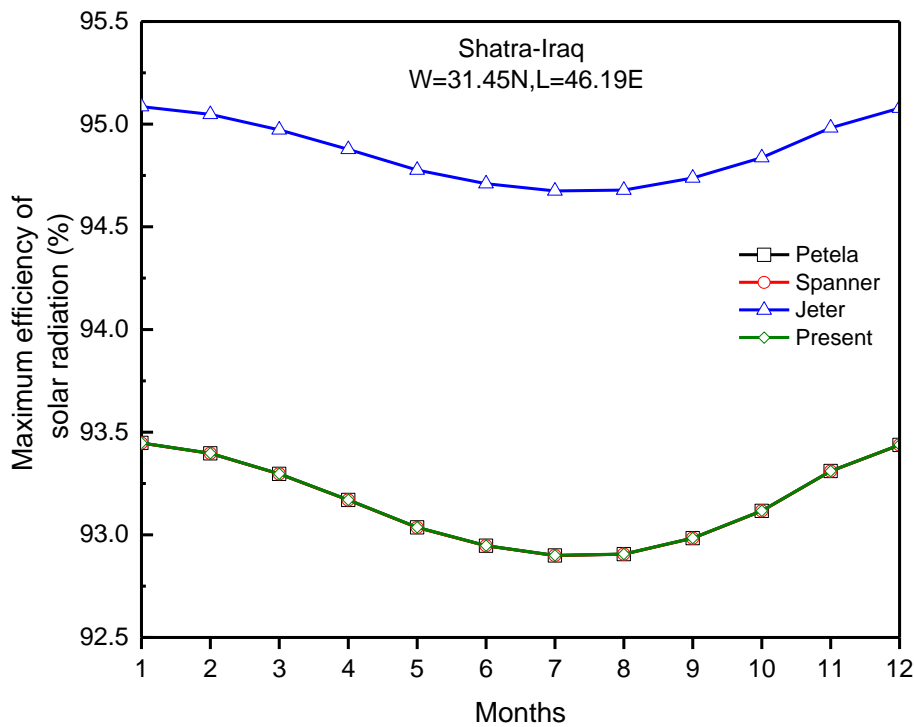


Figure 5.2 Maximum efficiency of average solar radiation (Petela, Spanner, Jeter, and Present Approach, see Table 3.1) at mean temperatures for the site in Shatra, Iraq.

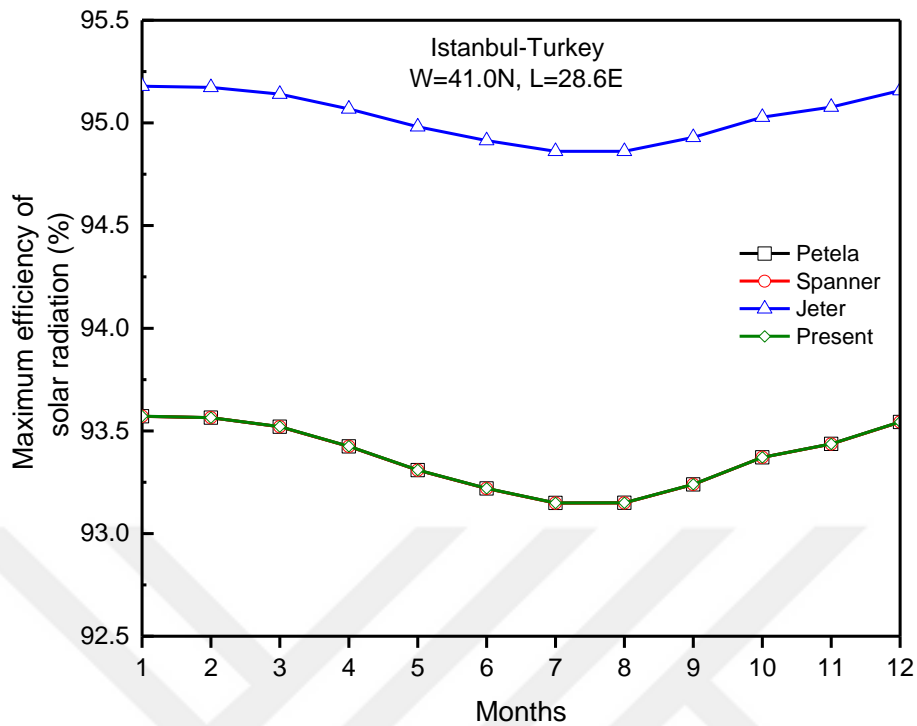


Figure 5.3 Maximum efficiency of average solar radiation (Petela, Spanner, Jeter, and Present Approach, see Table 3.1) at mean temperatures for the site in Istanbul, Turkey.

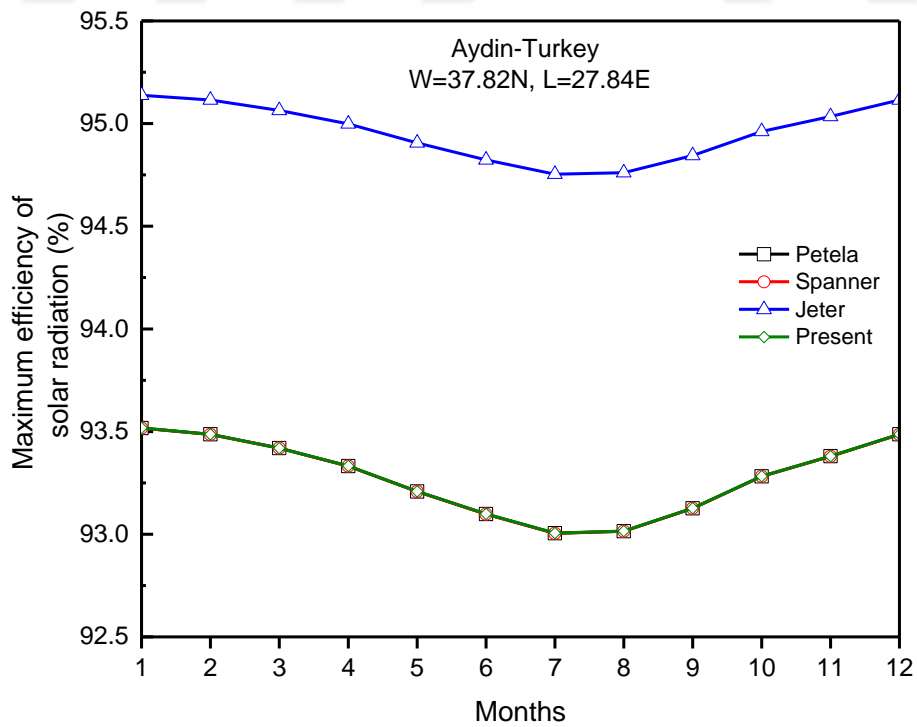


Figure 5.4 Maximum efficiency of average solar radiation (Petela, Spanner, Jeter, and Present Approach, see Table 3.1) at mean temperatures for the site in Aydin, Turkey.

Results depicted in Figures 5.1 to 5.4 show the mean temperature of the months and maximum efficiency are inversely proportional for all approaches and the sites. In Karbala, Iraq, the maximum efficiency calculated by the present expression reached the highest value (0.934) in January when the mean temperature is 10.8°C, which is minimum value of the year whereas the lowest value of maximum efficiency (0.928) is obtained in August at 36.3°C mean temperature, which is the maximum value of the year. Similarly, in Shatra, the best value of maximum efficiency (0.934) is obtained in February when the mean temperature is at yearly minimum 12°C, whereas the lowest value is (0.929) is obtained in July when the maximum value of the mean temperature is reached at 35.9°C. In Istanbul, Turkey, the highest (0.935) and lowest (0.931) values of maximum efficiency can be found in January and July when the mean temperature is 6.7°C and 25°C, respectively. In the same trend, the highest value of maximum efficiency is 0.935 at a minimum mean temperature of 9°C in January, whereas the lowest efficiency is 0.93 at the maximum mean temperature of 31°C in July for Aydin, Turkey.

5.4.2 The Empirical Models for Solar Radiation Exergy

As discussed in section 5.2, we have implemented a detailed investigation of solar radiation exergy with different empirical models as shown in Table 5.1. The regression coefficients for the five models of solar radiation exergy are given in Table 5.4. Figures 5.5 to 5.8 for four cities, show the differences between measured and estimated exergy values of horizontal global irradiation for five models.

The results obtained from Model 1 (linear) and Model 2 (quadratic) for three sites were poor compared with other models except for Aydin. In the same trend, the R^2 values exceed 90% for Aydin and were less for other locations. The predictions of Model 3 (cubic) seem more acceptable because the R^2 value of Model 3 is higher than R^2 values

in Model 1 and 2. On the other hand, global radiation exergy predictions of Model 4 (present approach I) are quite satisfactory when compared to the measured values. Likewise, estimates of Model 5 (present approach II) are better. In this model, the R^2 values are always more than 90% for all locations studied. As shown in Table 5.3, for Model 5, the R^2 values are 91.5%, 91.5%, 90.15%, and 97.4% for Karbala, Shatra, Istanbul, and Aydin, respectively.

The monthly average daily horizontal global radiation exergy values predicted by all models are calculated for the four sites chosen, and then as can be seen from Table 5.3. The performances of these five models are tested by various statistical indicators, which are $RMSE$, MBE , $MABE$, MPE , $MAPE$, and t_{st} for each model and site. For Karbala, the lowest values of statistical indicators $RMSE$, MBE , $MAPE$, and t_{st} are computed by Model 5 as 0.3766, -0.0004, 1.8603, and 0.0032, respectively. The best $MABE$ and MPE values resulted from Model 2 and Model 4 are 0.29 and 0.0039, respectively. The exergy of solar radiation for Karbala changes between 9.42 and 24.55 MJ/m²-day between the months of December and July, respectively. For the second site, Shatra, the optimal values of $RMSE$ and $MAPE$ is obtained from Model 5 which are 0.7042 and 3.4127, respectively. The best value of MPE is obtained from Model 1 which is 0.2185, whereas the best values of MBE , $MABE$, and t_{st} which are -0.0512, 0.6237 and 0.2106, respectively, are computed by using Model 3. For Shatra, the extremum values of solar radiation exergy are 10.14 to 25.3 MJ/m²-day in December and June, respectively. The best MBE , $MABE$, MPE , $MAPE$, and t_{st} values for Istanbul are given by Model 5 as -0.0234, 0.5921, 0.0542, 4.7062, and 0.0976, respectively, whereas the lowest value of $RMSE$ is obtained by using Model 4, which is 0.7839. The lowest value of solar radiation exergy was 4.74 MJ/m²-day in December, and the highest value was 23.23 MJ/m²-day in July for Istanbul. On the other hand, the lowest values of indicators

$RMSE$, MBE , $MABE$, MPE , $MAPE$, and t_{st} for Aydin are 0.2981, -0.0027, 0.2533, 0.0287, 1.6927, and 0.0308, respectively, which are provided by Model 5. The lowest and highest solar radiation exergy for Aydin are 7.04 and 25.7 MJ/m²-day in the months of December and June, respectively.

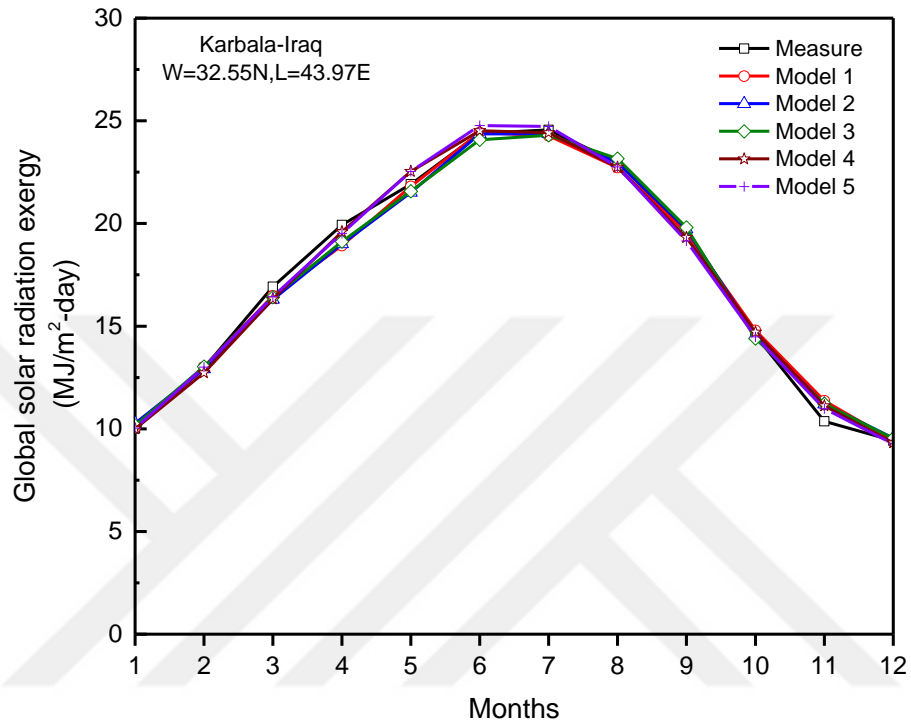


Figure 5.5 Estimated and measured exergy values of the global radiation in Karbala, Iraq. (Based on the information provided in Tables 5.1 and 5.3).

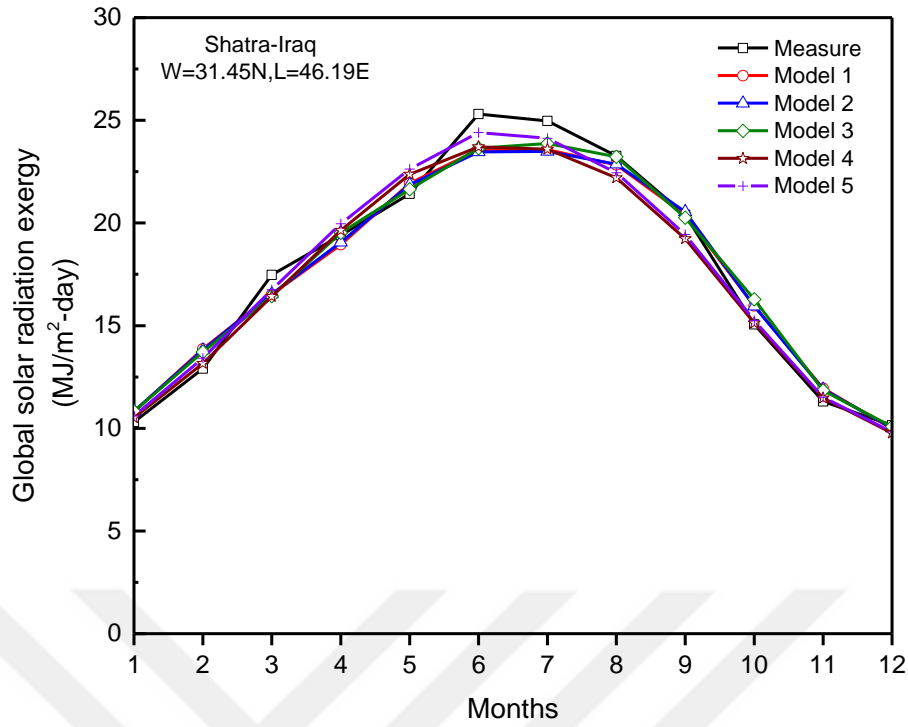


Figure 5.6 Estimated and measured exergy values of the global radiation in Shatra, Iraq. (Based on the information provided in Tables 5.1 and 5.3).

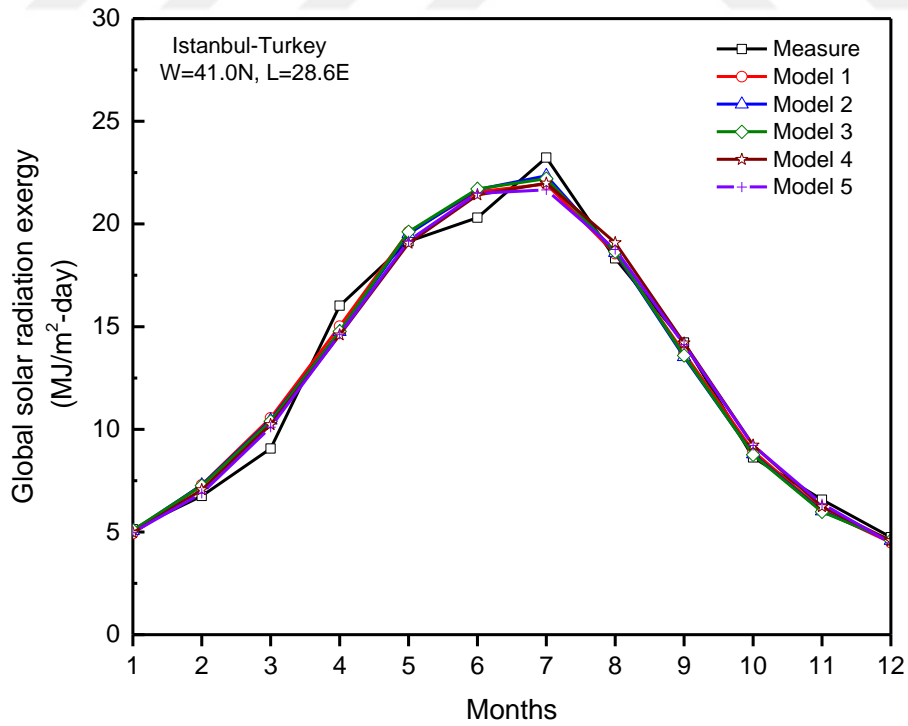


Figure 5.7 Estimated and measured exergy values of the global radiation in Istanbul, Turkey. (Based on the information provided in Tables 5.1 and 5.3).

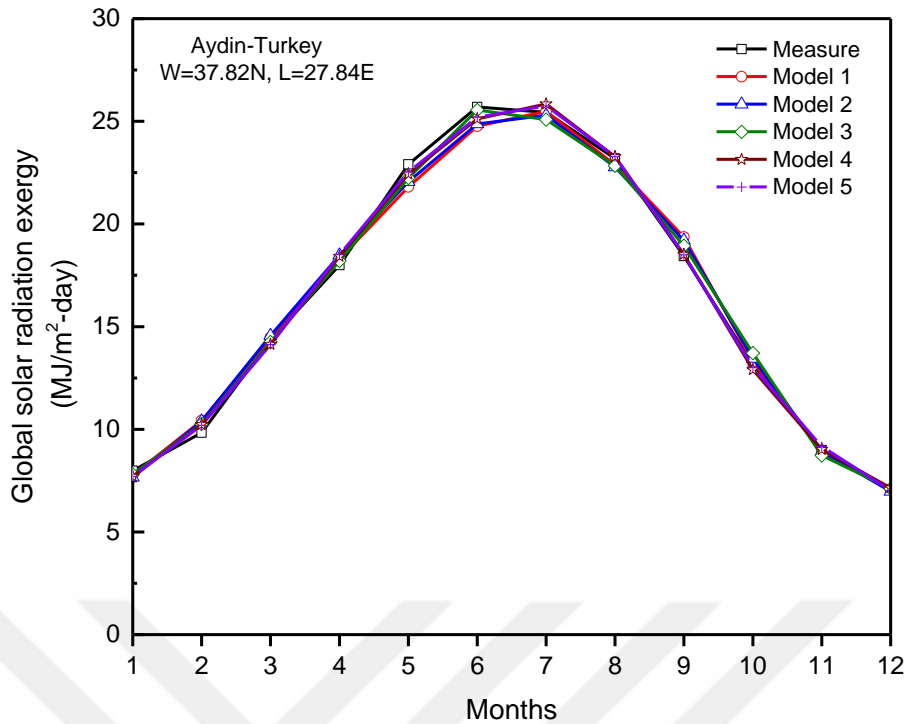


Figure 5.8 Estimated and measured exergy values of the global radiation in Aydin, Turkey (Based on the information provided in Tables 5.1 and 5.3).

The best values of MBE , MPE , and t_{st} are produced by Karbala, whereas the best values of $RMSE$, $MABE$, and $MAPE$ are computed in Aydin using the models developed in this work. The values of statistical indicators might be considered to be acceptable, except for $MAPE$. In summary, the estimated global radiation exergy value at each location is acceptable when compared with the measured values. The present models (4 and 5) produce the best values of statistical tests. Model 5 has less residual than the other models. Thus, this model can estimate the horizontal global radiation exergy most reliably.

5.5 Summary

In this Chapter, a new methodology is introduced for predicting solar radiation exergy. The empirical models are assessed by the statistical parameters to predict the exergy value of the monthly average daily horizontal solar radiation in Iraq and Turkey.

The results show the losses caused by radiation heat transfer are higher than those resulting from the other modes of heat transfer because the energy transfer via radiation is proportional to the fourth power of the temperature. Also, the monthly variations of maximum conversion efficiencies are found to be quite small. We note that the R^2 values of Model 5 can provide additional evidence on the effects of weather condition parameters on the accuracy of the empirical models based on measurements in Iraq and Turkey.

The statistical parameters ($RMSE$, MBE , $MABE$, MPE , $MAPE$, and t_{st}) show that the proposed empirical models can be adopted in Iraq and Turkey for academic and industrial applications. The Model 5 seems to provide the most reliable results, and is considered to be the best.

CHAPTER VI

THERMAL AND RADIATIVE PERFORMANCE ANALYSES OF A PTC SYSTEM

6.1 Description of the PTC System

In this Chapter, the solar field established with the help of EU-FP7-BRICKER project is considered. The system includes ten rows of solar PTC systems (PTMx-36) that are designed and manufactured by Soltigua [14]. The system is divided into five hydraulic loops of two concentrator rows, located in Aydin province of Turkey, in the campus of Adnan Menderes University (ADU). Figure 6.1 shows that the rows are arranged solar field.

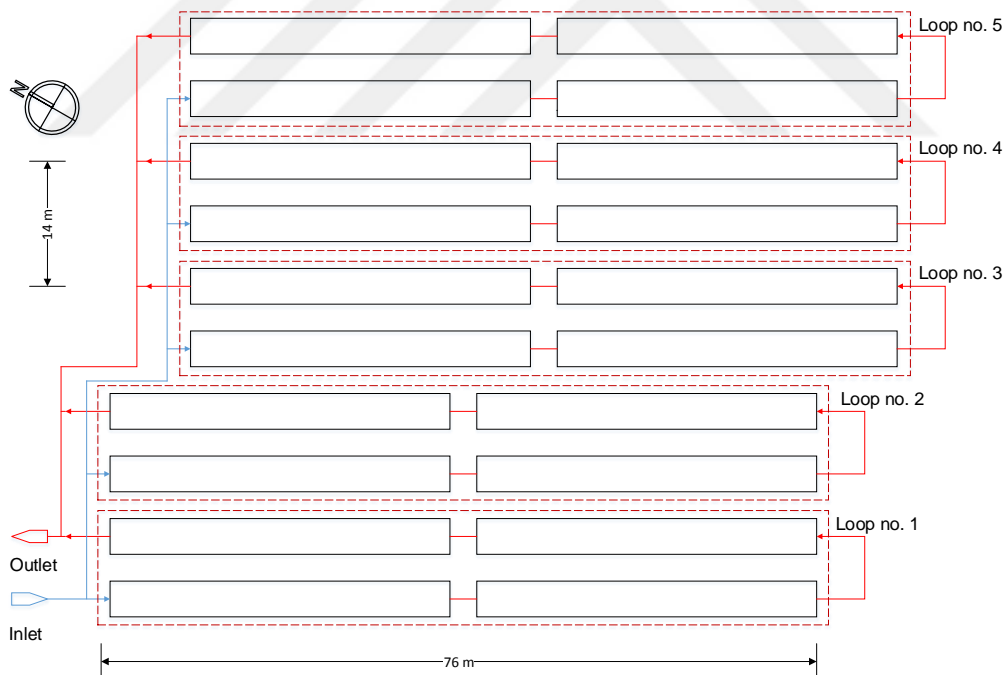


Figure 6.1 Scheme of the solar field layout at ADU Campus, Aydin, Turkey.

An estimated overall thermal power provided by the PTC field corresponds to approximately 1 MW. The project mainly aims to save more than 50% of the required

energy for different applications with the help of a tri-generation system, which include electricity, air conditioning and heating for a building nearby used as a teaching hospital. This project is constructed in Adnan Menderes University, Aydin, a province in Turkey which was chosen because of the favorable solar radiation intensity throughout the year. All data on climatic conditions of this Turkish site are measured by the State Meteorological Service in Turkey for Aydin [107].

The solar field was designed for single axis tracking PTCs. All instruments were equipped with a programmable logic controller (PLC) which allows an automatic remote control, including stowing procedures in case of bad weather, strong wind, overheating or insufficient flow rate, to prevent damages.

The reflector is made of a high reflectance glass and silver. Each mirror has four sufficient stiffness points to hold of a steel structure. Another attractive feature of the PTMx is that it has a small aperture width to simplify cleaning and to reduce the wind forces which is transmitted to the foundations. The third characteristic of the PTMx is hot dip galvanized metal structure which keeps it from corrosion under outdoor conditions. Receivers compose from absorbers and the glass envelope without evacuating between them. The welding between absorbers may cause reduction of durability; therefore, absorbers were bolted one by one. Figure 6.2 shows the connection absorbers, the tracking system, and the solar field.



Figure 6.2 A-the connection absorbers, B-the tracking system, and C-the solar field.

The overall energy system is divided into three parts based on the type of working fluid used. Energy generation units (EGUs) use oil, energy distribution units (EDUs) use water, and energy conversion units (ECUs) have both oil and water.

- EGUs generate useful energy by utilizing solar energy incident. Thermal oil groups are selected for the EGUs to satisfy the required temperature ranges of working fluid throughout thermal cycle.

- ECUs' the primary purpose is the conversion of thermal energy from the oil loop into either electrical or thermal energy in the water loop.

- EDUs are responsible for meeting cooling loads by using adsorption units.

The possibility of using steam or pressurized hot water as HTF in place of oil has been rejected due to the excessive pressures required by operating temperature over 200°C [108].

Dimensional parameters are based on data provided by the PTC manufacturer Soltigua. The PTC commercial model considered in the system design is PTMx-36, whose main characteristics and operational limits are gathered in Table 6.1.

Table 6.1 Characteristics and operational limits of PTC model PTMx-36 by Soltigua [108].

Parameter	Value	Unit
Collector width	2.37	m
Focal distance	0.8	m
Absorber internal diameter	38.4	mm
Absorber external diameter	42.4	mm
Absorber thermal conductivity	stainless steel 316L	
Glass cover internal diameter	75.8	mm
Glass cover external diameter	80	mm
Selective coating of the absorber	Cermet coating	
Absorptivity of absorber surface	0.94	
Emissivity of absorber surface	0.18	
Emissivity of glass envelope	0.88	
Transmissivity of glass envelope	0.93	
Reflectivity of the mirror	0.94	
Heat transfer fluid	Therminol-55	
Number of Loops	5	
Length of each loop	144	m
Inclination angle	0°	
Nominol flow rate for each loop	6	m ³ /hr
Inlet temperature	142	°C
Maximum oil temperature	250	°C
Maximum working pressure	8	bar
Minimum oil flow rate (200-250°C)	20	l/min
Maximum oil flow rate	120	l/min

6.2 Optical Analysis

Below, the optical performance of the PTC is discussed first. The equations for geometry factors are defined using the geometry shown in Figure 6.3.

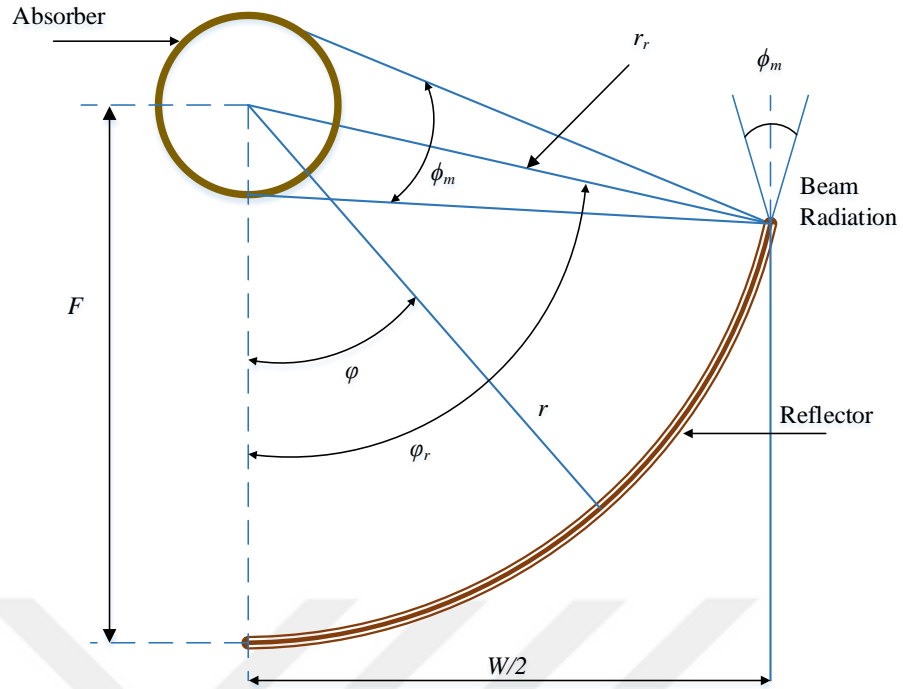


Figure 6.3 Geometry of parabolic trough collector.

6.2.1 Geometry of PTC

Solar concentrating system is based on PTC mechanism. For this, we need to start with the formula for a parabola. In Cartesian (x, y) coordinates, it is given by following relation [109] :

$$x^2 = 4Fy \quad (6.1)$$

where F is the focal distance. The rim angle (φ_r) is the relevant parameter to determine the ‘flatness’ of the external form of a parabola, and can be computed from Figure 6.3 [109]:

$$\tan \varphi_r = \frac{W/2}{F - y} \quad (6.2)$$

where W is the width of PTC. Substituting Eq. (6.1) into (6.2) and letting $x = \frac{W}{2}$ yields:

$$\tan \varphi_r = \frac{8F/W}{16(F/W)^2 - 1} \quad (6.3)$$

The solar concentration ratio (C) is defined as the ratio between the aperture area (A_a) to outer area of absorber pipe (A_3). Then, it is calculated as [95]:

$$C = \frac{A_a}{A_3} = \frac{(W - d_3)L}{\pi d_3 L} = \frac{W - d_3}{\pi d_3} \quad (6.4)$$

The acceptance angle (ϕ_m) is defined as the maximum angle describes the range of the incident angle of solar radiation on reflector which is captured by an absorber pipe. The minimum acceptance angle in practice is 32' based on the solid angle of the Sun sphere that can be seen from the Earth [66]. The diameter (d_3) of the outer absorber pipe is determined as [24]:

$$d_3 = 2r_r \sin(\phi_m / 2) \quad (6.5)$$

where r_r is the rim radius, and can be obtained as [109]:

$$r_r = \frac{2F}{1 + \cos \varphi_r} \quad (6.6)$$

The width of the parabolic mirror can be obtained using the following equation [109]:

$$W = 2r_r \sin \varphi_r \quad (6.7)$$

Substituting Eq. (6.6) into (6.7) and using the double angle formula

$\sin \varphi_r = 2 \sin \frac{\varphi_r}{2} \cos \frac{\varphi_r}{2}$ and half angle formula $1 + \cos \varphi_r = 2 \cos^2 \frac{\varphi_r}{2}$, Eq. (6.7) can be

rewritten as:

$$W = \frac{4F \sin \varphi_r}{1 + \cos \varphi_r} = 4F \left[\frac{2 \sin \frac{\varphi_r}{2} \cos \frac{\varphi_r}{2}}{2 \cos^2 \frac{\varphi_r}{2}} \right] = 4F \left(\frac{\sin \frac{\varphi_r}{2}}{\cos \frac{\varphi_r}{2}} \right) = 4F \tan \frac{\varphi_r}{2} \quad (6.8)$$

Inserting Eq. (6.8) into (6.5). The diameter of absorber pipe can be calculated as:

$$d_3 = 2 \left(\frac{W}{2 \sin \varphi_r} \right) \sin(\phi_m / 2) = W \frac{\sin(\phi_m / 2)}{\sin \varphi_r} \quad (6.9)$$

6.2.2 Solar Radiation Input

The amount of solar radiation (S) absorbed depends on the radiative properties of the PTC materials, geometrical collector and different defects produced from the construction of the PTC. The solar radiation absorbed is [110]:

$$S = I_b \rho_{ref} \tau_g \alpha_{abs} \gamma \varepsilon_t K(\theta) A_f A_a \quad (6.10)$$

where I_b is the incident solar radiation, ρ_r is the reflectivity of the mirror, τ_g is the transmissivity of the glass envelope, α_a is the absorptivity of the surface absorber, γ is the intercept factor, ε_t is the total miscellaneous loss factor, $K(\theta)$ is the incident angle modifier, A_f is the collector geometric factor and A_a is the aperture area. They are discussed in detailed below.

6.2.2.1 Intercept Factor

The intercept factor is considered to determine the optical efficiency of the system. The factor is defined as the portion of the reflected radiation that is intercepted by the absorber. Under ideal conditions, the intercept factor is equal to 1. However, in real operation conditions, several errors made this factor less than 1. Such errors include manufacturing and assembly errors, these caused by the tracking system and from misalignment problems. These errors are categories as the random and non-random errors. Random errors (σ) include random tracking error (σ_{sun}), random error in manufacturing and assembly (σ_{slope}), and random error produced from optical properties for the mirror (σ_{mirror}). These random errors are computed by a statistical approach which determines the standard deviation of the total reflected energy distribution at normal incident. The total random error can be determined as [111]:

$$\sigma = \sqrt{\sigma_{sun}^2 + \sigma_{slope}^2 + \sigma_{mirror}^2} . \quad (6.11)$$

Non-random errors refer to the errors associated with operations and imperfections of manufacturing. These errors show how to deviate radiation from the design focal point. Random and non-random errors can be calculated using the universal error parameter. Then, the intercept factor (γ) can be determined by using the following equation [112]:

$$\gamma = \frac{1 + \cos \varphi_r}{2 \sin \varphi_r} \int_0^{\varphi_r} Erf \left\{ \frac{\sin \varphi_r [1 + \cos \varphi] [1 - (2d_r / d_3) \sin \varphi] - \pi \beta C [1 + \cos \varphi_r]}{\sqrt{2} \pi \sigma C [1 + \cos \varphi_r]} \right\} - Erf \left\{ - \frac{\sin \varphi_r [1 + \cos \varphi] [1 + (2d_r / d_3) \sin \varphi] + \pi \beta C [1 + \cos \varphi_r]}{\sqrt{2} \pi \sigma^* [1 + \cos \varphi_r]} \right\} \times \frac{d\varphi}{(1 + \cos \varphi)} \quad (6.12)$$

where d_r is the dislocated distance between the ideal focus and the real focus of receiver, and β is the misalignment and tracking errors.

6.2.2.2 The Miscellaneous Loss Factors

These parameters are generated from experimental data and can be adopted from NREL, and the total miscellaneous loss factor (ε_t) can be calculated by the following equation [64]:

$$\varepsilon_t = \varepsilon_1' \varepsilon_2' \varepsilon_3' \quad (6.13)$$

Table 6.2 shows the values of the miscellaneous loss factors.

Table 6.2 Estimation of the miscellaneous loss factors [64].

Term	Value
HCE Shadowing ε_1'	0.974
Dirt on mirror ε_2'	ρ_r / ρ_{cl}
Dirt on HCE ε_3'	$(1 + \varepsilon_2') / 2$
Clean mirror reflectance ρ_{cl}	0.935

6.2.2.3 Incident Angle Modifier

The incident angle modifier ($K(\theta)$) is defined as the ratio of thermal efficiency at a specific incident angle to the maximum efficiency at normal incident angle. It considers the effect of incident angle [113]. Moreover, the value of solar radiation reaching the PTC relies on the incident angle. For this purpose, several modes of tracking are designed to control the orientation of the PTC towards the Sun. The incident solar radiation is proportional to the incident angle modifier which depends on the geometry of the PTC. Experimental data regarding the incident angle modifier for different values of incident

angle are also provided by the company [108]. The fitting curve equation can be obtained from Figure 6.4 as:

$$K(\theta) = 0.9998 - 0.0003\theta - 0.0002\theta^2 + (6E-10)\theta^3 \quad (6.14)$$

where θ is the incident angle and can be computed for the collector rotating in north-south axis, which is given as follows [66]:

$$\cos \theta = \sqrt{\cos^2 \theta_z + \sin^2 \omega \cos^2 \delta} \quad (6.15)$$

where θ_z is the zenith angle, ω is the hour angle and δ is the solar declination angle that is an angle between a connecting line between the Earth and Sun and the line project on the Earth's equator. The zenith angle (θ_z) refers to the angle between the beam solar radiation and the vertical of a horizontal surface. It can be determined by the following equation [109]:

$$\cos \theta_z = \cos \phi \cos \delta \cos \omega + \sin \phi \sin \delta \quad (6.16)$$

where ϕ is the latitude angle. The hour angle (ω) is the angular distance of the sun west or east of the local meridian as a result of the rotation of the earth afternoon on its positive axis and morning on its negative axis.

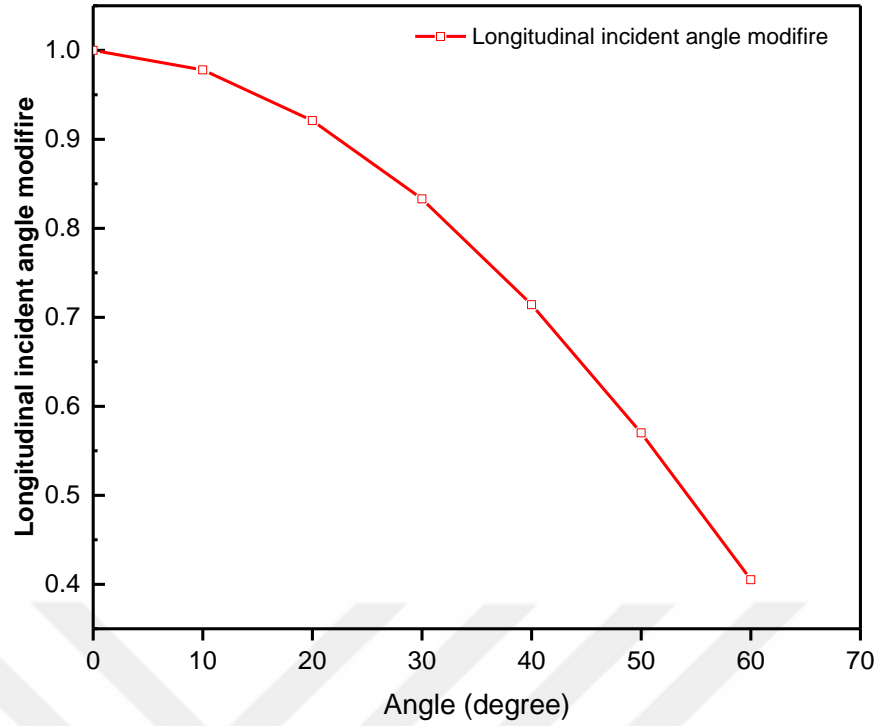


Figure 6.4 Incident angle modifier of PTC model PTMx-36 [108].

6.2.2.4 Collector Geometric Factor

Geometric factor refers to the effect of the reduction of the aperture area caused by shading, the end-effect and another effect which can occur because of the arrangement of the collectors in parallel arrays. It is described as follows [110]:

$$A_f = 1 - \left[\frac{d_3}{L} + \frac{F}{L} \left(1 + \frac{W^2}{48F^2} \right) \right] \tan \theta \quad (6.17)$$

6.2.2.5 Optical Efficiency

Optical efficiency (η_{op}) is defined as the ratio of solar energy that reaches the receiver to the incident beam solar radiation on the collector. Thus, the following equation can be determined [109]:

$$\eta_{op} = \frac{S}{I_b A_a} = \rho_{ref} \tau_g \alpha_{abs} \gamma \epsilon_t K(\theta) A_f \quad (6.18)$$

6.3 Energy Analysis

Energy analysis specifies the energy absorbed by the HTF and determines the energy losses from the receiver to the ambient as a result of the heat transfer (conduction, convection, and radiation). Figure 6.5 explains the heat transfer through HCE, and Figure 6.6 shows the thermal resistance model used in the heat transfer analysis. The thermal analysis model contains the equations of energy which is used to do an energy balance between the HTF and the environment.

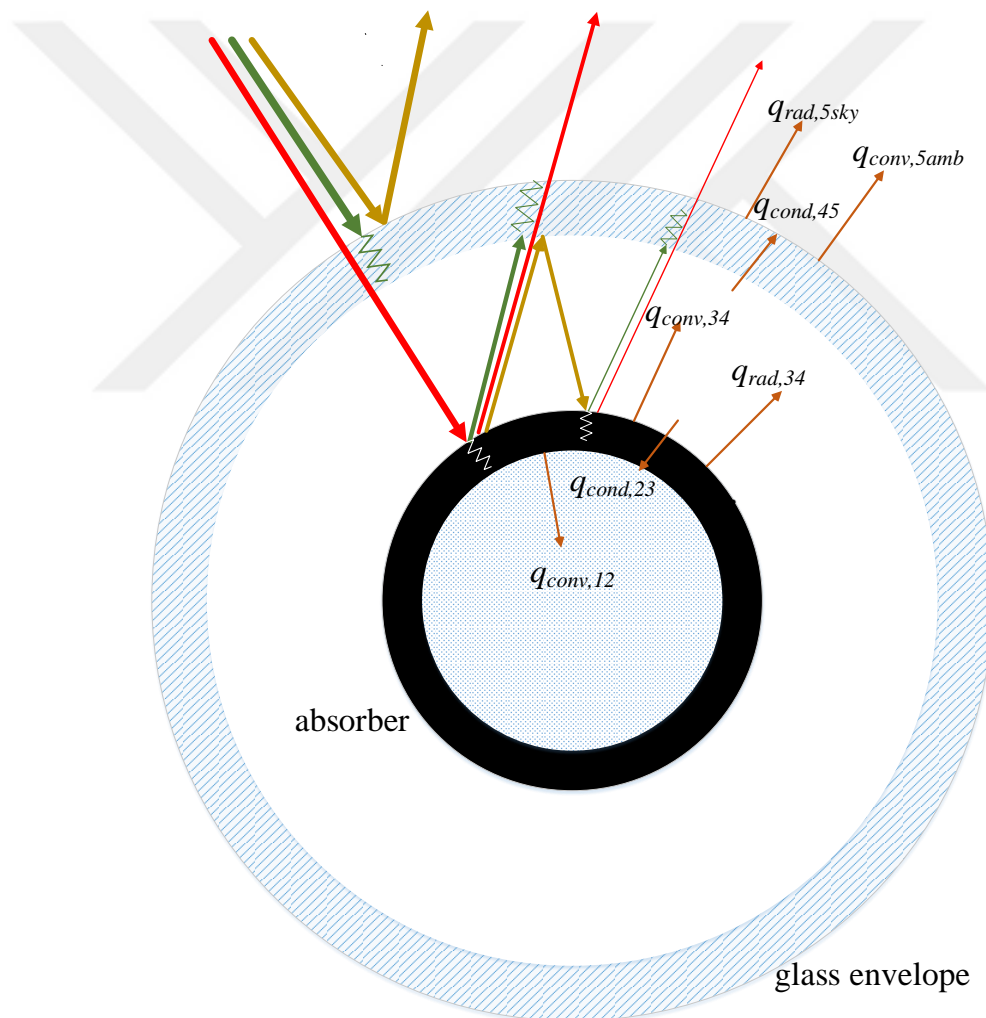


Figure 6.5 Scheme for the heat transfer mechanism through heat transfer collector element.

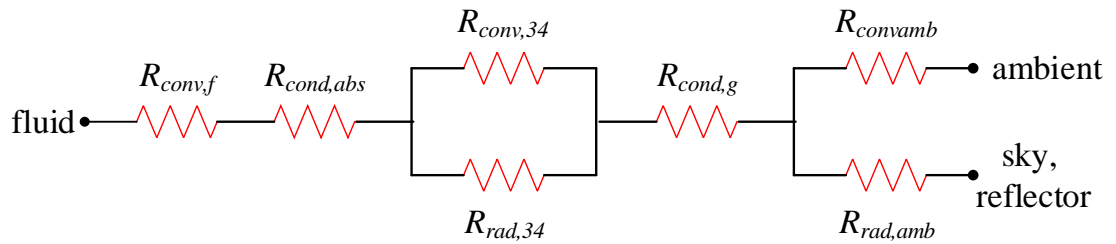


Figure 6.6 Thermal resistance model for the parabolic trough collector system.

In a PTC system such as the one shown in Figure 6.5, the solar radiation is captured and concentrated by a reflector which is divided into three parts. The first part is reflected by glass envelope. The next part is absorbed by glass. After absorbing, the second part is emitted because of increasing the temperature of glass. The third part transmits the crucial part to absorber. The most percentage of the third part is absorbed by the selective surface and transferred through a wall by conduction and to the fluid by convection as a useful energy. Once the radiation is absorbed, the temperature of the surface increases. Therefore, the energy is emitted as heat losses from the absorber surface. The remaining percentage of the third part is reflected by the absorber in the direction of inner surface of glass. This percentage is then transmitted outside, absorbed by the glass and again reflected to the absorber. To absorb energy by glass envelope, the emitted energy from the selective surface is transferred by radiation and convection through annular space. Conduction through glass is lost by convection and radiation. In practice, neglecting the effect of the remaining third part is problematic. However, the present analysis considers the effect of all solar radiation parts on the performance of PTC. Moreover, the heat transfer takes place by radiation between glass envelope and sky. The reflector is considered as well.

In the current work, the following major features are included:

1) The PTC analysis is implemented under steady state. Thus, mass or energy is not accumulated in control volume. The thermodynamic properties are independent of time.

2) For short solar collector lengths, a one-dimensional heat transfer provides reasonable results. This is due to the relevant gradient of temperature occurring mostly in the direction of falling solar radiation. The path of radiation is shorter than the length of the absorber. Thus, the change of temperature is neglected in the axial direction of absorber based on bulk temperature, that is, average temperature. However, heat transfer calculations should account for the change in thermodynamic properties and pressure drop provided that the total of solar collector length is longer than 100 m. Therefore, a two-dimensional model is considered to include the effect of temperature variation in the axial direction.

3) In energy balance, the surface of the absorber deal as a constant heat flux surface. Therefore, the bulk temperature of working fluid increases in the flow direction. For the purpose of analysis, the governing equation for steady state is applied to control volume. The length of absorber should be divided into N number of segments to understand the discretization principle. Figure 6.7 shows that $i-1$ and $i+1$ represent the inlet and outlet segment, respectively.

4) Bulk temperature of the centerline is equal to an average temperature between inlet and outlet segment.

5) Work and potential energy are equal to zero (horizontal). In addition, kinetic energy is smaller than other energies, and the surface roughness is uniform.

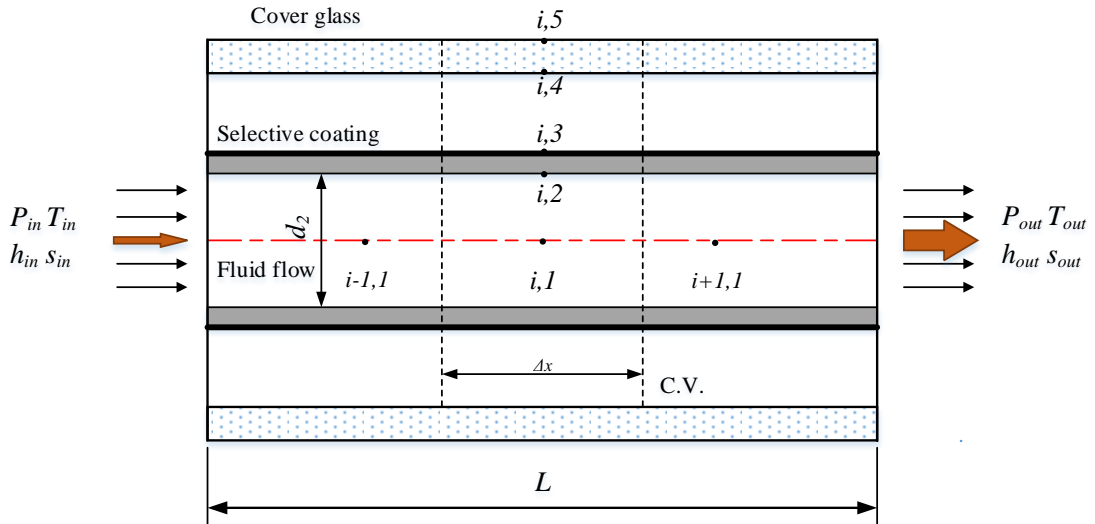


Figure 6.7 Schematic side view of the receiver.

The governing equation of energy applied on control volume has the following form [110]:

$$\left[m e \right]_{i-1}^{i+1} = \sum_{i=1}^N \delta q \quad (6.19)$$

where m is a mass flow rate; q is a rate of heat transfer; e is a specific energy and can be obtained by the following equation:

$$e = h + \frac{V^2}{2} + gz \quad (6.20)$$

where h is a specific enthalpy and $h \cong c_p T$ for incompressible fluid [114], V is a velocity, g is a gravitational constant, z is the high (cancels out for horizontal flow), and T is temperature.

The thermal analysis is estimated by applying thermal resistance shown in Figure 6.6. To estimate the temperature at nodes in resistance network, a number of equations equal to unknown temperatures should be proposed. In addition, the thermodynamic

properties and heat transfer coefficients are unknown because they are based on temperatures. Therefore, these equations are solved by trial-and-error approach. However, EES is one of the software programmes that solve these kinds of problems by using numerical solution. By applying the energy balance at each surface of the heat collector element, the energy balance equations for each part can be written as follows:

$$q_{conv,f} = q_{cond,23} \quad (6.21)$$

$$\eta_o I_b A_a + \eta_o I_b A_a \rho_{abs} \rho_g = q_{conv,34} + q_{rad,34} + q_{cond,23} \quad (6.22)$$

$$\eta_o I_b A_a \rho_{abs}^2 \alpha_g \rho_g / \alpha_{abs} + \eta_o I_b A_a \rho_{abs} \alpha_g / \alpha_{abs} + q_{conv,34} + q_{rad,34} = q_{cond,45} \quad (6.23)$$

$$\eta_o I_b A_a \alpha_g / \tau_g \alpha_{abs} + q_{cond,45} = q_{conv,amb} + q_{rad,amb} \quad (6.24)$$

$$q_l = q_{conv,amb} + q_{rad,amb} \quad (6.25)$$

The analysis based on heat transfer modes identifies the assessment performance of PTC.

6.3.1 Heat Transfer between the Fluid and the Inner Surface of Absorber

By applying Newton's law of cooling between the inner surface of the absorber and fluid to calculate heat transfer by convection, the following equation is obtained [115]:

$$q_{conv,f} = h_f d_2 \pi \Delta x (T_{2,i} - T_{1,i}) \quad (6.26)$$

where h_f is the heat transfer coefficient of fluid, d_2 is the inner diameter of absorber pipe and $T_{i,1}$ and $T_{i,2}$ are the temperature of fluid and the inner absorber surface, respectively.

Heat transfer coefficient can be computed using the Nusselt number correlations, such as:

$$Nu_f = \frac{h_f d_2}{k_f} \quad (6.27)$$

where k_f is the thermal conductivity of fluid at bulk temperature. Nusselt number (Nu_f) depends on Reynolds number (flow type) which determined as:

$$Re_f = \frac{V_f d_2}{\nu_f} \quad (6.28)$$

where V_f and ν_f are the velocity and kinematic viscosity at bulk temperature of a fluid, respectively. Although the type of flow in the absorber is typically turbulent, the model includes conditional statements to specify the type of flow. Laminar flow at Re_f is less than 2,300, thus Nusselt number is given as follows [115]:

$$Nu_f = 4.36 \quad (6.29)$$

The flow in the absorber can be assumed fully developed because the entry length which equals to ten times absorber diameter has a much smaller value than the length of each loop in the solar field. Then, Nusselt number correlation for turbulent flow is developed by Gnielinski [115]:

$$Nu_f = \frac{Pr_f \left(\frac{f}{8}\right) (Re_f - 1000)}{1 + 12.7 \sqrt{\frac{f}{8}} (Pr_f^{2/3} - 1)} \left[1 - \left(\frac{d_2}{L}\right)^{2/3} \right] \left(\frac{Pr_f}{Pr_2}\right)^{0.11} \quad \text{For } 0.5 < Pr_f < 2000 \text{ and } 2300 < Re_f < 5 \times 10^6 \quad (6.30)$$

where Pr_f is the Prandtl number of fluid at bulk temperature, Pr_2 is the Prandtl number at wall temperature of absorber, L is the length of absorber and f is the friction coefficient that can be determined first by correlation [116]:

$$f = (1.82 \log_{10} Re_f - 1.64)^{-2} \quad (6.31)$$

Gnielinski prefers next equation instead of Eq. (6.31) which represents the friction coefficient in pipes as [116]:

$$f = (1.8 \log_{10} Re_f - 1.5)^{-2} \quad (6.32)$$

The pressure drop of fluid flow in each loop for solar field can be calculated using the following equation [117]:

$$\Delta p = \frac{f \Delta x \rho V_f^2}{2d_2} \quad (6.33)$$

In this Chapter, Therminol-55 is used. It is a high-performance HTF with the organic systems. It can also be used for all operating conditions in systems without pressurizing. The best performance is with a temperature of 290°C. In addition, it has thermal stability at operating temperatures and without significant changes in thermal properties when used for years.

6.3.2 Heat Transfer through the Wall of Absorber

By applying the Fourier law of conduction heat transfer to find heat transfer rate through the wall of absorber as the following formula can be obtained [115]:

$$q_{cond,23} = \frac{2\pi k_{23} \Delta x (T_{3,i} - T_{2,i})}{\ln\left(\frac{d_3}{d_2}\right)} \quad (6.34)$$

where k_{23} is the thermal conductivity of absorber wall which depends on the type of stainless steel and the average temperature ($T_{23,i}$) of inner and outer temperatures for absorber wall. Three types of stainless steel (304L, 316L and 321H) are commonly used. Thermal conductivity for 304L and 316L is calculated in units of ($\text{W m}^{-1} \text{K}^{-1}$), by following equation:

$$k_{23} = 0.013T_{23,i} + 15.2. \quad (6.35)$$

The thermal conductivity for 321H is determined as follows:

$$k_{23} = 0.0153T_{23,i} + 14.775. \quad (6.36)$$

Eqs. (6.35) and (6.36) are obtained from fit curve data from Davis [118].

In this work, the absorber of PTMx-36 is made of (316L) stainless steel. It has a high corrosion resistance.

6.3.3 Heat Transfer through the Annular Space

The heat transfer between these two surfaces occurs by two modes of convection and radiation. As previously stated, both modes through annular space in HCE can be considered energy losses due to rise of temperature of outer surface after absorbing the captured solar radiation by the spectrally selective surface.

6.3.3.1 Convection Heat Transfer through the Annular Space

Convection heat transfer relies on the annular space pressure. For this reason, heat transfer occurs in two modes. When the pressure in annular space is less than 100 mmHg, the annulus is considered under vacuum. Thus, heat transfer is obtained by free-molecular convection, and the suggested correlation is given as follows [115]:

$$q_{conv,34} = h_{34} d_3 \pi \Delta x (T_{3,i} - T_{4,i}) \quad (6.37)$$

where h_{34} is heat transfer coefficient by convection through space between cover glass and absorber pipe. It can be computed as follows [64]:

$$h_{34} = \frac{k_{st}}{(d_3/2) \ln(d_4/d_3) + b\lambda(d_3/d_4 + 1)} \quad (6.38)$$

Eq. (6.38) can applied for $Ra_{34} < [d_4/(d_4-d_3)]^4$. k_{st} is the thermal conductivity of the gas in annular space at standard temperature and pressure. b and λ are the interaction coefficient and mean-free-path between collisions of molecules, respectively. These coefficients can be calculated from the following formulas [119]:

$$b = \frac{(2-a)(9\gamma-5)}{2a(\gamma+1)} \quad (6.39)$$

$$\lambda = 2.331 \times 10^{-20} \left(\frac{T_{34,i} + 273}{p_a \delta^2} \right) \quad (6.40)$$

where δ is molecular diameter of gas in annular space, p_a is the gas pressure in annular space, $T_{34,i}$ is the average temperature of outer surface temperature of absorber ($T_{i,3}$) and inner surface temperature of glass envelope ($T_{4,i}$), γ is ratio of specific heat at constant pressure to specific heat at constant volume for the gas in annular space ($\gamma_{air} = 1.39$) and a is the accommodation coefficient that can be determined by the following correlation [120]:

$$a = \exp \left[C_o \left(\frac{T_{3,i} - T_0}{T_0} \right) \right] \left(\frac{M_g^*}{C_1 + M_g^*} \right) + \left\{ 1 - \exp \left[C_o \left(\frac{T_{3,i} - T_0}{T_0} \right) \right] \right\} \left\{ \frac{2.4\mu}{(1+\mu)^2} \right\} \quad (6.41)$$

where $C_o = -0.57$; $C_1 = 6.8$; $T_0 = 273$ K; M_g^* is the monatomic equivalent molecular weight (for monatomic gas $M_g^* = M_g$ and for diatomic/polyatomic gas $M_g^* = 1.4M_g$) and μ is the ratio of molecular weight of gas (M_g) to molecular weight of solid (M_s). This ratio can be calculated as:

$$\mu = \frac{M_g}{M_s} \quad (6.42)$$

Table 6.3 presents the molecular diameter and molecular weight of suggested gases in annular space [121].

Table 6.3 Molecular diameter and molecular weight of suggested gases [121].

Gas	Molecular diameter (cm)	Molecular weight (g/mole)
Air	3.53×10^{-8}	28.97
Argon	3.58×10^{-8}	39.95
Helium	2.15×10^{-8}	4.003
Hydrogen	2.71×10^{-8}	2.01
Carbon dioxide	4.53×10^{-8}	44.01

When the pressure in annular space is more than 100 mm Hg, the natural convection heat transfer occurs from the outer surface of absorber to inner surface of glass envelope. The heat can be determined by the following equation [115]:

$$q_{conv,34} = \frac{2\pi k_{eff} \Delta x}{\ln(d_4 / d_3)} (T_{3,i} - T_{4,i}) \quad (6.43)$$

The effective thermal conductivity (k_{eff}) can be determined by using the correlation [115]:

$$k_{eff} = 0.386k_{34} \left(\frac{Pr_{34}}{0.861 + Pr_{34}} \right)^{1/4} (F_{cyl} Ra_{34})^{1/4} \quad (6.44)$$

Eq. (6.44) is valid for $0.7 \leq Pr_{34} \leq 6000$ and $10^2 \leq F_{cyl} Ra_{34} \leq 10^7$. Moreover, k_{34} and Pr_{34} are the thermal conductivity and Prandtl number of the gas in annular space at the average temperature ($T_{34,i}$), respectively. Ra_{34} is the Rayleigh number and can be obtained as follows:

$$Ra_{34} = \frac{g\beta(T_3 - T_4)L_c^3}{\nu_{34}^2} Pr_{34} \quad (6.45)$$

where ν_{34} is the kinematic viscosity of a gas in annular space, and β is the volume expansion coefficient at average temperature ($T_{34,i}$) which can be determined as:

$$\beta = \frac{1}{T_{34,i}} \quad (6.46)$$

F_{cyl} is the geometric factor for concentric cylinder and can be obtained as:

$$F_{cyl} = \frac{[\ln(d_4/d_3)]^4}{L_c^3 (d_3^{-3/5} + d_4^{-3/5})^5} \quad (6.47)$$

where L_c is the characteristic length and equals $(d_4 - d_3)/2$.

In this work, the receiver considers PTMx-36 (company designation), which is not vacuum based receiver.

6.3.3.2 Radiation Heat Transfer through the Annular Space

The radiation heat transfer between the selective surface of absorber and the inner surface of the glass envelope needs to be considered. They are assumed grey (independent of wavelength) and diffuse reflectors (independent of direction). The glass envelope is naturally opaque to the infrared radiation at wavelengths larger than approximately 2 μm . These assumptions are reasonable for the working conditions of the collectors [6]. The radiative flux is determined by the following equation for long concentrating cylinders [6]:

$$q_{rad,34} = \frac{\sigma \pi d_3 \Delta x (T_{3,i}^4 - T_{4,i}^4)}{\left[\frac{1}{\varepsilon_3} + \frac{(1 - \varepsilon_g) d_3}{\varepsilon_g d_4} \right]} \quad (6.48)$$

where ε_3 and ε_g are the emissivities of the outer surface of the absorber and the glass envelope.

In the present work, the surface emissivity is expressed as a second-order polynomial function of the absorber surface temperature. This functional form allows

more flexibility when studying the performances of PTC. In Table 4.2, these emissivity expressions are given for five different selective coatings.

In this work, the absorber of PTMx-36 was coated by Cermet coating. It is one of the most commonly used commercial coatings for CSP systems.

6.3.4 Heat Transfer through the Glass

The temperature distribution through glass wall of the envelope can be considered linear. In addition, the corresponding thermal conductivity is assumed constant. Therefore, the Fourier law can easily be applied for the conduction heat transfer which occurs from inner to outer surface of the glass envelope. It can be obtained from the following equation [115]:

$$q_{cond,45} = \frac{2\pi k_{45} \Delta x (T_{5,i} - T_{4,i})}{\ln\left(\frac{d_5}{d_4}\right)} \quad (6.49)$$

where k_{45} is thermal conductivity of glass envelope

In this work, In the collectors considered, a high heat resistant Pyrex glass is used to protect the absorber.

6.3.5 Heat Transfer between the Outer Surface of the Glass Envelope and the Surroundings

Heat transfer from outer surface of glass represents energy losses from HCE which include heat transfer by convection and radiation to the surrounding. Based on weather condition, either natural or forced convection heat transfer need to be considered. In this paper, both the natural and forced convection are considered in energy analysis. Radiation heat transfer is to be determined by considering the geometry, the temperature difference and the radiative properties. In addition to heat transfer between outer surface

of glass and sky, the energy analysis considers the effect of heat transfer between outer surface of glass and the reflector.

6.3.5.1 Convection Heat Transfer from the Outer Surface of the Glass Envelope

In heat transfer analysis, HCE is considered as a horizontal cylinder. The heat transfer coefficient is determined using the proper Nusselt number correlation. The heat flux can be calculated by applying Newton's law of cooling as follows [115]:

$$q_{conv,amb} = \pi d_5 h_a \Delta x (T_{5,i} - T_a) \quad (6.50)$$

where h_a is the heat transfer coefficient from outer surface of glass to ambient and is calculated by the Nusselt number as:

$$Nu_a = \frac{h_a d_5}{k_a} \quad (6.51)$$

The thermal conductivity of air (k_a) can be determined at the average temperature ($T_{5a,i}$) of outer surface temperature of glass ($T_{5,i}$) and the ambient temperature (T_a).

In the absence of wind, the heat transfer from the outer surface of glass considers natural convection mode. Then, Nusselt number can be estimated for a horizontal cylindrical geometry as [115]:

$$Nu_a = \left(0.6 + \frac{0.387 Ra_a^{1/6}}{\left[1 + (0.559 / Pr_a)^{9/16} \right]^{8/27}} \right)^2 \quad 10^5 < Ra_a < 10^{12} \quad (6.52)$$

Prandtl number of air (Pr_a) is determined at average temperature (T_{5a}), and Rayleigh number Ra_a can be calculated as:

$$Ra_a = \frac{g\beta(T_{5,i} - T_a)d_5^3}{\nu_a^2} Pr_a \quad (6.53)$$

where ν_a is the kinematic viscosity of air at average temperature ($T_{5a,i}$), and β is the volume expansion coefficient at average temperature ($T_{5a,i}$). It can be determined as:

$$\beta = \frac{1}{T_{5a,i}} \quad (6.54)$$

When there is wind, forced convection heat transfer occurs from the outer surface of glass envelope to ambient. Then, Nusselt number is estimated as [115]:

$$Nu_a = C Re_a^m Pr_a^n \quad (6.55)$$

Even though Eq. (6.55) is simple, the following equation by Churchill and Bernstein [115] is preferable to you because of its accuracy [115].

$$Nu_a = 0.3 + \frac{0.62 Re_a^{1/2} Pr_a^{1/3}}{\left[1 + (0.4 / Pr_a)^{2/3}\right]^{1/4}} \left[1 + \left(\frac{Re_a}{282000}\right)^{5/8}\right]^{4/5} \quad \text{For } Ra_a Pr_a > 0.2 \quad (6.56)$$

where Re_a , Pr_a are the Reynolds number and the Prandtl number of air at average temperature ($T_{5a,i}$).

6.3.5.2 Radiation Heat Transfer from the Outer Surface of the Glass Envelope

Radiation heat transfer occurs between the glass envelope and both of the sky and the reflector. The upper part of the glass surface faces the sky. The bottom part is only ringed by reflector, and the rest is surrounded by sky and reflector as shown in Figure 6.8. For this case, the radiation network approach is used [6]. The shape factor is also important to find unknowns in the network. The assumptions are considered to simplify complicated radiation transfer analysis problems. They neglect the end losses of PTC

since each loop of solar field is too long. Grey diffused isothermal and opaque of segment of glass envelope can be considered as well. In addition, the sky temperature is compensated for the different temperature to calculate radiation heat transfer and can be determined by using air ambient temperature from the following relation [110]:

$$T_{sky} = 0.05532T_a^{1.5} \quad (6.57)$$

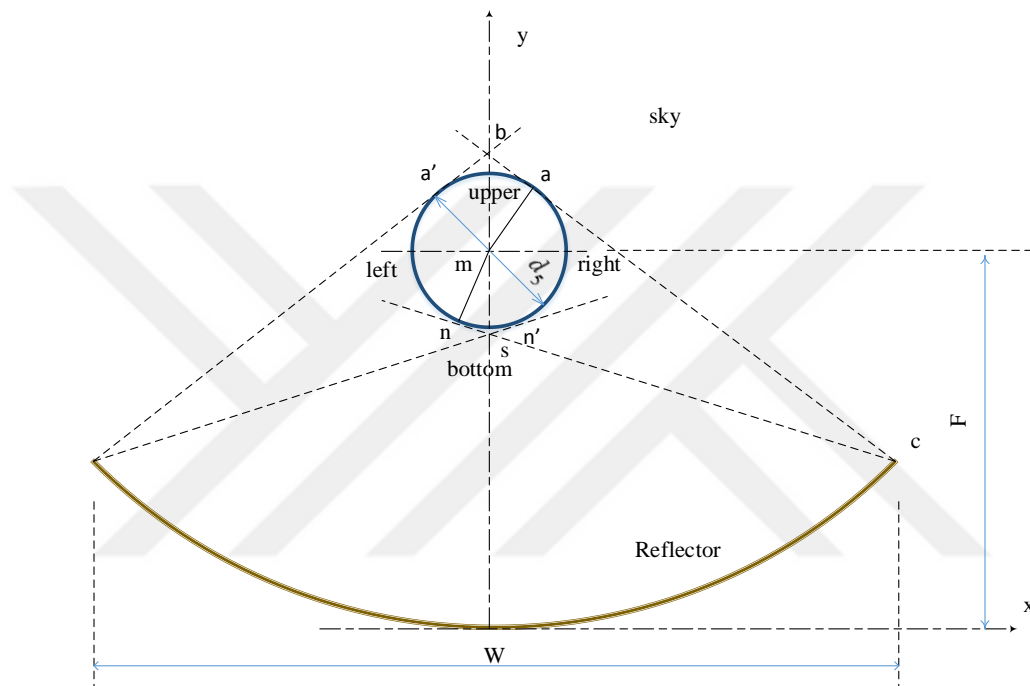


Figure 6.8 Geometry for PTC for calculation of shape factors and surface areas.

To specify the shape factor between surfaces, the cross-strings method and superposition and summation rules are utilized [6]. Figure 6.8 shows the symmetry between the right and left of HCE that interrelate the shape factors as $F_{right \rightarrow ref} = F_{left \rightarrow ref}$ and $F_{right \rightarrow sky} = F_{left \rightarrow sky}$. In addition, $F_{right \rightarrow right} = F_{left \rightarrow left} = 0$ because the convex surface cannot possibly receive radiation from itself. Moreover, the shape factor from reflector to itself is approximately $F_{ref \rightarrow ref} \approx 1 - 2/\pi$ [6]. $F_{bottom \rightarrow ref} = 1$ because the bottom part of glass only faces the reflector. All calculations of the surface areas per unit length (S) are

presented in Appendix A. The crossed-string method can illustrate the shape factor from the right of glass to reflector as follows [6]:

$$F_{right \rightarrow ref} = \frac{(S_{an'c'} + L_{n'c'}) - (S_{ac} - S_{n'c'})}{S_{an'}} \quad (6.58)$$

The superposition rule can be applied to determine the shape factor from reflector to the right side of glass as follows [122]:

$$F_{ref \rightarrow right} = \frac{S_{an'} F_{right \rightarrow ref}}{S_{ref}} \quad (6.59)$$

The summation rule is the third approach which can be used to specify the shape factor (F). The rule can result in calculating the shape factor from reflector to sky as:

$$F_{ref \rightarrow sky} = 1 - F_{ref \rightarrow ref} - 2F_{ref \rightarrow right} \quad (6.60)$$

Three parts of radiation heat transfer occur from the outer surface of glass envelope depending on the faced surface as:

1) The first part only exchanges from the upper surface of the glass to sky and can be determined as follows:

$$q_{rad, up \rightarrow sky} = \varepsilon_g \sigma S_{aa'} \Delta x (T_{5,i}^4 - T_{sky}^4) \quad (6.61)$$

where $S_{aa'}$ is the area per unit length of upper side of glass envelope.

2) Radiative heat flux from the bottom surface of the glass to the reflector is the second part and can be given as:

$$q_{rad,bottom \rightarrow ref} = \frac{\sigma \Delta x (T_{5,i}^4 - T_{ref}^4)}{\frac{1 - \epsilon_g}{S_{m'} \epsilon_g} + \frac{1}{S_{m'} F_{bottom \rightarrow ref}} + \frac{1 - \epsilon_{ref}}{S_{ref} \epsilon_{ref}}} \quad (6.62)$$

where $S_{m'}$ and S_{ref} are the area per unit length of the bottom side of glass envelope and reflector, respectively, as shown in Figure 6.8.

3) In the third part, the radiation heat transfer from the right and left surfaces of glass to sky and reflector can be determined by radiation network method as shown in Figure 6.9. Considering the symmetry between the right and left side of the glass surface, study of one side will be sufficient.

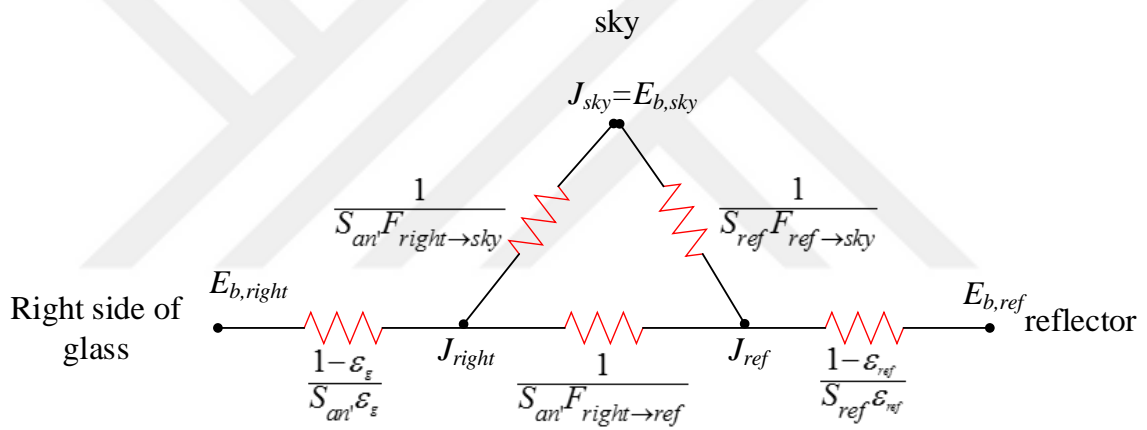


Figure 6.9 Radiation network between the right side of glass and both of sky and reflector.

Three equations are required to specify the third part of radiation heat transfer from glass. Two of them are applied to determine the unknown radiosities, and the third equation calculates the radiation heat transfer from the right and the left side of glass envelope as follows:

$$\frac{E_{b, right} - J_{right}}{\frac{1 - \epsilon_g}{S_{an'} \epsilon_g}} + \frac{E_{b, sky} - J_{right}}{\frac{1}{S_{an'} F_{right \rightarrow sky}}} + \frac{J_{ref} - J_{right}}{\frac{1}{S_{an'} F_{right \rightarrow ref}}} = 0 \quad (6.63)$$

$$\frac{E_{b,ref} - J_{ref}}{1 - \varepsilon_{ref}} + \frac{E_{b,sky} - J_{ref}}{1} + \frac{J_{right} - J_{ref}}{1} = 0 \quad (6.64)$$

$$\frac{S_{ref} \varepsilon_{ref}}{S_{ref} F_{ref \rightarrow sky}} \quad \frac{S_{an'} F_{right \rightarrow ref}}{S_{an'} F_{right \rightarrow ref}}$$

$$q_{rad, sides \rightarrow sky, ref} = 2S_{an'} \left[F_{right \rightarrow ref} (J_{right} - J_{ref}) + F_{right \rightarrow sky} (J_{right} - E_{b,sky}) \right] \quad (6.65)$$

where $S_{an'}$ is the area per unit length of the right side of glass envelope. Total radiation heat transfer from glass envelop to sky and reflector is given as follows:

$$q_{rad, amb} = q_{rad, up \rightarrow sky} + q_{rad, bottom \rightarrow ref} + q_{rad, sides \rightarrow sky, ref} \quad (6.66)$$

6.3.6 Thermal Efficiency

The thermal efficiency of the *PTC* is described as the ratio of useful energy gain by HTF to solar radiation input to the system. The useful energy gain represents all absorbed energy in HCE minus the energy losses to ambient by convection and radiation and can be determined as:

$$q_u = \left(\eta_o I_b A_a + \frac{\eta_o I_b A_a \alpha_g}{\tau_g \alpha_{abs}} + \frac{\eta_o I_b A_a \alpha_g \rho_{abs}}{\alpha_{abs}} + \frac{\eta_o I_b A_a \rho_{abs}^2 \alpha_g \rho_g}{\alpha_{abs}} + \eta_o I_b A_a \rho_{abs} \rho_g \right) - q_l \quad (6.67)$$

The outlet temperature from the segment as shown in Figure 6.7 can be calculated from sensible energy gain as:

$$T_{1,i+1} = T_{1,i-1} + \frac{q_u}{m c_{p_f}} \quad (6.68)$$

Then, the thermal efficiency can be obtained as:

$$\eta_{th} = \frac{q_u}{I_b A_a} \quad (6.69)$$

6.4 Validation of The Numerical Approach

Above, we have presented a comprehensive energy model for a PTC system. The model considers all heat transfer modes, including radiation and convection. A numerical solution was built by the EES. The results obtained by the current model were compared against two other studies, including: (1) the calculations reported by the company [108], and (2) the experimental data of Sandia National Laboratory [123] and the energy models proposed by NREL [64] and Zhen [124]. The calculations reported by Soltigua and the design conditions include the following: direct normal irradiance (DNI) of 900 W/m^2 , the inlet temperature of the Therminol-55 fluid at 142°C , and flow rate of $6 \text{ m}^3/\text{hr}$. The number of sunny hours and the monthly average temperature were measured by the State Meteorological Services in Turkey, and the data were gathered between January 1, 2010 and December 31, 2016. The first comparison includes two tests. In the first test (see results in a subsequent section), each loop of the proposed model produces 211 kW (Figure 6.18), while the design production is set to 200 kW. The second test (Figure 6.10) highlights the monthly useful energy production of the current model and the design [108].

In the same figure, the monthly average temperature of Aydin City is also compared with that from the State Meteorological Services in Turkey. The current model is in good agreement with the company design for most months. The inconsistent results can be attributed to metrological data sources and design conditions. The design conditions of the company model rely on the ambient temperature of 30°C . By contrast, the current model was built by using experimental data considering a range of temperatures, i.e., from heat transfer losses to ambient conditions. In addition, the current

model relies on the actual number of sunny hours. Therefore, the results of the current model are relatively more reliable because they are based on the current actual data.

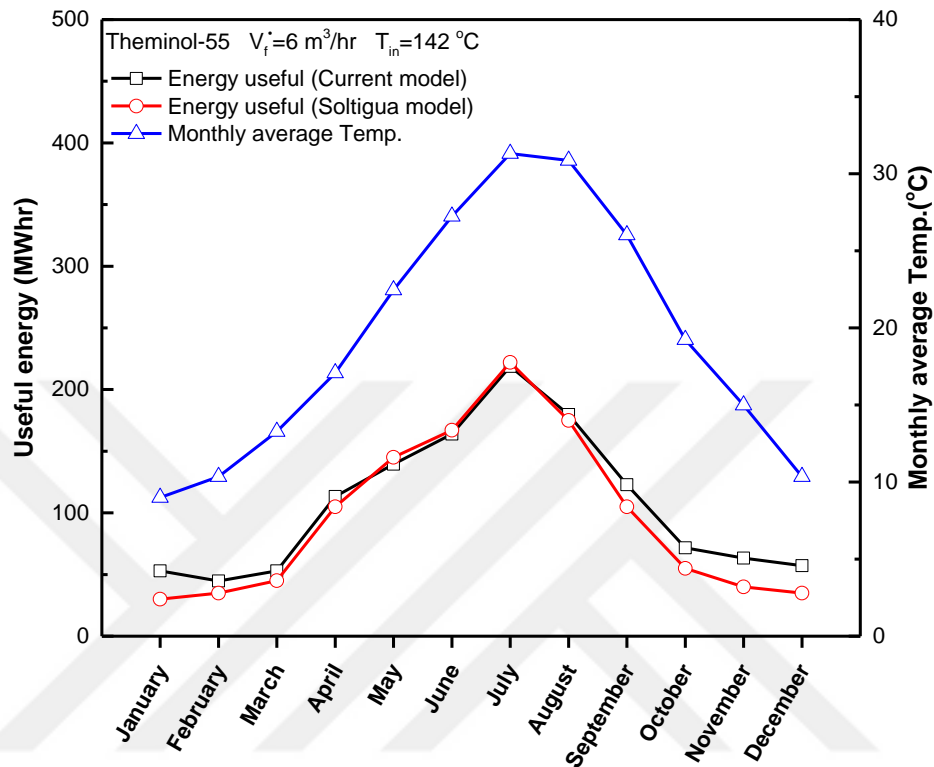


Figure 6.10 Useful energy of the PTC system and monthly average temperature for city of Aydin, Turkey throughout the year.

The second validation is made against the experimental and theoretical tests provided for the LS-2 solar collector as reported in [123]. This collector uses cermet selective coating and vacuum conditions, and considered in the four tests. Figure 6.11 presents the estimates of the bulk temperature range from 100°C to 400°C and the thermal efficiencies of the two models. As shown in Figure 6.11, the efficiency decreases markedly when the bulk temperature of the working fluid increases. This finding suggests that thermal efficiency is inversely proportional to HTF temperature, a phenomenon caused by the rise of energy losses to the ambient. The model developed in this work is in good agreement with these experimental tests.

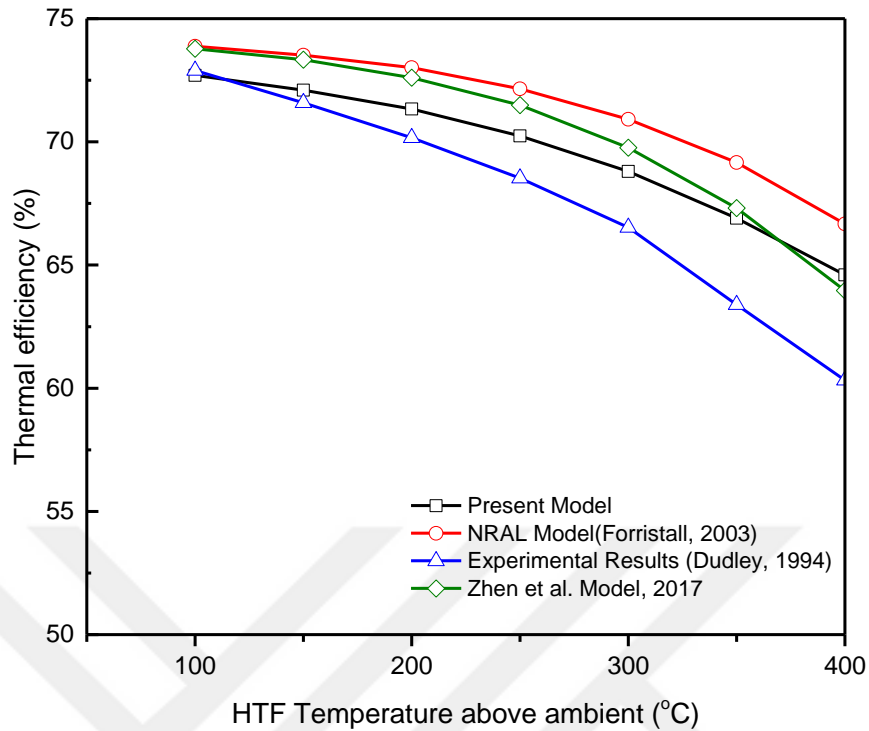


Figure 6.11 Comparison of thermal efficiency for present model and the other models.

6.5 Results and Discussions

A comprehensive energy analysis methodology is presented for PTC systems. A system available at the Campus of Aydin Adnan Menderes University is analyzed to determine its performance. The characteristics and operating limits of the PTMx-36 collector are listed in Table 6.1. The present model considers five gases in the annular space and five selective coatings. The useful energy gain and components of energy losses are obtained. The different effects of four common HTFs are also studied. The variations in useful energy gain, energy losses, and thermal efficiency can be compared under different operating and environmental conditions. The results are presented in the following subsections.

6.5.1 Gases Used in Annular Space

Two approaches are applied to reduce the convective heat transfer through the annular space: by using a vacuum condition or by filling the annular space with a low conductive gas instead of air. The information about the collectors is provided by the manufacturing company without the vacuum conditions in the annular space between the absorber and the envelope glass [108]. Thus, the convective heat transfer needs to be considered along with the thermal properties of gases and the temperature of surfaces. In addition to air, four gases are considered in our model. In Figure 6.12, shows the results for Argon gas, which reduces the convection losses in the annular space from 68 W/m at the beginning of the loop to more than 125 W/m at the end of the loop. By contrast, the losses increase from 184 W/m to 333 W/m when hydrogen gas is used. Hydrogen gas is not desirable to use, as it may also cause a permeation problem [64]. Therefore, convective heat loss can be minimized by filling the space with Argon gas.

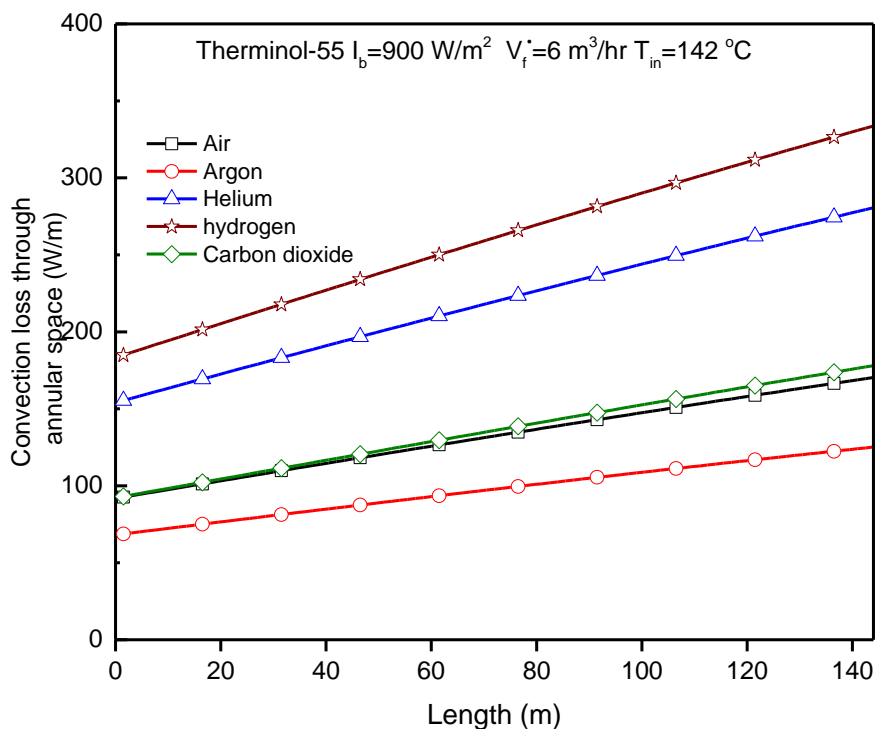


Figure 6.12 Convection losses through annular space for five gases along line of each loop.

6.5.2 Selective Coatings of Absorber Surface

Spectrally selective coatings should be analyzed when the thermal performance of a PTC is investigated. Table 4.2 presents the equations of emissivity as a function of the outer surface temperature of the absorber with five selective coatings. To assess these coatings, we should consider the thermal stability in the design conditions set by the manufacturing company [108]. Figure 6.13 presents the emissivity of the five coatings as a function of the temperature of the outer absorber surface.

Although the emissivity of all selective coatings increases along the line of the PTC, the emissivity of NREL-6A coating in this investigation is lower than those of the other coatings. The emissivity of NREL-6A slight increases from 0.025 to 0.03 at the end of the loop, whereas the emissivity of Black Chrome gradually increases from 0.13 to 0.16. The radiation losses from the outer surface of the absorber through the annular space are illustrated in Figure 6.14. The losses are strongly dependent on the optical properties and temperature of the outer absorber and the inner envelope glass surfaces. The radiation losses with the NREL-6A coating range from 8 W/m at the beginning of the loop to 20 W/m at the end of the loop, whereas the radiation losses with the Black Chrome coating range from 30 W/m to 95 W/m.

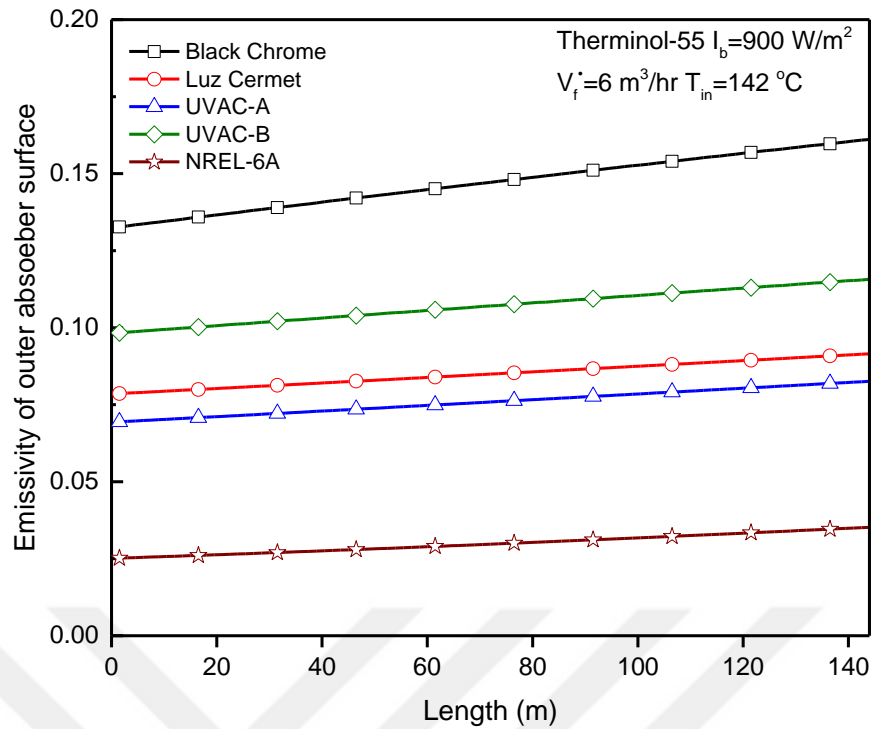


Figure 6.13 Emissivity of outer absorber surface for five selective coatings along line of each loop.

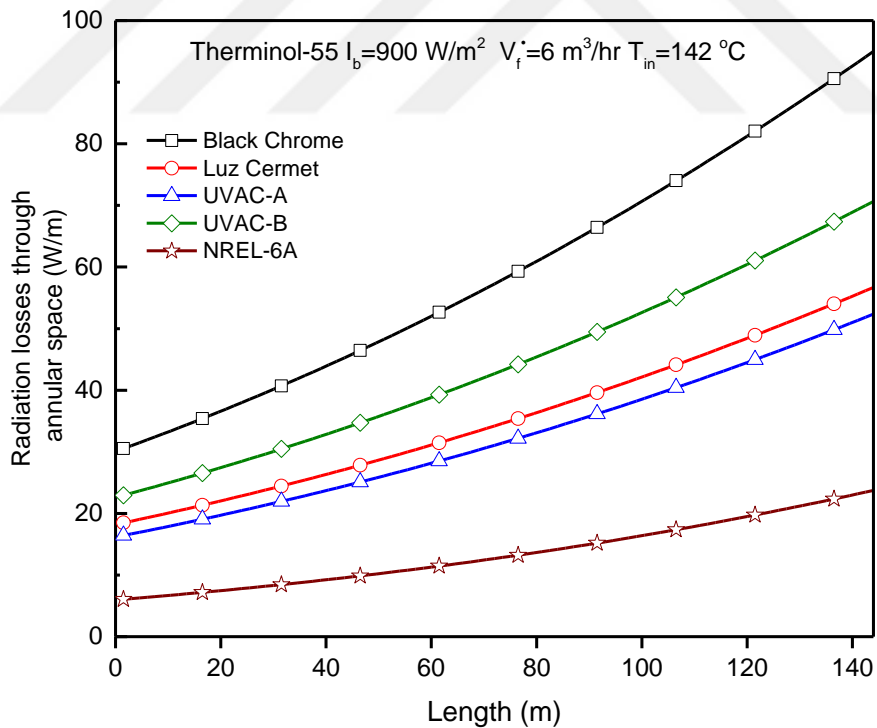


Figure 6.14 Radiation losses through annular space for five selective coatings along line of each loop.

The difference between the results of the outer surface temperature of the absorber is minimum (Figure 6.15). As such, the NREL-6A coating is the least dependent on the temperature among the compared coatings, although the emissivity is dependent on the outer surface temperature of the absorber. Therefore, the NREL-6A coating is the most thermally stable among all selective coatings considered. The results also indicate that the temperature of the inner surface of the glass envelope depends on the selective coating (Figure 6.16). The temperatures of the inner surface of the glass envelope are between 59.5°C and 76°C with NREL-6A coating, whereas the temperatures with Black Chrome coating are between 63°C to 84°C. Energy analysis should be performed to determine the suitable temperature and achieve the lowest energy loss with a given coating.

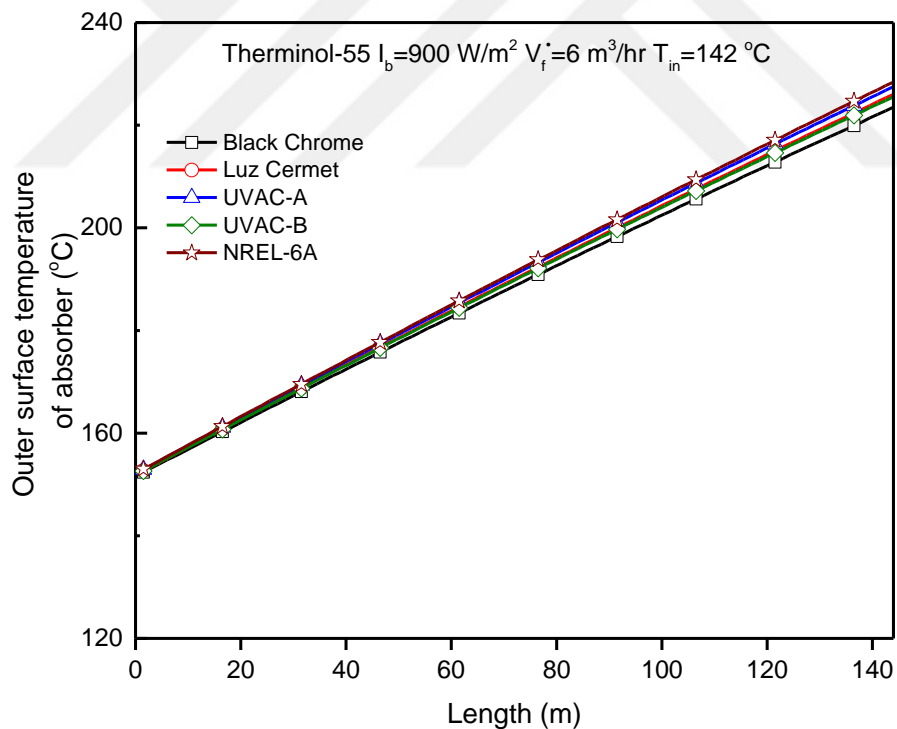


Figure 6.15 Outer surface temperature of absorber for five selective coatings along line of each loop.

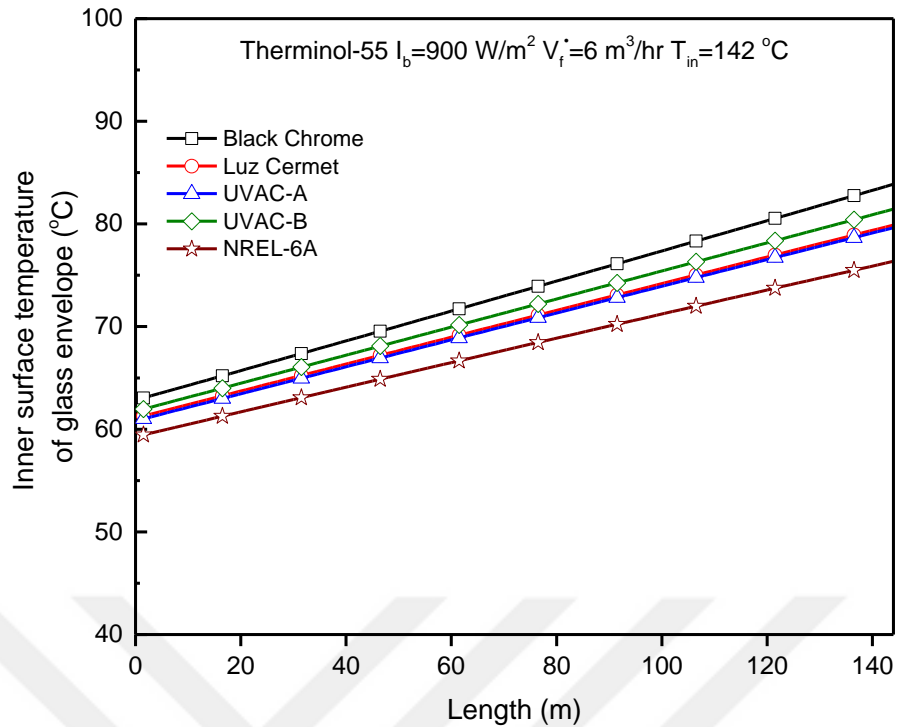


Figure 6.16 Inner surface temperature of glass envelope for five selective coatings along line of each loop.

6.5.3 Useful Energy

Useful energy is an important parameter to assess the performance of a PTC, as it shows the amount of energy transferred to the HTF. The modeling and design of PTC system should consider the input solar radiation beam and the energy gain by in HTF, as the outlet temperature of the HTF depends on the amount of solar energy absorbed.

The results obtained from the thermal analysis show the useful energy and the components of energy losses in Figure 6.17. The optical losses are unaffected by the length of the absorber because other factors, namely the intercept factor, incident angle modifier, collector geometric factor, and radiative properties play more dominant roles in optical losses. Furthermore, optical losses are unaffected by the temperature of the outer surface absorber. Figure 6.17 shows that the convection losses increase remarkably from 77 W/m to 141 W/m along the line of PTCs, whereas the radiation losses increase

from 113 W/m to 190 W/m. The losses caused by the radiative heat transfer are higher than those caused by convection because energy loss via radiation is proportional to the fourth power of the temperature of the outer absorber surface.

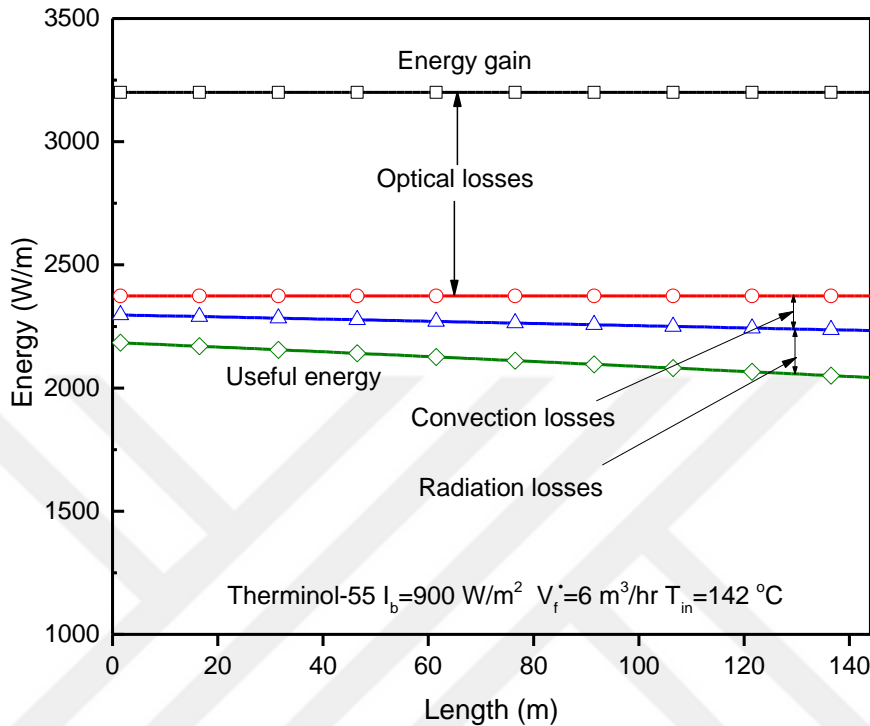


Figure 6.17 Useful energy and components of losses energy along line of each loop.

The energy gains are presented in Figure 6.18. The pie chart shows that more than two-thirds of the energy gain (67.4%) can be converted to useful energy, whereas less than a third of consumed energy (32.6%) corresponds to the lost energy. Two types of losses exist: optical and thermal losses. The optical losses account for approximately a quarter of the energy gain (25.3%). Thus, the main losses are optical losses. The thermal losses consist of the convection and radiation losses, thereby reaching 3.1% and 4.3%, respectively. These results indicate that the main losses are due to the optical parameters.

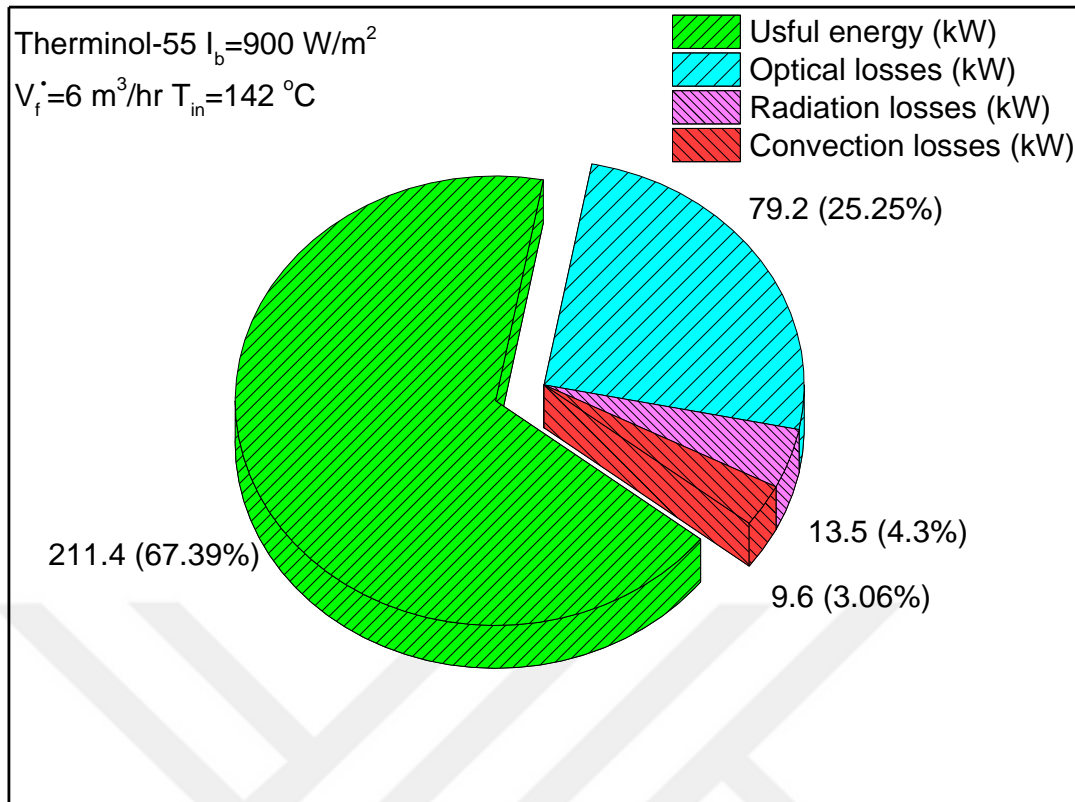


Figure 6.18 The amount and percentage of useful energy and components of losses energy along line of each loop.

6.5.4 Effect of Heat Transfer Fluids

Figure 6.19 shows the results obtained from the energy analysis of the PTC with four different HTFs. The two of the main characteristics of performance are thermal losses to ambient and pressure losses through the fluid flow in the pipe. No significant differences in the thermal losses (i.e., convection or radiation losses) are evident between the different types of HTF. Figure 6.19 illustrates the significant effect of the HTF on pressure losses. The effect of dynamic viscosity is the most dominant one. Consequently, Therminol-59 causes a minimum pressure loss of 62 kW at each loop, whereas Marlotherm-SH yields a maximum pressure loss of 77 kW.

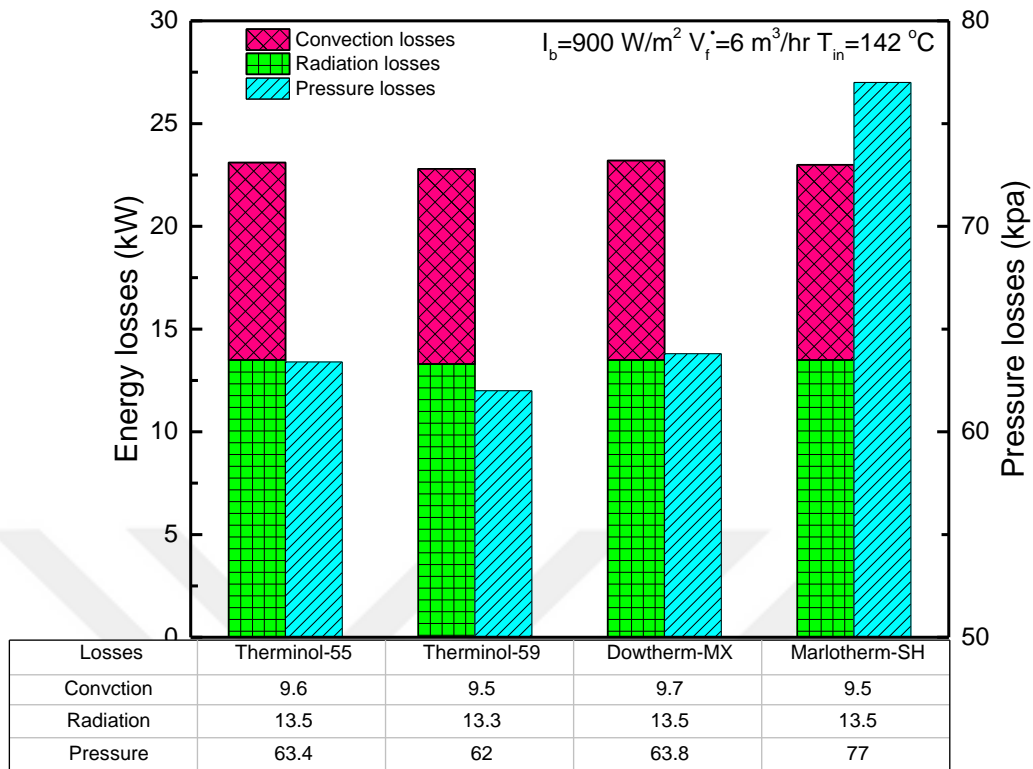


Figure 6.19 The energy losses (convection and radiation) and pressure losses for four type of heat transfer fluid.

The results of the thermal efficiency for the four HTFs are compared (Figure 6.20). The thermal properties of the HTF play a considerable role in the thermal efficiency of the PTC because of its effect on the heat transfer coefficient. When the length of the line increases, the thermal efficiency decreases because of the increase in temperature. Therefore, the losses increase. Therminol-55 has the best thermal efficiency ranging from 70.4% to 66%, whereas Marlotherm-SH demonstrates the lowest thermal efficiency varying from 70.3% to 65%. The range of operating temperature of each HTF is provided by the supplier.

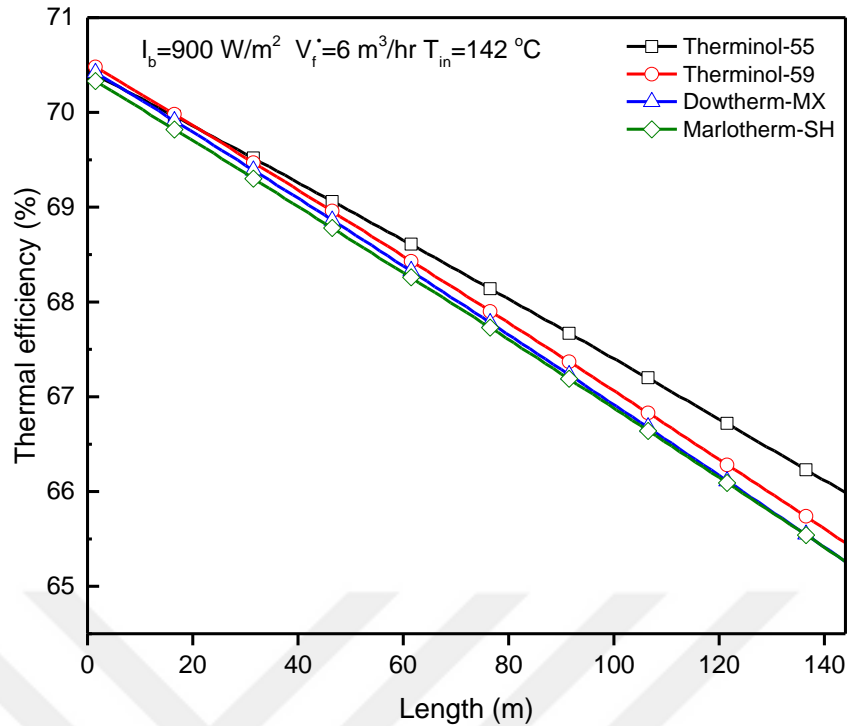


Figure 6.20 The thermal efficiency for four heat transfer fluids along line of each loop.

6.5.5 Effect of Operating Conditions

Various operating conditions are implemented to determine the parameter that is strongly dependent on these conditions. The inlet temperature and flow rate of HTF and wind velocity have remarkable effects on the thermal performance of the PTC. Figure 6.21 shows the results obtained when the HTF inlet temperature is changed. Increasing the inlet temperature can further increase the energy losses but cause a decrease in useful energy, and pressure loss.

Thus, increasing the inlet temperature reduces the thermal efficiency. For this reason, an appropriate inlet temperature should be selected to achieve the maximum thermal efficiency.

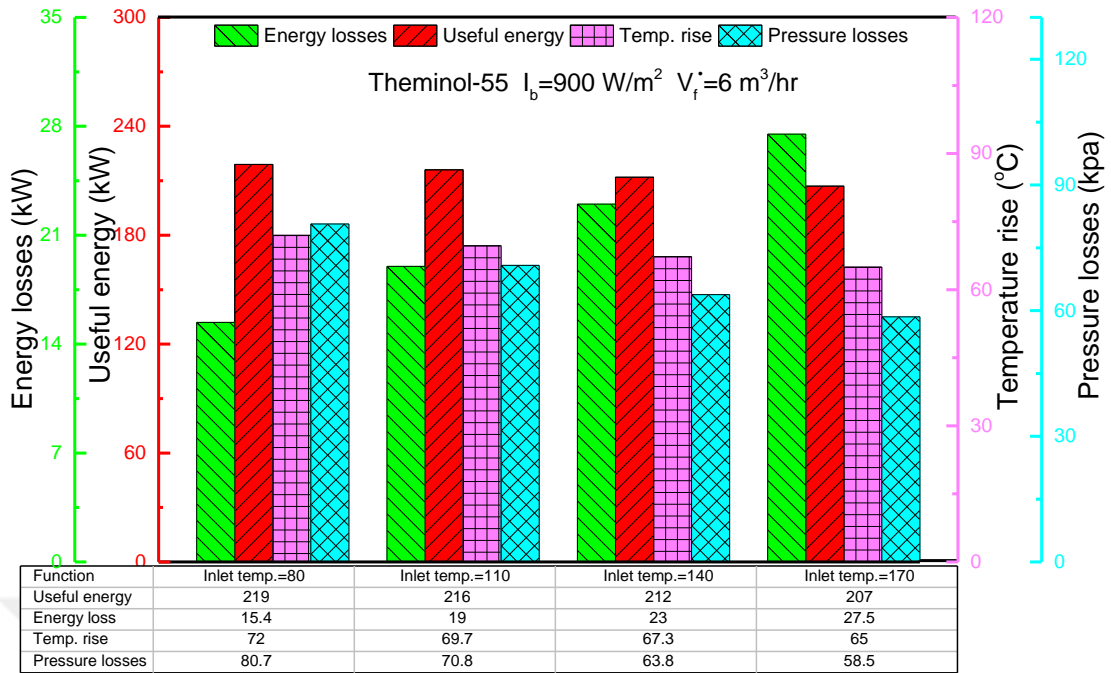


Figure 6.21 The useful energy, losses energy, increasing temperature and pressure losses for four inlet temperatures.

The impact of the HTF flow rate is shown in Figure 6.22, which is more significant than that of the inlet temperature. Increasing the flow rate can increase the useful energy and pressure losses but can reduce the temperature rise and the energy losses arising therefrom. On one hand, increasing the flow rate can improve the thermal efficiency. On the other hand, increasing the flow rate causes pressure losses. Therefore, the pump capacity should be increased. Consequently, the operating point should be selected at the optimal performance.

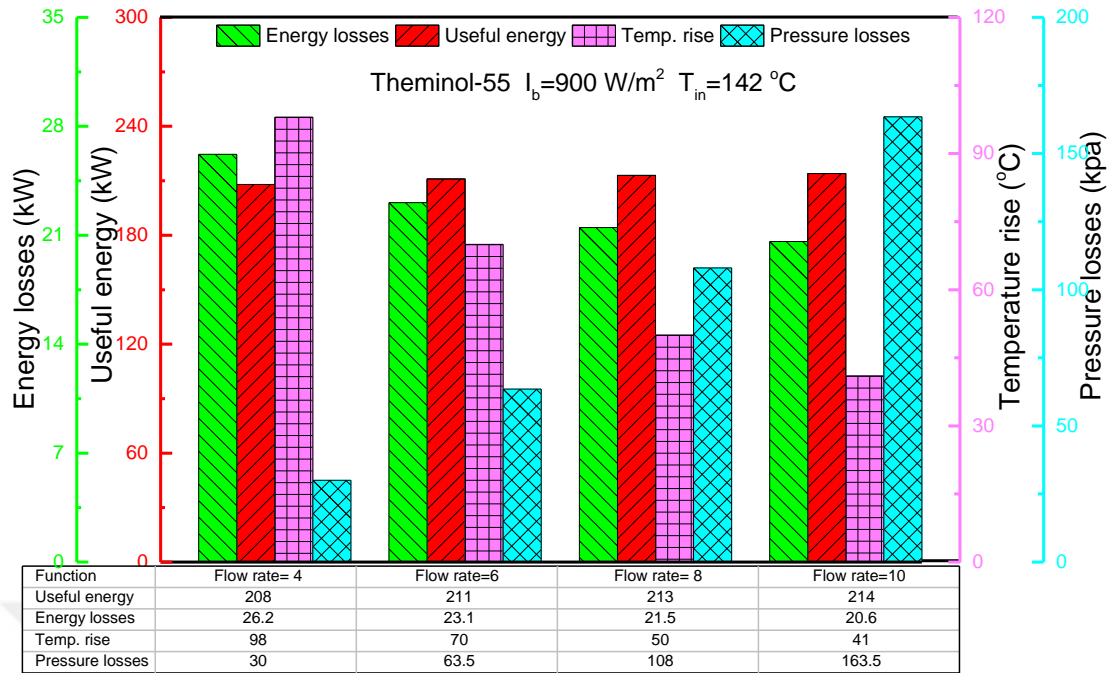


Figure 6.22 The useful energy, losses energy, increasing temperature and pressure losses for four flow rates.

As shown in Figure 6.23, the results suggest that the thermal efficiency is not strongly correlated with the third parameter of operating conditions, that is, wind velocity. The thermal efficiency changes approximately 1% when the wind velocity increases from 0 m/s to 2 m/s. As a consequence of the increase in velocity, the convective heat transfer coefficient increases. The outer surface temperature of the glass envelope approaches to ambient temperature. Therefore, wind velocity does not affect the thermal efficiency.

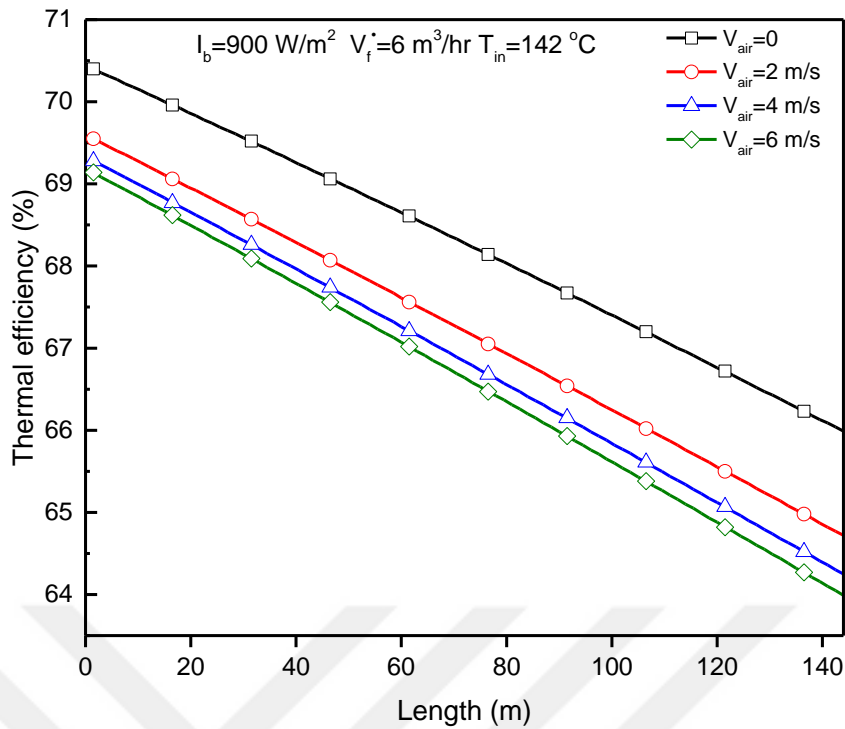


Figure 6.23 The thermal efficiency for four values of wind velocity along line of each loop.

6.6 Summary

This Chapter aims to assess the performance of an existing PTC system through a comprehensive energy analysis. A model was constructed which accounts for all optical components and the heat transfer modes. The optical properties of the selective coatings and the thermal properties of the HTFs are included in the model. The results obtained from the current model were compared with the calculations provided by the manufacturer of the PTC system and against the other results obtained from experimental tests and analytical models. The results indicate that the two-dimensional model is necessary to assess the performance of PTC systems.

Without vacuum conditions, the gas in the annular space can play a significant role on the convection losses. Also, the spectral emissivity of selective coatings is a significant parameter for the accurate calculation of the system efficiency by

demonstrating the radiation losses from the surface of the absorber. The optical losses are independent on the length of the loop and accounted for the largest percentage of all losses. The second largest percentage of losses due to the thermal processes which are attributed to the rising temperature of the outer surface of the absorber as the length of the loop increases. Therefore, the thermal efficiency of the PTC is reduced along the line of the loop. In addition, the effect of operating conditions on the performance of a PTC system is significant. Among different parameters, the effects of inlet temperature and wind velocity are directly proportional to the energy losses, whereas the flow rate is inversely proportional to the same.

CHAPTER VII

RADIATIVE EXERGY PERFORMANCE ANALYSES OF A PTC SYSTEM

7.1 Exergy Model

A complementary approach to study the performance of PTC is by exergy analysis, which allows designers to decrease the exergy consumption during processes to enhance the thermal performance of the PTC. The exergy balance can be expressed as [17]:

$$\text{Exergy input} - \text{Exergy output} - \text{Exergy consumption} = \text{Exergy accumulation} \quad (7.1)$$

The surface temperatures of the inlet and outlet for the segment of the receiver can be considered constant. Therefore, the thermodynamic properties are not changed with respect to time. For this reason, the analysis is under a steady state. The exergy accumulation is neglected, and the exergy balance for PTC becomes:

$$\text{Exergy input} - \text{Exergy output} - \text{Exergy consumption} = 0 \quad (7.2)$$

The last term in Eq. (7.2) presents the exergy losses and exergy destructions. Exergy consumption should be decreased for two reasons. First, they are unwanted and second, improving the performance of the solar collector is crucial. The exergy destruction is produced by the irreversibility of thermal processes while the exergy losses describe the heat transfer losses to the surrounding and having an optical error. The exergy analysis for PTC is shown in Figure 7.1. Exergy analysis is based on energy analysis which presented in Chapter six.

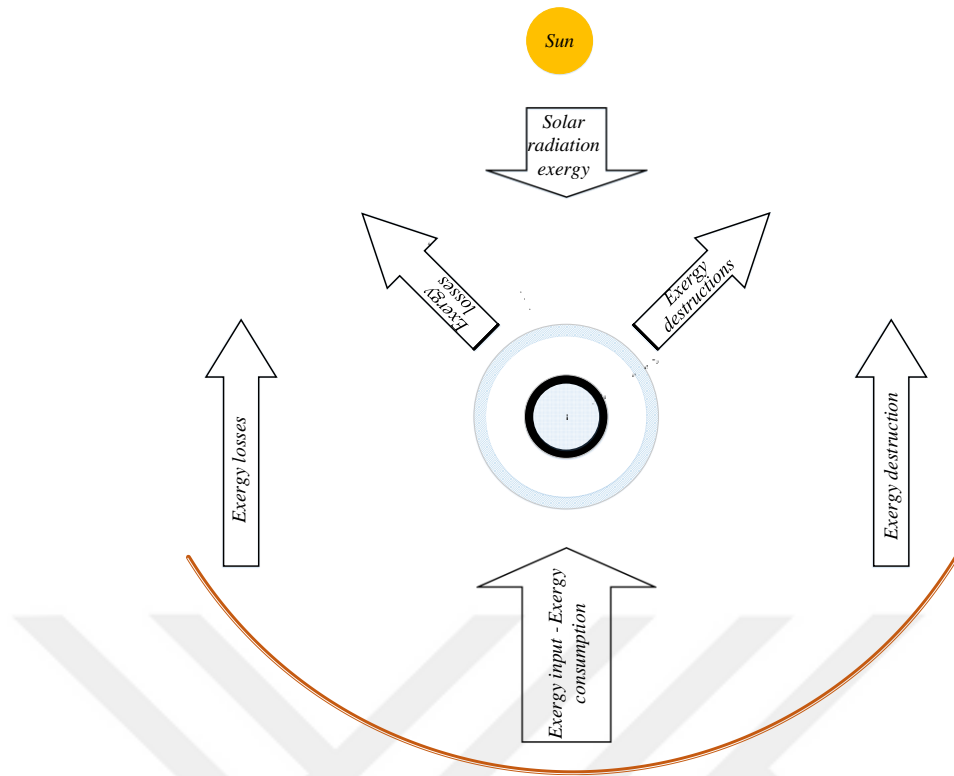


Figure 7.1 Exergy balance for receiver subsystem.

The maximum efficiency associated with radiation heat transfer is consistently less than the maximum efficiency related to conduction and convection heat transfer. That is, the losses caused by radiation heat transfer are higher than those produced by other modes of heat transfer because energy transfer via radiation is proportional to the fourth power of the temperature. For this reason, we use two formulas to obtain the exergy of heat transfer modes, as described in Chapter two, Eq. (3.35) used to obtain the exergy from converting radiation heat transfer to work. The second approach uses the Carnot efficiency expression (η_{II}) for calculating the exergy only due to conduction and convection heat transfer modes; the expression is [12]:

$$\eta_{II} = 1 - \frac{T_a}{T} \quad (7.3)$$

The form of specific exergy (ex) in open system with negligible potential energy can be determined as [114]:

$$ex = \left((h - h_a) - T_a (s - s_a) + \frac{V^2}{2} \right) \quad (7.4)$$

For an incompressible matter, the enthalpy change and entropy change from initial to the final state are obtained as [88]:

$$h - h_a = \int dh = \int c_p dT = c_p (T - T_a) \quad (7.5)$$

$$s - s_a = \int ds = \int c_p \frac{dT}{T} = c_p \ln \frac{T}{T_a} \quad (7.6)$$

7.1.1 Exergy Balance for Reflector Subsystem

The captured energy by reflector is obtained as:

$$q_{in} = I_b A_a \quad (7.7)$$

The exergy receives by the reflector ($Ex_{in,ref}$) includes only solar radiation, as expressed as follows [125]:

$$Ex_{in,ref} = q_{in} \psi = I_b A_a \left(1 - \frac{4}{3} \frac{(T_a T_s^3 - T_a^4)}{(T_s^4 - T_a^4)} \right) \quad (7.8)$$

The exergy output from the reflector toward the receiver ($Ex_{out,ref}$) is only one part related to solar radiation, as expressed as follows:

$$Ex_{out,ref} = q_{abs} \psi = I_b A_a \eta_o \left(1 - \frac{4}{3} \frac{(T_a T_{3,i}^3 - T_a^4)}{(T_{3,i}^4 - T_a^4)} \right) \quad (7.9)$$

The exergy consumption ($Ex_{cons,ref}$) due to radiation transfer from the Sun to selective surface and heat losses, which consist two components (convection and radiation) is expressed as [126]:

$$Ex_{cons,ref} = Ex_{d,ht,ref} + Ex_{l,conv,ref} + Ex_{l,rad,ref} \quad (7.10)$$

The first part of exergy consumption is the exergy destruction ($Ex_{d,ht,ref}$), which has been produced as a result to solar radiation transfer from the source (Sun) to sink (selective surface), which can be expressed as:

$$Ex_{d,ht,ref} = \frac{4}{3} I_b A_a \eta_o \left(\frac{(T_a T_{3,i}^3 - T_a^4)}{(T_{3,i}^4 - T_a^4)} - \frac{(T_a T_s^3 - T_a^4)}{(T_s^4 - T_a^4)} \right) \quad (7.11)$$

The heat losses from reflector to ambient and sky by convection and radiation, respectively. They can be computed by:

$$q_{conv,ref} = 2A_{ref} h (T_{ref} - T_o) \quad (7.12)$$

$$q_{rad,ref} = \varepsilon_{ref} \sigma A_{ref} (T_{ref}^4 - T_{sky}^4) \quad (7.13)$$

where A_{ref} is the surface area of reflector, h is the convection heat transfer coefficient (typically is 10 W/m² K) [127]. T_{ref} is the temperature of reflector. ε_{ref} is the mirror emissivity(is 0.85) [110]. Exergy losses due to convection ($Ex_{l,conv,ref}$) and radiation ($Ex_{l,rad,ref}$) heat transfer modes from the reflector to ambient and sky, respectively, can be given:

$$Ex_{l,conv,ref} = q_{conv,ref} \eta_{II} = 2A_{ref} h (T_{ref} - T_a) \left(1 - \frac{T_a}{T_{ref}} \right) \quad (7.14)$$

$$Ex_{l,rad,ref} = q_{rad,ref} \psi = \varepsilon_{ref} \sigma A_{ref} (T_{ref}^4 - T_{sky}^4) \left(1 - \frac{4}{3} \frac{(T_a T_{ref}^3 - T_a^4)}{(T_{ref}^4 - T_a^4)} \right) \quad (7.15)$$

7.1.2 Exergy Balance for Receiver Subsystem

Exergy analysis of receiver can be applied, as shown in Figure 7.2. The irreversibility processes and energy losses can be defined. Moreover, the exergy efficiency is derived. The exergy input to the receiver ($Ex_{in,rec}$) includes two parts. The first part is the exergy of matter ($Ex_{in,f,rec}$), which is due to heat transfer by the incoming fluid to the receiver. The second part of the solar radiation exergy ($Ex_{in,rad,rec}$), which is absorbed by selective coating, can be calculated as:

$$Ex_{in,rec} = m \left((h_{in,i} - h_a) - T_a (s_{in,i} - s_a) \right) \left(+ \frac{V_{in}^2}{2} \right) + I_b A_a \eta_o \left(1 - \frac{4}{3} \frac{(T_a T_{3,i}^3 - T_a^4)}{(T_{3,i}^4 - T_a^4)} \right) \quad (7.16)$$

For incompressible substances, Eqs. (7.5) and (7.6) are substituted into (7.16), which can be rewritten as:

$$Ex_{in,rec} = m \left(\left(c_{p,i} \left((T_{in,i} - T_a) - T_a \ln \frac{T_{in,i}}{T_a} \right) \right) + \frac{V_{in}^2}{2} \right) + I_b A_a \eta_o \left(1 - \frac{4}{3} \frac{(T_a T_{3,i}^3 - T_a^4)}{(T_{3,i}^4 - T_a^4)} \right) \quad (7.17)$$

The exergy output from the receiver ($Ex_{out,rec}$) is one part related to exit HTF from the solar receiver. The total exergy can be determined as:

$$Ex_{out,rec} = m \left(\left(c_{p,i} \left((T_{out,i} - T_a) - T_a \ln \frac{T_{out,i}}{T_a} \right) \right) + \frac{V_{out}^2}{2} \right) \quad (7.18)$$

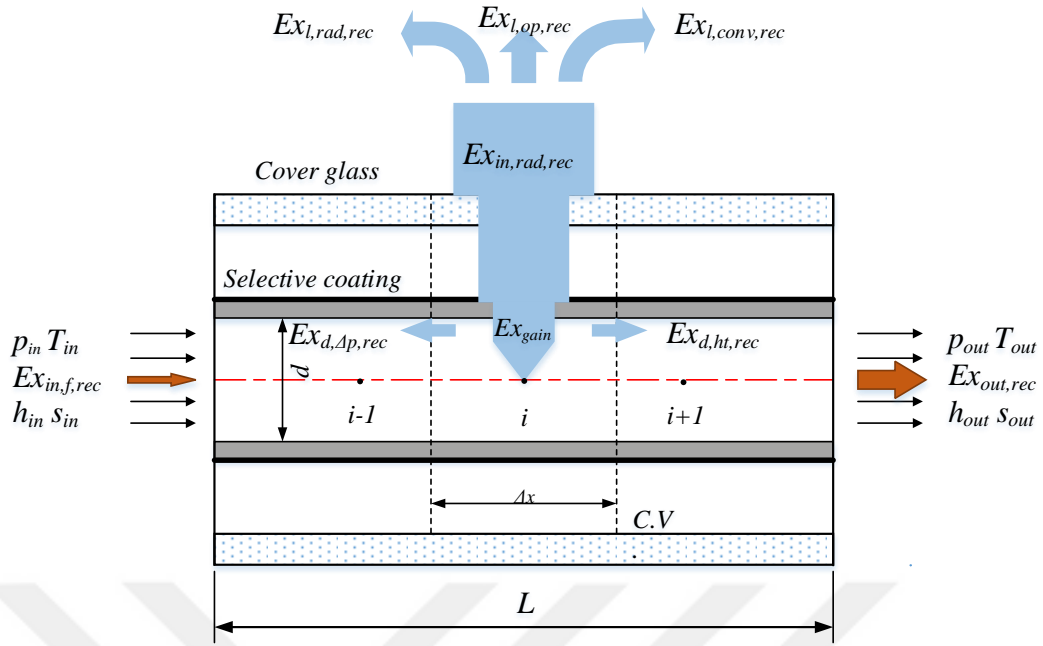


Figure 7.2 Schematic of exergy balance for the receiver.

In the receiver of PTC, the exergy consumption ($Ex_{cons,rec}$) is expressed by the exergy destruction ($Ex_{d,rec}$) and exergy losses ($Ex_{l,rec}$). The exergy consumption is as follows [83]:

$$Ex_{cons,rec} = Ex_{d,rec} + Ex_{l,rec} \quad (7.19)$$

The exergy is destroyed because of the heat transfer of solar radiation from the Sun to the selective coating surface and the transfer of heat from the surface of the pipe to the fluid. The friction of viscous fluid can have a considerable effect for destroying exergy, as expressed as follows [128]:

$$Ex_{d,rec} = Ex_{d,ht,rec} + Ex_{d,\Delta p,rec} \quad (7.20)$$

The mechanisms that generate entropy through the receiver results from irreversibility. The differential expression of the second principle of thermodynamics in

an open system includes the specific enthalpy and energy flow. This expression is also known as the Gibbs relation, which can be expressed as follows as [88]:

$$Tds = dh - vdp \quad (7.21)$$

The specific exergy (ex) as a function of temperature and pressure can be considered to derive the total differential of change in specific exergy, which can be written as follows:

$$dex = \left(\frac{\partial ex}{\partial T} \right)_p dT + \left(\frac{\partial ex}{\partial p} \right)_T dp \quad (7.22)$$

The partial derivative of the temperature and pressure of Eqs (7.5), (7.6) and (7.21) at a constant velocity and incompressible fluid flow, can be applied with respect to T and p , respectively as shown as follows:

$$\left(\frac{\partial ex}{\partial T} \right)_p = \left(\frac{\partial h}{\partial T} \right)_p - T_a \left(\frac{\partial s}{\partial T} \right)_p = c_p - T_a \frac{c_p}{T} = c_p \left(1 - \frac{T_a}{T} \right) \quad (7.23)$$

$$\left(\frac{\partial ex}{\partial p} \right)_T = \left(\frac{\partial h}{\partial p} \right)_T - T_a \left(\frac{\partial s}{\partial p} \right)_T = \left(\frac{\partial h}{\partial p} \right)_T - T_a \left(\frac{1}{T} \left(\frac{\partial h}{\partial p} \right) - \frac{v}{T} \right)_T = v \quad (7.24)$$

By substituting Eqs. (7.23) and (7.24) into Eq. (7.22). Then, the change in specific exergy is obtained as:

$$dex = c_p \left(1 - \frac{T_a}{T} \right) dT + vdp \quad (7.25)$$

As shown in Figure 7.2, the exergy balance for the receiver in a control volume at steady state can be expressed as:

$$\delta Ex_{in,rec} - \delta Ex_{out,rec} - \delta Ex_{cons,rec} = 0 \quad (7.26)$$

As mentioned earlier in Eq. (7.16), the exergy input to receiver ($Ex_{in,rec}$) involves two components. That is, the incoming fluid to the receiver has exergy of matter, and the exergy of the solar radiation is absorbed by selective coating and then, transferred to fluid as useful heat. The change of exergy of fluid between input ($\delta Ex_{in,rec}$) and output ($\delta Ex_{out,rec}$) of the receiver can be computed by multiple changes in specific exergy by a mass flow rate in Eq. (7.25). Moreover, the significant heat gain through the wall of the pipe can lead to increase in the fluid temperature. Consequently, when the temperature increases according to Newton's law of cooling, the change of temperature will be nonlinear. Therefore, the arithmetic means cannot describe the actual mean temperature, whereas logarithmic mean temperature can accurately lead to mean temperature [129]. Then, Eq. (7.26) can be rewritten as:

$$m \left(c_p \left(\frac{T_a}{T} - 1 \right) dT - v dp \right) - \delta Ex_{cons,rec} + m c_p dT \left(1 - \frac{T_a}{T_3} \right) = 0 \quad (7.27)$$

The logarithmic mean temperature can be used to simplify Eq. (7.27). Hence, the exergy destruction ($Ex_{d,rec}$) can be calculated as:

$$Ex_{cons,rec} = m T_a c_p \left[\ln \left(T_{out,i} / T_{in,i} \right) - \frac{(T_{out,i} - T_{in,i})}{T_{3,i}} \right] - m v \Delta p + Ex_{l,rec} \quad (7.28)$$

From the right side of Eq. (7.28), the first part presents to exergy destructions due to heat transfer by gradient of temperatures through radial axis of a receiver, whereas the exergy destructions caused by viscous fluid computes by the second part. The exergy losses ($Ex_{l,rec}$) describe the optical error and the heat transfer losses to the ambient and sky. The total exergy losses from the receiver can be computed as follows:

$$Ex_{l,rec} = Ex_{l,op,rec} + Ex_{l,conv,rec} + Ex_{l,rad,rec} \quad (7.29)$$

The first part is exergy losses due to optical error ($Ex_{l,op,rec}$), which are produced by several factors included in optical efficiency and obtained as:

$$Ex_{l,op,rec} = I_b A_a (1 - \eta_o) \left(1 - \frac{4 (T_a T_{3,i}^3 - T_a^4)}{3 (T_{3,i}^4 - T_a^4)} \right) \quad (7.30)$$

The losses come from the receiver to the ambient and sky by convection and radiation, which is presented in Chapter six. The second and third parts on the right side of Eq. (7.29) are exergy losses that result from heat losses of an outer cover glass of the receiver to the ambient and sky by convection and radiation heat transfer modes, which can be expressed as follows:

$$Ex_{l,conv,rec} = q_{conv,amb} \eta_{II} = q_{conv,amb} \left(1 - \frac{T_a}{T_{5,i}} \right) \quad (7.31)$$

$$Ex_{l,rad,rec} = q_{rad,amb} \psi = q_{rad,amb} \left(1 - \frac{4 (T_a T_{5,i}^3 - T_a^4)}{3 (T_{5,i}^4 - T_a^4)} \right) \quad (7.32)$$

Then, Eq. (7.19) can be rewritten with all components of exergy consumption as:

$$Ex_{cons,rec} = Ex_{d,ht,rec} + Ex_{d,\Delta P,rec} + Ex_{l,op,rec} + Ex_{l,conv,rec} + Ex_{l,rad,rec} \quad (7.33)$$

Exergy gain accumulates exergy by HTF through the receiver that absorbs solar radiation by selective coating.

7.1.3 Exergy Balance for PTC

The exergy input ($Ex_{in,ptc}$) to PTC comprises solar radiation. Exergy input is the same term of exergy received by the reflector and is expressed as:

$$Ex_{in,ptc} = Ex_{in,ref} = I_b A_a \left(1 - \frac{4}{3} \frac{(T_a T_s^3 - T_a^4)}{(T_s^4 - T_a^4)} \right) \quad (7.34)$$

The exergy gain to PTC includes the exergy difference between output and input exergies for HTF. Exergy consumption ($Ex_{cons,ptc}$) includes all exergy destructions and exergy losses from the reflector and receiver, Eqs. (7.10) and (7.20) demonstrate that total exergy consumption of the PTC. Thus, the following equation is obtained:

$$Ex_{cons,ptc} = Ex_{d,ptc} + Ex_{l,ptc} \quad (7.35)$$

The exergy efficiency of the PTC described the ratio of exergy output as exergy gain by HTF to solar radiation exergy input to the reflector. However, the previous definition of exergy efficiency cannot exhibit the destruction and loss of exergies, which are important in characterizing the reasons and positions of these consumptions. Hence, the exergy efficiency can be considered as a function of exergy consumption components. Then, the exergy efficiency of PTC can be obtained as:

$$\eta_{ex,ptc} = 1 - \frac{Ex_{cons,ptc}}{Ex_{in,ptc}} \quad (7.36)$$

A dimensionless fraction exergy term is used to define how much the ratio of each parameter of exergy consumption is to incoming radiation exergy ($Ex_{in,ptc}$). Then, the exergy efficiency can be rewritten as:

$$\eta_{ex,ptc} = 1 - Ex_{cons,ptc}^* \quad (7.37)$$

where $Ex_{cons,ptc}^*$ is a dimensionless fraction of exergy consumption ($Ex_{cons,ptc}^* = Ex_{cons,ptc}/Ex_{in,ptc}$). In the same way, all components of exergy consumption in Table 7.1.

Table 7.1 Dimensionless exergy fractions of exergy consumption for PTC.

Dimensionless exergy fractions	Functions	Equations
Exergy destructions of solar radiation transfer from Sun	$Ex_{d,ht,ref}^*$	$\frac{Ex_{d,ht,ref}}{Ex_{in,ptc}}$
Exergy losses due to convection losses from reflector	$Ex_{l,conv,ref}^*$	$\frac{Ex_{l,conv,ref}}{Ex_{in,ptc}}$
Exergy losses due to radiation losses from reflector	$Ex_{l,rad,ref}^*$	$\frac{Ex_{l,rad,ref}}{Ex_{in,ptc}}$
Exergy destructions due to heat transfer by gradient temperatures through receiver	$Ex_{d,ht,rec}^*$	$\frac{Ex_{d,ht,rec}}{Ex_{in,ptc}}$
Exergy destructions caused by viscous fluid through receiver	$Ex_{d,\Delta P,rec}^*$	$\frac{Ex_{d,\Delta P,rec}}{Ex_{in,ptc}}$
Exergy losses due to optical error	$Ex_{l,op,rec}^*$	$\frac{Ex_{l,op,rec}}{Ex_{in,ptc}}$
Exergy losses due to convection losses from receiver	$Ex_{l,conv,rec}^*$	$\frac{Ex_{l,conv,rec}}{Ex_{in,ptc}}$
Exergy losses due to radiation losses from receiver	$Ex_{l,rad,rec}^*$	$\frac{Ex_{l,rad,rec}}{Ex_{in,ptc}}$

7.2 Results and Discussion

A detailed exergy analysis is presented the first time for an actual PTC system based on radiative exergy concept. In this approach, PTMx-36 collector is used. Five gases in annular space, five selective coatings of the absorber are investigated. To assess the performance, dimensionless fractions of exergy consumption are used. The comparative exergy work for four working fluids is outlined. Various operating conditions are also studied. The results obtained from this approach are presented in the following subsections.

7.2.1 Gases Used in Annular Space

Without considering vacuum conditions in the analysis, Air, Argon, Helium, Carbon dioxide and Hydrogen in annular space are used. Figures 7.3 to 7.6 show the key parameters of exergy, including, exergy losses, destructions, consumption, and efficiency, respectively, for a PTC system, after filling annular space with five different gases. The exergy losses for these gases are presented in Figure 7.3. In general, the most likely cause of increasing exergy losses along the line of each loop is the rising temperature of the absorber surface. The minimum exergy losses are obtained by Argon from 239 W/m at the beginning of the loop to 343 W/m at the end. By contrast, Hydrogen increases the exergy losses from 264 W/m to 391 W/m. Figure 7.4 presents the exergy destructions along the line for each loop for five gases. For the examined gases, one reason why exergy destructions have increased due to the inverse proportionality between the temperature of the absorber surface (sink temperature) and exergy destructions.

The differences in exergy destructions of five gases are at a minimum. Although the exergy losses increase along the line of the pipe, the exergy consumption decreases (Figure 7.5) because the exergy destruction is higher than the exergy losses. For Argon gas, at the beginning of the line of the loop, the exergy losses are 239 W/m, and the exergy destruction is 2420 W/m as shown in Figures 7.3 and 7.4, respectively. This means that the length of the lines is an independent parameter. The lowest exergy consumption is achieved by Argon whereas the highest can be found by using Hydrogen gas as seen in Figure 7.5. The exergy efficiencies are illustrated in Figure 7.6. The efficiencies are not significant considering the exergy losses and are strongly dependent on exergy destructions. The exergy efficiency for Argon ranges from 33.1% at the

beginning of the loop to 37.5% at the end of the loop, whereas the exergy efficiency with Hydrogen ranges from 32.6% to 36%.

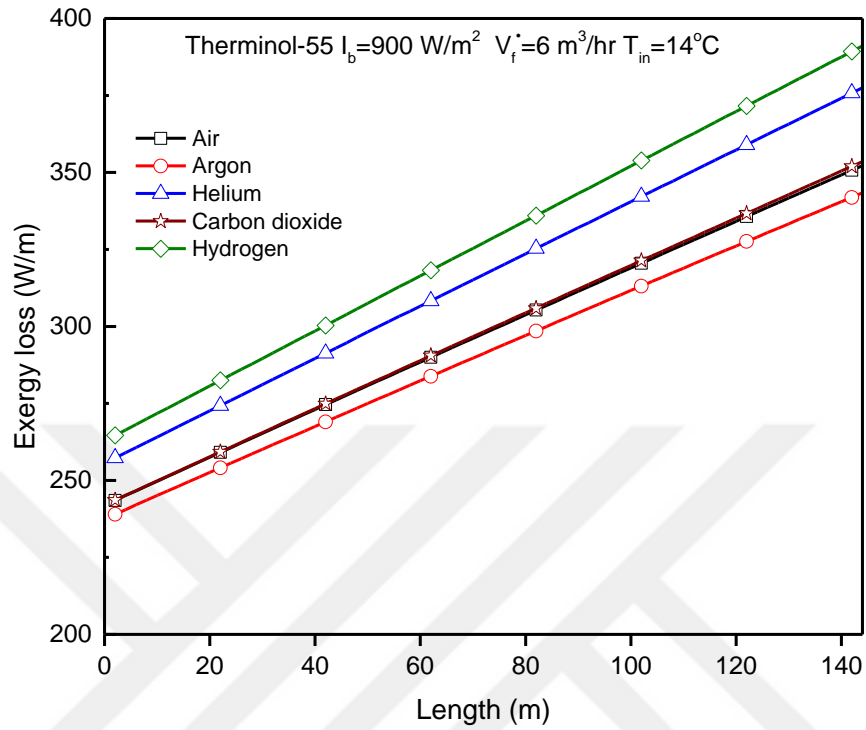


Figure 7.3 Exergy losses through annular space for five gases along the line of each loop.

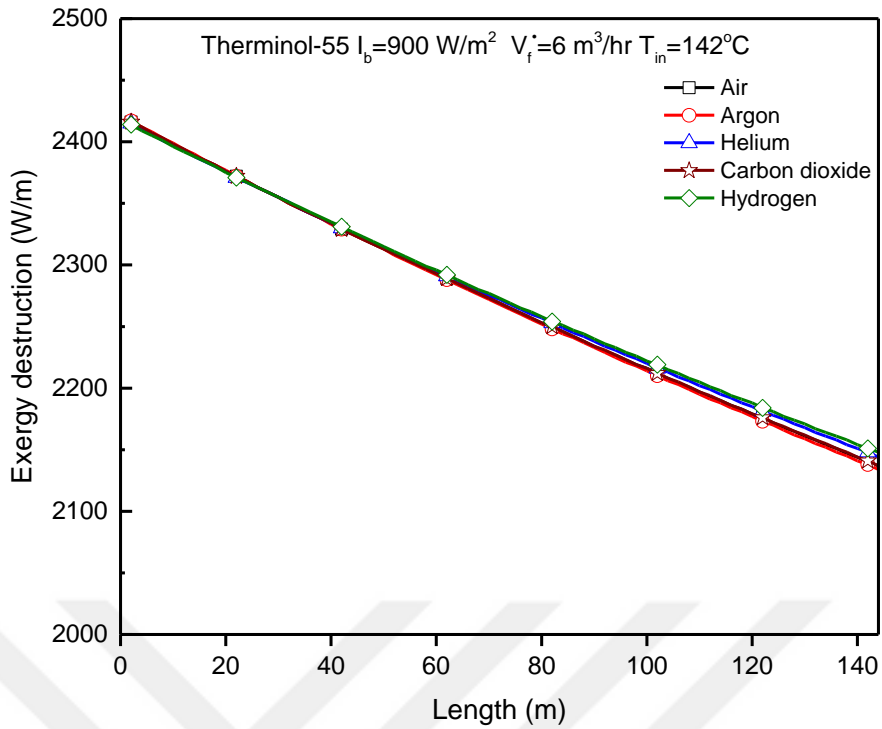


Figure 7.4 Exergy destruction through annular space for five gases along the line of each loop.

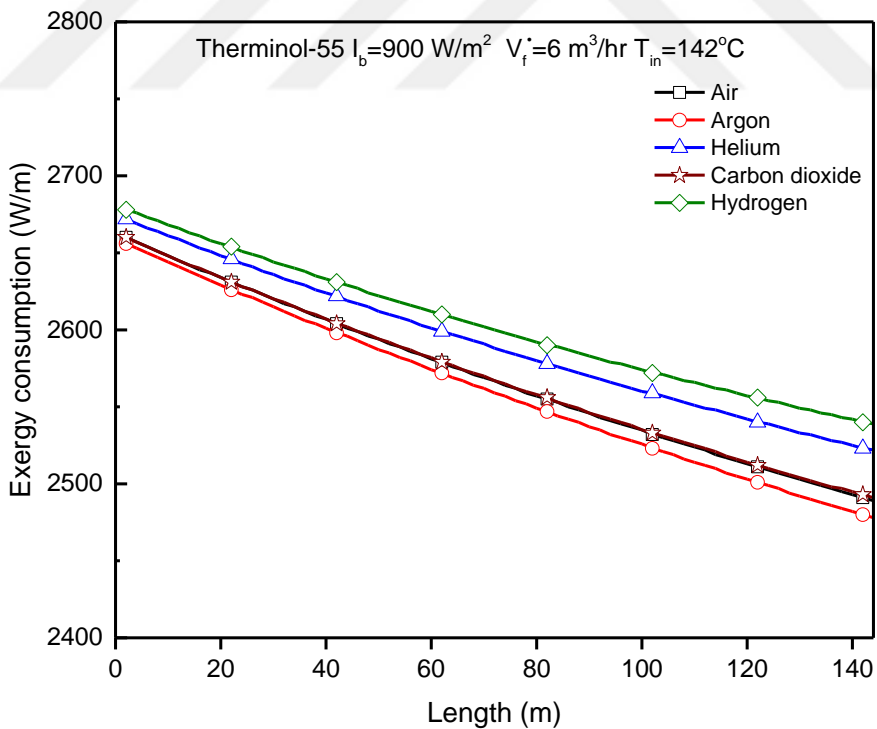


Figure 7.5 Exergy consumption through annular space for five gases along the line of each loop.

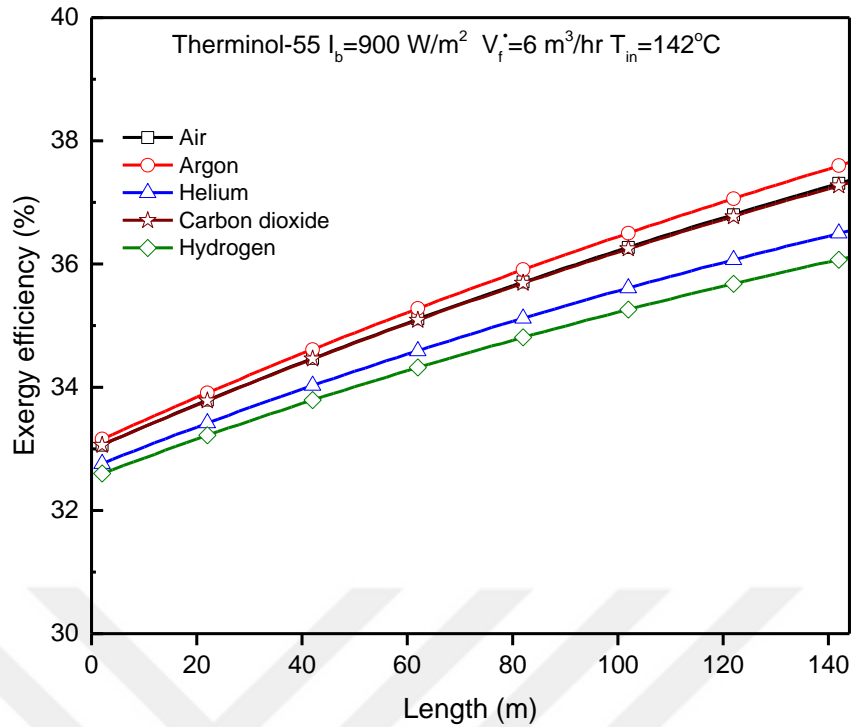


Figure 7.6 Exergy efficiency through annular space for five gases along the line of each loop.

7.2.2 Selective Coatings of Absorber Surface

One parameter that affects the assessment of PTC system is the type of selective coatings for the absorber surface. Black Chrome, Luz Cermet, UVAC-A, UVAC-B and NREL-6A selective coatings are used in the analysis. Figures 7.7 to 10 show the exergy losses, destructions, consumption, and efficiency, respectively, for PTC system after using selective coatings for the absorber surface. As shown in Figure 7.7, the exergy losses for all selective coatings increase along the line of the loop because of the increasing temperature of the absorber surface. NREL-6A increases the exergy loss along the line of the loop from 225 W/m at the beginning of the loop to 323 W/m at the end, which is the lowest value. By contrast, Black Chrome leads to the highest exergy loss, which increases from 261 W/m to 371 W/m. The exergy destructions along the line for each loop is illustrated in Figure 7.8 for the five selective coatings. The exergy destructions gradually decrease due to the increasing temperature of the absorber surface.

The exergy destructions of NREL-6A and Black Chrome decrease from 2465 W/m to 2160 W/m and from 2352 W/m to 2080 W/m, respectively.

As can be seen from Figure 7.9, the exergy consumption decreases because the exergy losses are less than the exergy destructions along the line of the pipe. For NREL-6A, the exergy consumption decreases from 2690 W/m to 2483 W/m at the end of the loop. For Black Chrome, the exergy consumption decreases from 2613 W/m to 2451 W/m, which is the lowest value. The exergy efficiencies of selective coatings are presented in Figure 7.10. The efficiencies are not significant considering the exergy losses and strongly dependent on exergy destructions. The exergy efficiencies for NREL-6A and Black Chrome range from 32.2% at the beginning of the loop to 37% at the end of the loop and from 34.2% to 38.1%, respectively. For example, at a length of 120 m, the exergy efficiency of Black chrome coating is more than 0.6% of the exergy efficiency for Luz Cermet and UVAC-B coatings while the exergy efficiency of Black chrome coating is more than 1.1% of the exergy efficiency for UVAC-A and NREL-6A coatings. These results suggest that it is very important to use selective coatings for such systems, and NREL-6A is the least exergy losses and the highest exergy destructions because of decreasing the outer surface temperature of the annular glass and the absorber, respectively. For that reason, for important of PTC systems, new and more effective selective coatings should be developed.

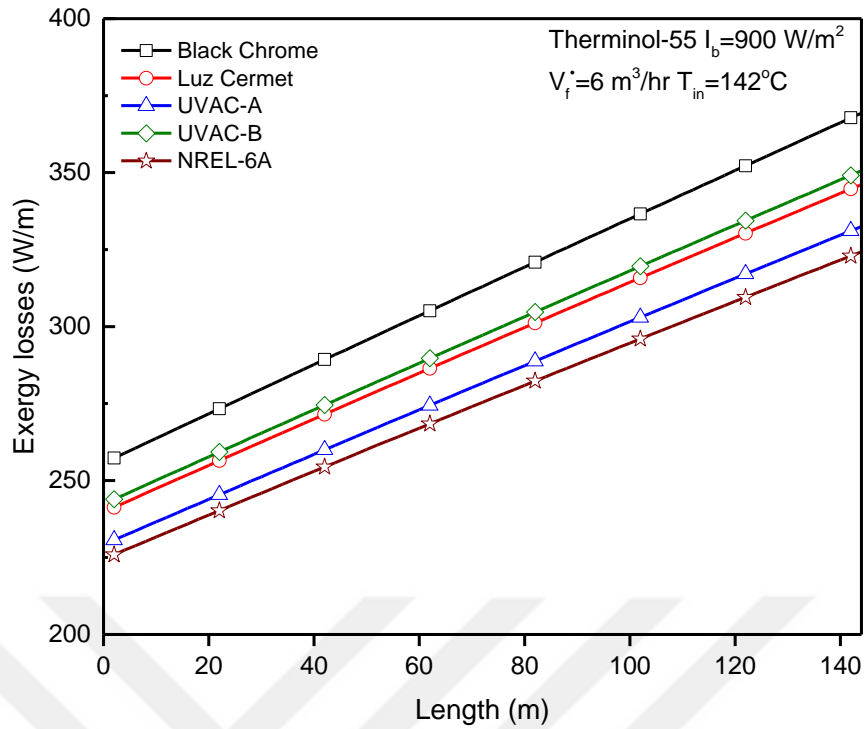


Figure 7.7 Exergy losses through annular space for five selective coatings along the line of each loop.

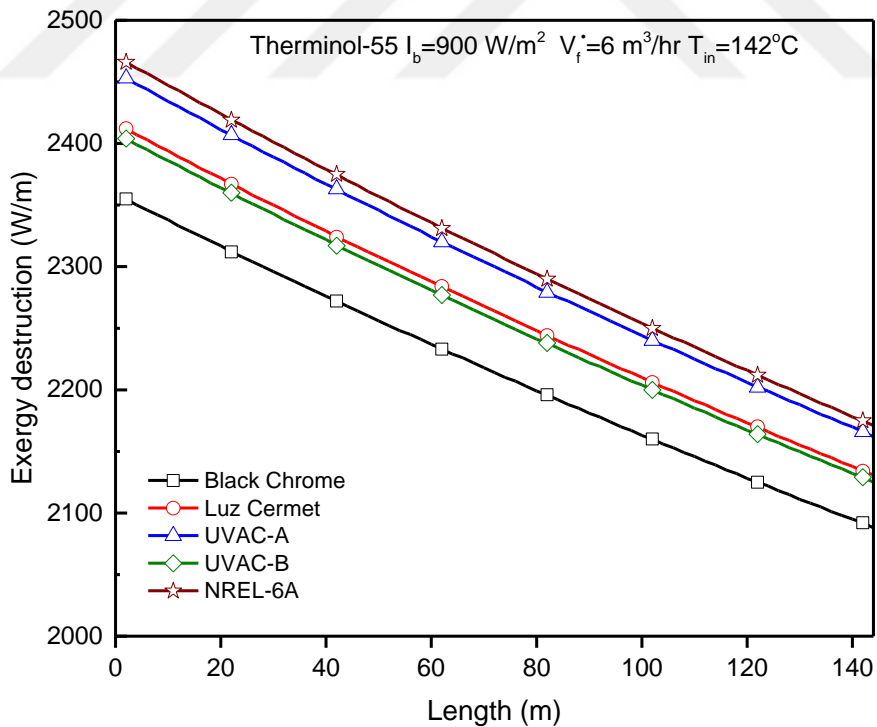


Figure 7.8 Exergy destruction through annular space for five selective coatings along the line of each loop.

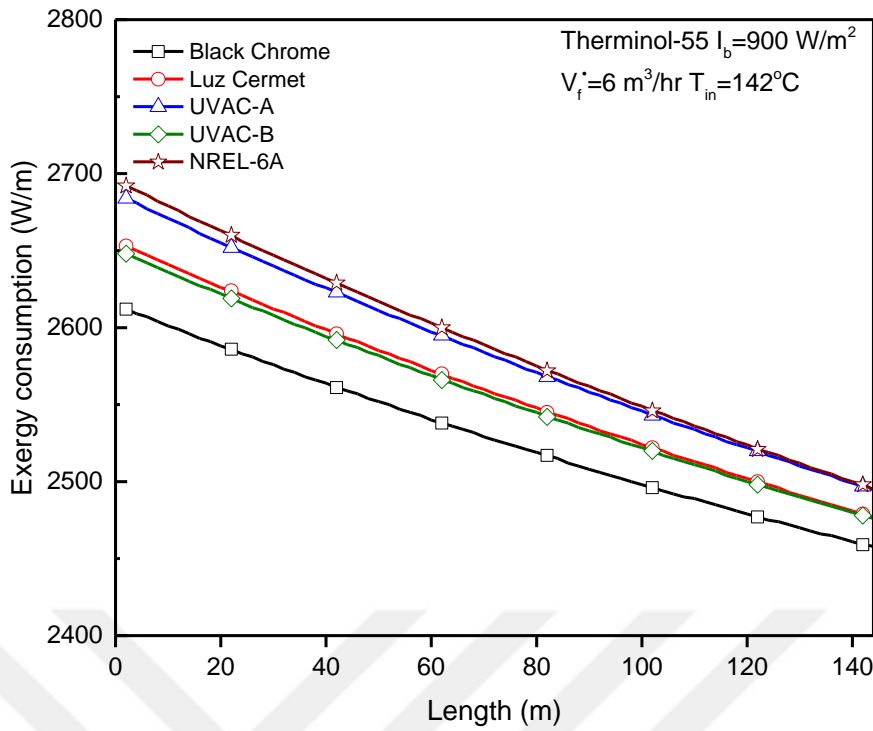


Figure 7.9 Exergy consumption through annular space for five selective coatings along the line of each loop.

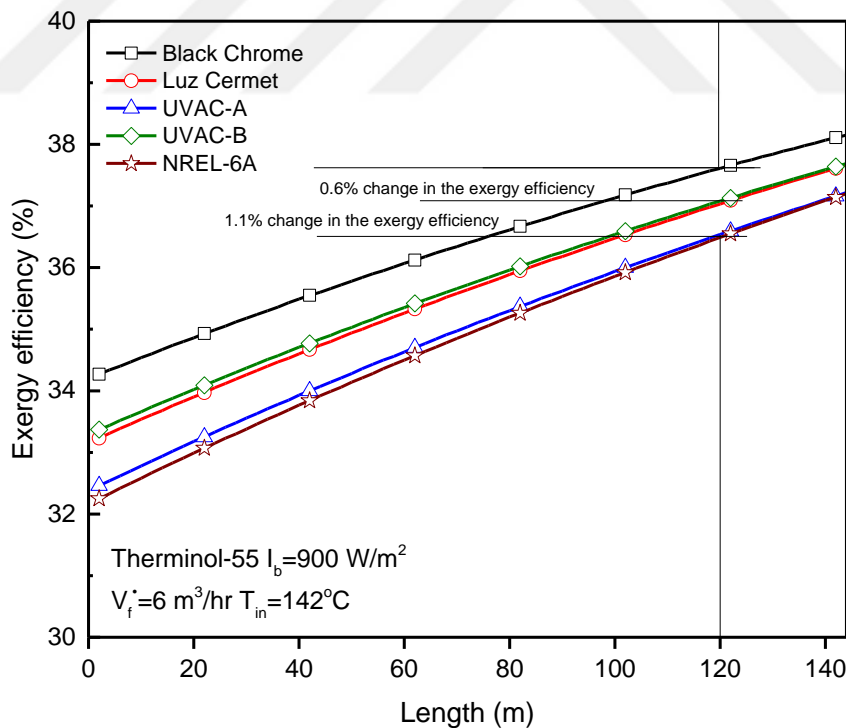


Figure 7.10 Exergy efficiency through annular space for five selective coatings along the line of each loop.

7.2.3 Dimensionless fractions of exergy consumption

These fractions of exergy consumption are significant keys for evaluating the performance of a PTC system. Table 7.1 presents the exergy consumption components as a percentage of the incoming radiation exergy. The exergy fractions are an important complementary tool for determining exergy destructions and losses. The reason of this, the dimensionless parameter describes the percentage of each component from the incoming radiation exergy. Therefore, the importance of these components can be presented.

The results show the fractions of exergy consumption in Figure 7.11. The fraction of exergy destructions of solar radiation from sun and exergy losses due to convection and radiation losses from reflector are unaffected by the length of the absorber because of the constant temperature of the reflector. However, the remaining fractions of exergy consumption are dependent on the absorber surface temperature. Figure 7.11 shows that the highest fraction of exergy consumption due to solar radiation exergy along the line of loop is 60%, whereas the exergy losses fraction caused by the viscous fluid is the lowest (0.1%). The exergy losses caused by the convective heat transfer are higher than those caused by radiative for both of the reflector and the receiver

The percentage fractions of exergy consumption are presented in Figure 7.12. The pie chart shows that more than 86% of the exergy consumption is due to solar radiation transfer, whereas 0.05% of exergy consumption results from the viscous fluid through the receiver. The two types of exergy consumption are destructions and losses. The exergy destruction fractions account for more than 88.3%. Thus, the main fraction of exergy consumption is exergy destructions. The exergy losses consist of the pressure drop, convection losses, and radiation losses and reach less than 11.7%.

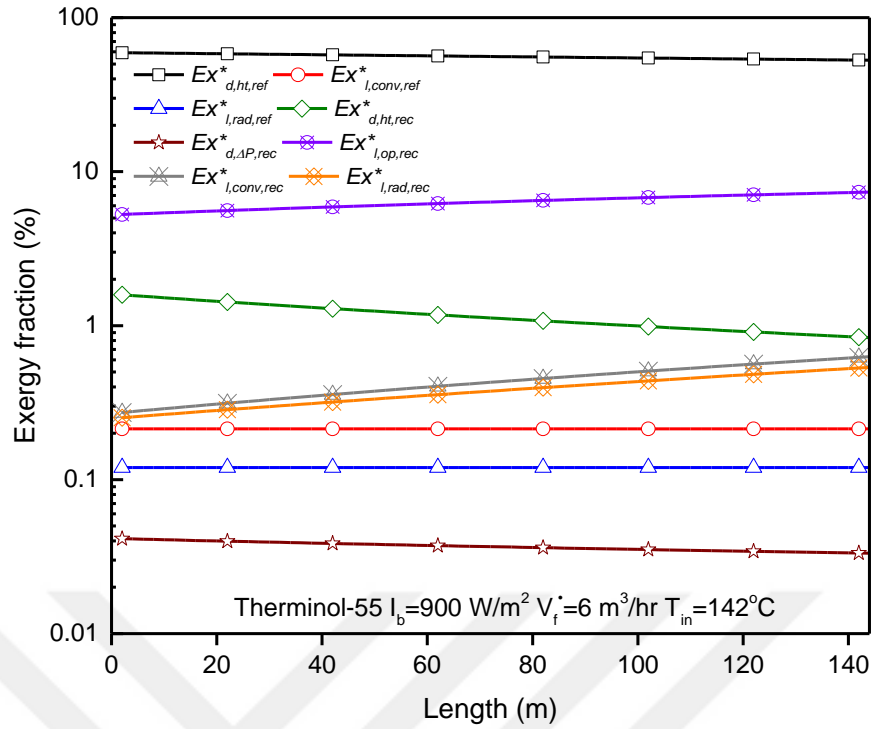


Figure 7.11 Exergy fraction along the line of each loop.

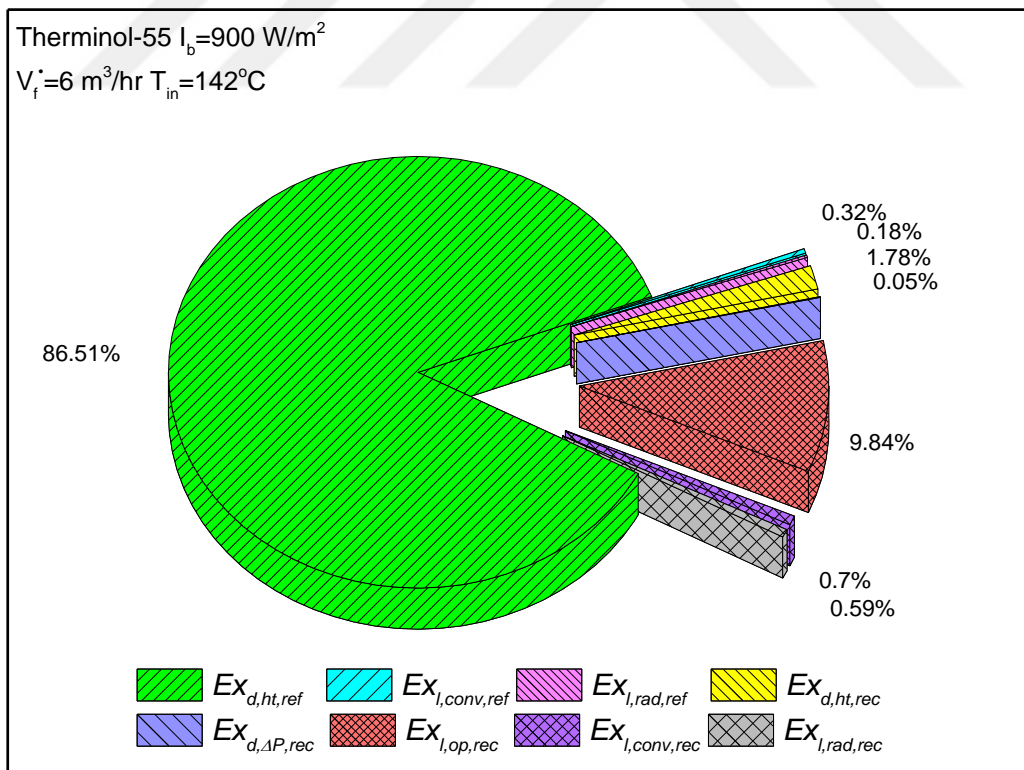


Figure 7.12 The percentages of fraction exergy.

7.2.4 Heat Transfer Fluids

Another parameter investigated to assess the performance of the PTC system is the HTF. Therminol-55, Therminol-59, Dowtherm-MX, and Marlotherm-SH are considered in the present analysis. Figure 7.13 illustrates the results of the exergy analysis of the PTC with four different HTFs. The two parameters of exergy consumption (destructions and losses) are considered. No significant differences in these parameters (i.e., destructions or losses) are evident among the different types of HTF. Figure 7.13 shows the significant effect of the exergy destructions which is the most dominant. Dowtherm-MX leads to the lowest exergy destructions of 162.9 kW at each loop, and Marlotherm-SH and Therminol-59 yield the minimum exergy losses of 21.2 kW.

Figure 7.14 shows the comparison of exergy efficiency among the four HTFs. When the length of the line increases, the exergy efficiency increases because of the increase in the absorber surface temperature. Therefore, the exergy destructions decrease. The difference in the exergy efficiency among the HTFs is minimal. Therminol-59 exhibits the best exergy efficiency of 33.3% at the beginning of the line, whereas Dowtherm-MX has the highest value of 37.6% at the end of loop.

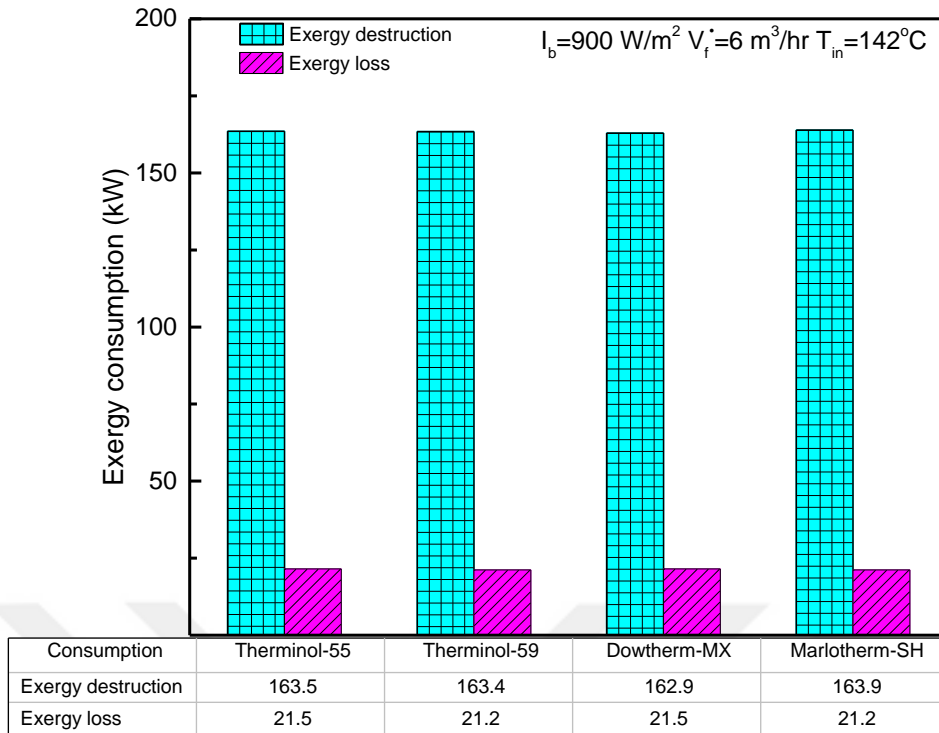


Figure 7.13 Exergy consumption s for four types of heat transfer fluid.

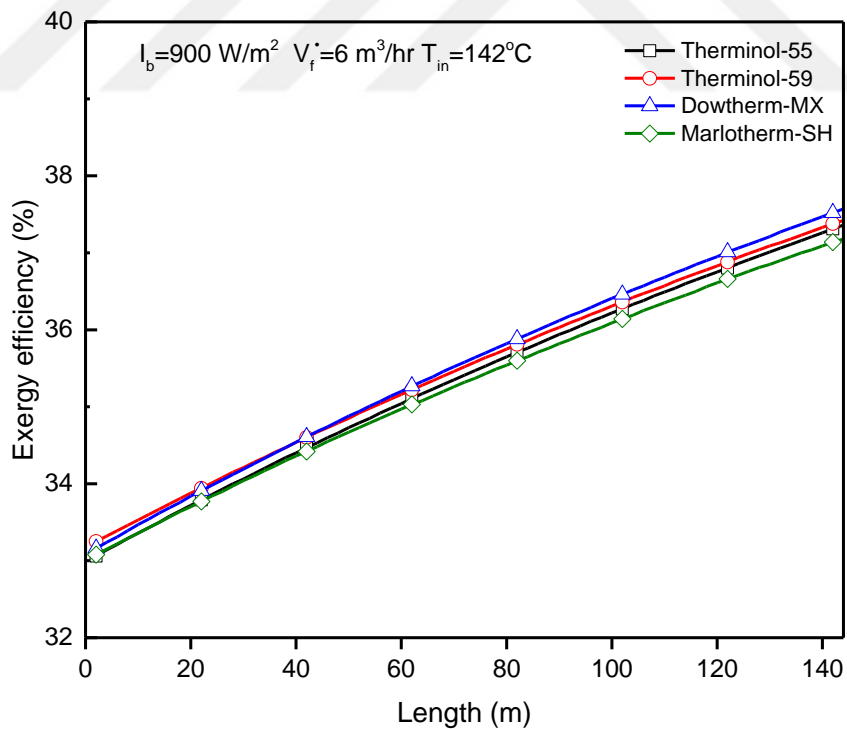


Figure 7.14 Exergy efficiency for four heat transfer fluids along the line of each loop.

7.2.5 Operating Conditions

Analysis under different operating conditions can be conducted to determine the most affected parameter. Inlet temperature, HTF flow rate, and solar irradiance have remarkable effects on the exergy efficiency of the PTC system. Figure 7.15 presents the exergy efficiencies obtained at various inlet temperatures. Increasing the inlet temperature decreases the exergy destructions and thus increases the exergy efficiency. At the beginning of the line of loop, increasing the inlet temperature from 80°C to 170°C increases the exergy efficiency from 27.2% to 35.1%. At the end of the line, the exergy efficiency increases from 33.2% to 37.2%. At a length of 120 m, the exergy efficiency of the inlet temperature (170°C) is more than 5.2% of the exergy efficiency when the inlet temperature is 80°C.

The effect of the HTF flow rate (Figure 7.16) is less significant than that of the inlet temperature. Increasing the flow rate decreases the exergy efficiency and the absorber surface temperature. Therefore, the exergy destructions increase and the exergy efficiency decreases. Here, at a length of 120 m, the exergy efficiency of the flow rate (4 m³/hr) is more than 2.5% of the exergy efficiency when the flow rate is 10 m³/hr.

As shown in Figure 7.17, exergy efficiency is strongly correlated with the third parameter of the operating conditions, namely, solar irradiance of more than 250 W/m². The exergy efficiency increases from 33% to 37.8% when the solar irradiance is 1000 W/m². As a consequence of the increase in the solar irradiance, the outer surface temperature of the absorber increases. The main exergy consumption (exergy destruction) decreases, leading to increased exergy efficiency. For example, at a length of 120 m, the exergy efficiency of the solar irradiance (1000 W/m²) is more than 4.4% of the exergy efficiency when the solar irradiance is 250 W/m².

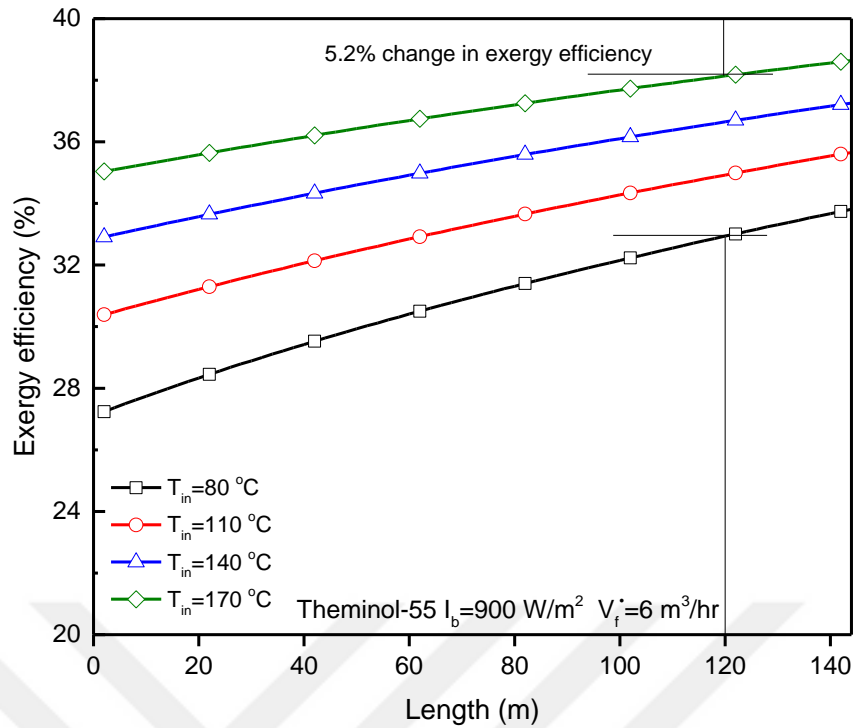


Figure 7.15 Exergy efficiency for four values of temperature along the line of each loop.

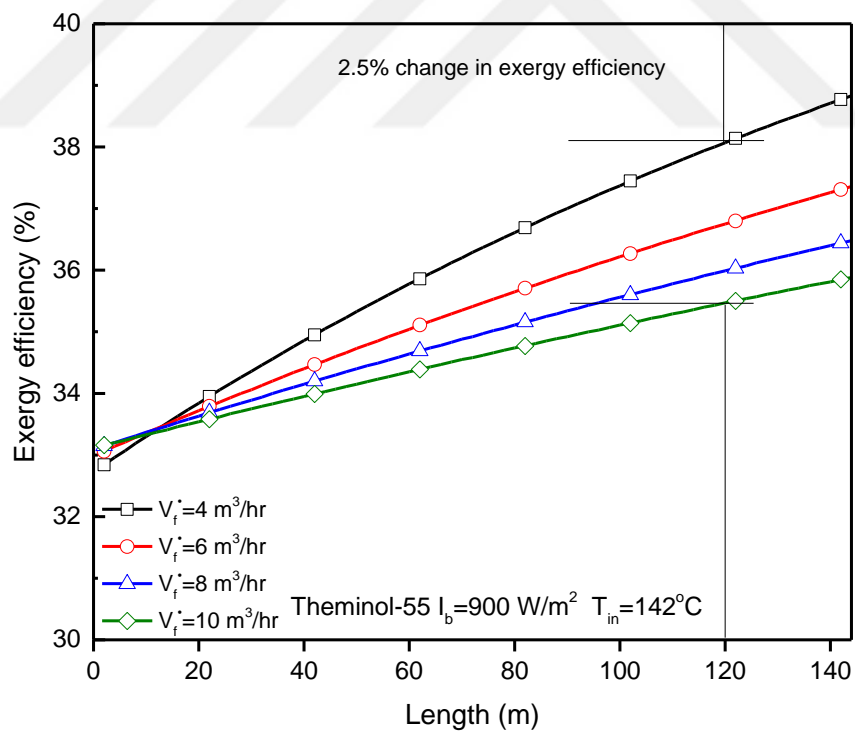


Figure 7.16 Exergy efficiency for four values of flow rate along the line of each loop.

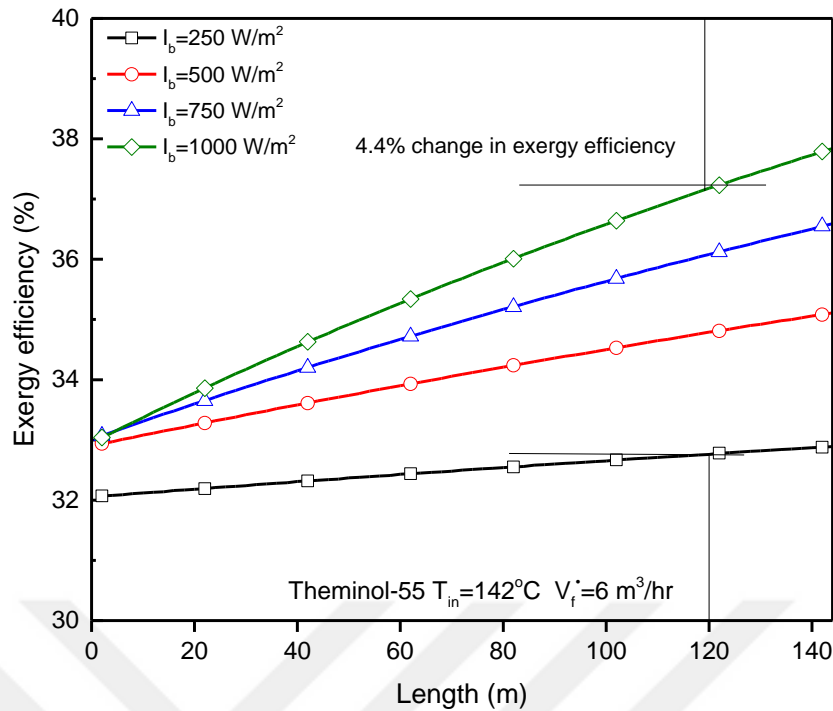


Figure 7.17 Exergy efficiency for four values of solar irradiance along the line of each loop.

7.3 Summary

The aim of this Chapter was to investigate the radiative exergy performance of a PTC system. A comprehensive analysis was performed based on the key parameters of exergy analyses including the exergy losses, destructions, consumption, and efficiency. The results were investigated for five different gases in the annular space, five different selective coatings of absorber surface, and four working fluids all considered using a two-dimensional model. The results show that the main part of exergy consumption is the exergy destructions that produced from solar radiation transfer from the Sun. On the other hand, the effect of the pressure drop in the exergy consumption and efficiency is no significant. That means, the model presented in this Chapter would be essential for evaluating the exergy consumption components and their effect on the performance of PTC systems.

The gas in the annular space plays a significant effect on the exergy consumption and exergy efficiency. This effect dominates the exergy losses due to convection losses which, in turn, affects the performance of a PTC system. The best gas is determined to be Argon. Also, the selective coating is a significant parameter which affects the exergy consumption and exergy efficiency by changing the absorber surface temperature. Among several coating considering here, the best coating is deemed to be Black Chrome. In addition, the type of HTFs has a minimum effect on exergy consumption and exergy efficiency. The best HTF is found to be Dowtherm-MX

This work may confirm the effects of operating conditions on the exergy performance of PTC. The flow rate is inversely proportional to exergy efficiency, whereas the inlet temperature and solar irradiance are directly proportional to the same.

CHAPTER VIII

CONCLUSIONS AND RECOMMENDATIONS FOR FUTURE STUDIES

This dissertation has provided a deeper insight into the radiative energy and exergy analysis of CSP systems, and had five distinct objectives: the first objective was to establish a new methodology for the derivation of a new maximum efficiency expression. The radiative performance of spectrally selective coatings for CSP systems was the second objective. The third objective was to establish a new methodology for predicting spectral solar radiation exergy. To achieve the fourth objective, thermal and radiative performance of a PTC system was investigated thoroughly. Finally, the PTC was assessed based on spectral radiative exergy concept. The methodology for the dissertation is shown in Figure 8.1.

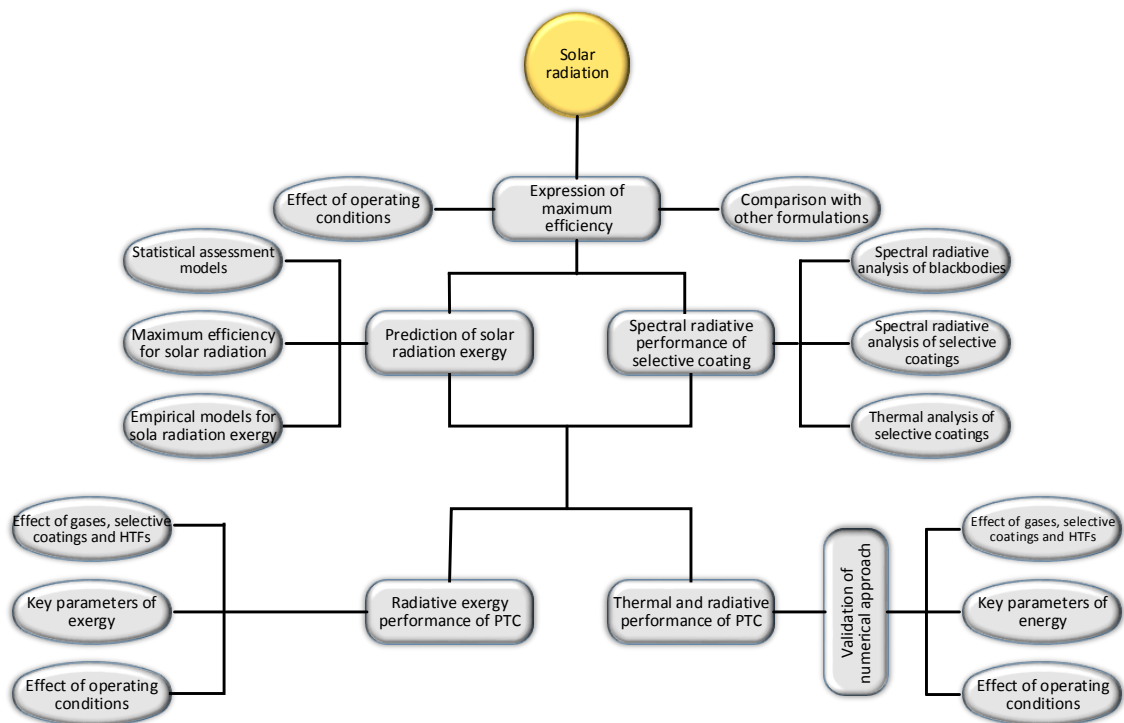


Figure 8.1 Methodology for the dissertation.

The major findings of the dissertation and recommendations for the future works are summarized below.

8.1 Maximum Efficiency for Solar Radiation

The maximum radiative efficiency expressions are derived. The conclusions of this Section are:

- A. In the energy term to determine the maximum radiative efficiency, the temperature of the environment should be taken into account. This is important for applications which have relatively low-temperature differences with the surrounding, in order to obtain more reliable results.
- B. The model deals with an enclosed system that comprises a radiation source and an absorbing sink. Such system is more feasible than the system that involves a cylinder-piston unit.
- C. Comparisons with other studies show that the result obtained in the current formulation is similar to those of other approaches that involve thermal radiation.

8.2 Radiative Performance of Spectrally Selective Coatings for CSP Systems

The radiative performance of spectrally five selective coatings for CSP systems is assessed using radiative energy and radiative exergy analysis models. This analysis is original, as it is carried out in spectral sense the very first time, to our knowledge. The following observations are:

- A. Based on two blackbodies, one as a source ($T=5800$ K) and the other as a receiver ($T=700$ K), the importance of maximum spectral radiative efficiency is clearly supported by the current model, which is based on the spectral behavior of materials as a function of wavelength. The highest value of the maximum radiative efficiency

is found to be 94% in the spectrum of solar radiation, while the lowest value is 84%, which occurs in the infrared region. These results indicate that radiative exergy losses mostly occur in the infrared region for specific coatings used. This can be altered by changing the spectral absorption of coating.

- B. The variations for spectral radiative energy and radiative exergy efficiencies are found to be similar to the variation of spectral emittance for all selective coatings. The highest values of efficiencies for selective coatings are obtained in the solar radiation waveband, while the lowest radiative efficiencies are found in the infrared waveband. The quantity of radiative energy profit at a specific wavelength can be obtained by measuring spectral radiative energy efficiency; while the quality of this radiative energy is determined by spectral radiative exergy efficiency. The spectral radiative energy and radiative exergy gains have peak values for all selective coatings at the wavelength of 500 nm. The greatest radiative energy and radiative exergy gains were observed for NREL-6A coating, while UVAC-B coating has the lowest radiative energy and radiative exergy gains. Spectral radiative energy gains cannot be completely converted to useful work because radiative energy is destroyed through the irreversible process of entropy generation due to emission. Spectral radiative exergy gain, however, can be described as entirely useful work. Therefore, radiative exergy gain can be used to represent how much maximum work can be converted from solar radiation. In addition, spectral radiative exergy gain is always less than spectral radiative energy gain. That said, the true value of the impact of a coating can be measured with the help of radiative exergy gain.
- C. The results obtained under direct normal solar spectral radiation, which has not been previously described, are more reliable and can be used for practical applications. The best overall efficiencies and gains in radiative energy and radiative exergy

analyses were obtained for NREL-6A, while the lowest values are calculated for Luz Cermet. The comparison between the coatings highlighted an unexpected difference between radiative energy and radiative exergy results. The radiative exergy was less than half of the radiative energy regarding efficiency and gain values, showing the significance of how much availability of solar energy can be converted to useful work. Note that the irreversibility on coating surfaces can also play an important role in destroying exergy.

- D. Operating temperature contributed significantly to thermal stability. Within the temperature range of 325 K to 800 K, NREL-6A achieved the best thermal stability and the highest levels of radiative energy and radiative exergy efficiency values. In contrast, Black Chrome coating gave the poorest performance of all the coatings considered in this work.

8.3 The Prediction of Solar Radiation Exergy

The third objective of the present work was to establish a new methodology for predicting solar radiation exergy. In addition, the aim was to construct empirical models as reliable predictors of the exergy value of the monthly average daily horizontal radiation in Iraq and Turkey. The major findings are summarised as follows:

- A. The proposed expression in Chapter two for the maximum efficiency shows no notable difference with other formulas that involve the radiation effects. The results of the Jeter's approach are approximately 2% higher than those of the other approaches (Petela, Spanner, and Proposed expression, see Table 3.1), which are consistent with the predicted effect of radiation transfer. This means, the losses caused by radiation heat transfer are higher than those resulting from the other modes of heat transfer because the energy transfer via radiation is proportional to the fourth

- power of the temperature. However, the present approach is more reliable for the extreme conditions as it is based on more fundamental physics.
- B. When the Eq. (3.35) is used, the maximum conversion efficiency varies between 0.934 and 0.928 from January to August in Karbala, Iraq. The highest and lowest efficiencies are 0.934 and 0.929, which are obtained in February and July, respectively, in Shatra, Iraq. The maximum efficiency in Istanbul, Turkey changes from 0.935 in January to 0.931 in July. Similarly, the efficiency calculated for Aydin, Turkey is 0.935 in January and 0.930 in June. The monthly variations of maximum conversion efficiencies are quite small. However, comparison of the calculation results shows that the expression developed is the most accurate of the ones considered in this work, and can be used later for more reliable economical analysis.
- C. The R^2 of Model 4, values are precise in estimating exergy value of the horizontal global radiation. Similarly, the R^2 values of Model 5 can provide additional evidence on the effects of weather condition parameters on the accuracy of empirical models based on measurements in Iraq and Turkey.
- D. The statistical parameters ($RMSE$, MBE , $MABE$, MPE , $MAPE$, and t_{st}) show that the proposed empirical models can be adopted in Iraq and Turkey for academic and industrial applications. The new proposed model, i.e., Model 5 seems to be the best.

8.4 Thermal and Radiative Performance of a PTC System

The fourth objective of this work is to assess the performance of an existing PTC system through a comprehensive energy analysis. A model was constructed which accounts for all optical components and the heat transfer modes. The optical properties of the selective coatings and the thermal properties of the HTFs are included in the model. The results obtained from the proposed model were compared with the calculations

provided by the manufacturer of the PTC system and against the other results obtained from experimental tests and analytical models. The findings of the present work and the relevant Conclusions reached are listed below:

- A. A complete thermal–radiative energy analysis of an existing PTC system is performed. The reflected and absorbed components of solar radiation between the outer surface of the absorber and the inner surface of the glass envelope are considered. The shape factor between the glass envelope, the reflector, and the sky are accounted for in the calculations. These components are quantitatively analyzed to identify and characterize the heat transfer modes and consequently allow us to reach to reliable results.
- B. The results indicate that the two-dimensional model is necessary to assess the performance of PTC systems, as the heat transfer depends on temperature in both axial and radial axes. The present model allows how to consider the changes in the thermal properties in two dimensions.
- C. Without vacuum conditions, the gas in the annular space can play a significant role on the convection losses. It was observed that the gases in the annular space affect the energy losses in a considerable amount and affect the performance of a PTC system.
- D. The spectral emissivity of selective coatings is a significant parameter for the accurate calculation on the system efficiency by demonstrating the radiation losses from the surface of the absorber. The spectral radiative properties of the selective coatings are dependent on the temperature of outer surface of absorber. While, the temperature of the inner surface of the glass envelope depends on the spectral radiative properties of these coatings.

- E. The optical losses are independent on the length of the loop and accounted for the largest percentage of the losses. While, the second largest percentage of losses are the thermal losses which attributed to the rising temperature of the outer surface of the absorber as the length of the loop increases. Therefore, the thermal efficiency of the PTC is reduced along the line of the loop.

8.5 Thermal and Radiative Exergy Performance of a PTC System

To achieve the fifth objective of this dissertation, the exergy performance of a PTC system was investigated. A comprehensive analysis was conducted which accounts for all key parameters of exergy consumption components. The work is specifically focused on determination of exergy efficiency and particularly on spectral radiative exergy analysis. For this, a series of fundamental expressions are derived. The results were obtained for five different gases in the annular space, five different selective coatings of absorber surface, and four working fluids all considered using a two-dimensional model. The findings of this study contribute in several ways to our understanding of exergy analysis and provide a basis for optimizing the performance for a PTC system. The major findings are summarised as follows:

- A. A detail exergy analysis is presented for a PTC system based on energy analysis. Exergy analysis cannot be a substitute for the energy analysis, yet it provides a complementary tool to determine the useful work and unrecoverable losses, that lead to improving the system.
- B. The key parameters of exergy analyses include exergy losses, destructions, consumption, and efficiency. These parameters are quantitatively analyzed to evaluate and characterize the exergy model.

- C. Based on the two-dimensional model, the results show that the main part of exergy consumption is the exergy destructions that produced from solar radiation transfer from the Sun. On the other hand, the effect of the pressure drop in the exergy consumption and efficiency is no significant. That means, the present model is necessary for evaluating the exergy consumption components and their effect on the performance of PTC systems.
- D. The gas in the annular space plays a significant effect on the exergy consumption and exergy efficiency. This effect dominates the exergy losses due to convection losses which consider and affect the performance of a PTC system. The best gas is determined to be Argon.
- E. The spectrally selective coating is a significant parameter affects the exergy consumption and exergy efficiency. Its impact depends on the absorber surface temperature, as the spectral radiative properties of the selective coatings are dependent on the absorber surface temperature. Therefore, this parameter controls the radiation losses from the surface of the absorber and the exergy efficiency, and can be determined only if a spectral analysis is carried out. The best coating is deemed to be Black Chrome.
- F. Type of HTFs has a minimum effect on exergy consumption and exergy efficiency. The best HTF is found to be Dowtherm-MX
- G. This study may confirm the effect of operating conditions on the exergy performance of PTC. The flow rate is inversely proportional to exergy efficiency, whereas the inlet temperature and solar irradiance are directly proportional to the same.

8.6 Recommendations Future Works

Further studies on the spectral analysis of different spectrally selective coatings should be done for solar power systems. Such work should also include the effects of coupled heat transfer problem with convection and radiation.

In addition, additional future studies of the spectral exergy approach would be of interest, as they can be used for several solar problems and for the radiative cooling by coating of buildings.

Furthermore, the prediction models should include the effects of other parameters of weather conditions, such as the relative humidity. Also, new empirical models can be constructed to estimate monthly average daily horizontal global radiation exergy for different climatic conditions worldwide by considering latitudes and longitudes.

Finally, on the basis of the promising findings presented in exergy analysis for the selective coatings and a PTC system, work on the exergoeconomic analysis should be presented in future research.

LIST OF REFERENCES

- [1] J. Sun, Q. Liu, H. Hong, Numerical study of parabolic-trough direct steam generation loop in recirculation mode: characteristics, performance and general operation strategy, *Energy Conversion and Management* 96 (2015) 287-302.
- [2] L.S. Conrado, A. Rodríguez-Pulido, G. Calderón, Thermal performance of parabolic trough solar collectors, *Renewable and Sustainable Energy Reviews* 67 (2017) 1345-1359.
- [3] H. Zhang, J. Baeyens, J. Degrève, G. Cacères, Concentrated solar power plants: Review and design methodology, *Renewable and Sustainable Energy Reviews* 22 (2013) 466-481.
- [4] W. Stein, R. Buck, Advanced power cycles for concentrated solar power, *Solar Energy* 152 (2017) 91-105.
- [5] A. Fernández-García, E. Zarza, L. Valenzuela, M. Pérez, Parabolic-trough solar collectors and their applications, *Renewable and Sustainable Energy Reviews* 14 (7) (2010) 1695-1721.
- [6] J.R. Howell, M.P. Menguc, R. Siegel, Thermal radiation Heat Transfer, 6th ed., CRC press 2016.
- [7] K.M. McCord, D.A. Klinglesmith, C.A. Jurgenson, E.J. Bakker, R.A. Schmall, R.A. Schmall, D. Gartner, A. Jaramillo, K. Romero, A. Rael, Characterization of Silver and Aluminum custom mirror coatings for the MRO interferometric telescopes, Optical Materials and Structures Technologies IV, International Society for Optics and Photonics, 2009, p. 74250V-74250V9.
- [8] V.S. Reddy, S. Kaushik, K. Ranjan, S. Tyagi, State-of-the-art of solar thermal power plants- A review, *Renewable and Sustainable Energy Reviews* 27 (2013) 258-273.
- [9] E. Bellos, C. Tzivanidis, K.A. Antonopoulos, A detailed working fluid investigation for solar parabolic trough collectors, *Applied Thermal Engineering* 114 (2017) 374-386.
- [10] M. Liu, N.H.S. Tay, S. Bell, M. Belusko, R. Jacob, G. Will, W. Saman, F. Bruno, Review on concentrating solar power plants and new developments in high temperature thermal energy storage technologies, *Renewable and Sustainable Energy Reviews* 53 (2016) 1411-1432.
- [11] D.C. Spanner, Introduction to thermodynamics, Academic Press, London, 1964.
- [12] S.M. Jeter, Maximum conversion efficiency for the utilization of direct solar radiation, *Solar Energy* 26 (3) (1981) 231-236.
- [13] B. Project, Turkish demo site.2014 <<http://www.bricker-project.com/>>, [accessed March, 2018].
- [14] Soltigua, PTMx. 2007 <<http://www.soltigua.com/>>, [accessed May, 2018].
- [15] I. Dincer, The role of exergy in energy policy making, *Energy Policy* 30 (2) (2002) 137-149.
- [16] I. Dincer, Y.A. Cengel, Energy, entropy and exergy concepts and their roles in thermal engineering, *Entropy* 3 (3) (2001) 116-149.
- [17] I. Dincer, M.A. Rosen, Exergy: Energy, Environment and Sustainable Development, Newnes 2012.
- [18] R. Petela, Exergy of Heat Radiation, *Journal of Heat Transfer* 86 (2) (1964) 187-192.
- [19] J. Parrott, Theoretical upper limit to the conversion efficiency of solar energy, *Solar Energy* 21 (3) (1978) 227-229.
- [20] J. Osterle, The second law efficiency of solar energy conversion, *Journal of Solar Energy Engineering* 106 (1984) 17.

- [21] S. Wright, M. Rosen, D. Scott, J. Haddow, The exergy flux of radiative heat transfer for the special case of blackbody radiation, *Exergy, An International Journal* 2 (1) (2002) 24-33.
- [22] R. Petela, Exergy of undiluted thermal radiation, *Solar Energy* 74 (6) (2003) 469-488.
- [23] S. Kabelac, Exergy of solar radiation, *INTERNATIONAL JOURNAL OF ENERGY TECHNOLOGY AND POLICY* 3 (1/2) (2005) 115-122.
- [24] K. Lovegrove, W. Stein, *Concentrating Solar Power Technology: Principles, Developments and Applications*, 1st ed., Elsevier 2012.
- [25] K. Burlafinger, A. Vetter, C.J. Brabec, Maximizing concentrated solar power (CSP) plant overall efficiencies by using spectral selective absorbers at optimal operation temperatures, *Solar Energy* 120 (2015) 428-438.
- [26] S. Karlsson, The exergy of incoherent electromagnetic radiation, *Physica Scripta* 26 (4) (1982) 329.
- [27] Y. Candau, On the exergy of radiation, *Solar Energy* 75 (3) (2003) 241-247.
- [28] R. Petela, Radiation spectra of surface, *International Journal of Exergy* 7 (1) (2009) 89-109.
- [29] S. Wijewardane, Y. Goswami, Exergy of partially coherent thermal radiation, *Energy* 42 (1) (2012) 497-502.
- [30] D. Allerd, J. Reyes, J. Pionkowski, *Selective absorber amorphous alloys and devices*, 1986.
- [31] C. Atkinson, C.L. Sansom, H.J. Almond, C.P. Shaw, Coatings for concentrating solar systems—A review, *Renewable and Sustainable Energy Reviews* 45 (2015) 113-122.
- [32] T. Bostrom, Nickel-alumina coated solar absorbers, Google Patents, 2006.
- [33] H.C. Hottel, T. Unger, 2 The properties of a copper oxide-aluminum selective black surface absorber of solar energy, *Solar Energy* 3 (3) (1959) 10-15.
- [34] P. Driver, R. Jones, C. Riddiford, R. Simpson, A new chrome black selective absorbing surface, *Solar Energy* 19 (3) (1977) 301-306.
- [35] C.E. Kennedy, Review of mid-to high-temperature solar selective absorber materials, National Renewable Energy Laboratory Golden, Colo, USA2002.
- [36] R. Mahoney, HCE issues; cermet preliminary results, optical properties, and construction forum, Presentation at Solar Forum 2001, *Solar Energy: The Power to Choose* (2001).
- [37] C.E. Kennedy, Progress to develop an advanced solar-selective coating, National Renewable Energy Laboratory (NREL), Golden, CO., 2008.
- [38] C. Kennedy, H. Price, Progress in development of high-temperature solar-selective coating, ASME 2005 International Solar Energy Conference, American Society of Mechanical Engineers, 2005, pp. 749-755.
- [39] L. Zheng, F. Gao, S. Zhao, F. Zhou, J.P. Nshimiyimana, X. Diao, Optical design and co-sputtering preparation of high performance Mo–SiO₂ cermet solar selective absorbing coating, *Applied Surface Science* 280 (2013) 240-246.
- [40] Y. Ning, W. Wang, L. Wang, Y. Sun, P. Song, H. Man, Y. Zhang, B. Dai, J. Zhang, C. Wang, Optical simulation and preparation of novel Mo/ZrSiN/ZrSiON/SiO₂ solar selective absorbing coating, *Solar Energy Materials and Solar Cells* 167 (2017) 178-183.
- [41] P. Hu, Y. Liu, Q. Zhang, Z. Chen, Thermodynamic analysis on medium-high temperature solar thermal systems with selective coatings, *Science China Technological Sciences* 56 (12) (2013) 3137-3143.
- [42] C. Kandilli, Exergoeconomic analysis of a novel concentrated solar energy for lighting-power generation combined system based on spectral beam splitting, *International Journal of Exergy* 21(2) (2016) 239-260.
- [43] W.B. Wan Nik, M.Z. Ibrahim, K.B. Samo, A.M. Muzathik, Monthly mean hourly global solar radiation estimation, *Solar Energy* 86 (1) (2012) 379-387.

- [44] O. Kwon, Y.J. Yoon, S.K. Moon, H.J. Choi, J.H. Shim, Estimation of Singapore's hourly solar radiation using hybrid-Markov transition matrices method, *International Journal of Precision Engineering and Manufacturing* 14 (2) (2013) 323-327.
- [45] K. Lee, H. Yoo, G.J. Levermore, Quality control and estimation hourly solar irradiation on inclined surfaces in South Korea, *Renewable Energy* 57 (2013) 190-199.
- [46] M.J. Ahmad, G.N. Tiwari, Solar radiation models A review, *International Journal of Energy Research* 35 (4) (2011) 271-290.
- [47] A. Angstrom, Solar and terrestrial radiation. Report to the international commission for solar research on actinometric investigations of solar and atmospheric radiation, *Quarterly Journal of the Royal Meteorological Society* 50 (210) (1924) 121-126.
- [48] J. Prescott, Evaporation from a water surface in relation to solar radiation, *Transactions of the Royal Society of South Australia* 64 (1) (1940) 114-118.
- [49] M. Iris, C. Tiris, Y. Erdalli, Water heating system by solar energy. Marmara research centre, Institute of Energy systems and environmental research, NATO-TU-COATING, Gebze, Turkey, 1997.
- [50] J. Page, The estimation of monthly mean values of daily total short-wave radiation on vertical surfaces from sunshine records for latitude 40 N-40 S, UN Conf. on New Sources of Energy, Paper No. S/98, 1967.
- [51] H. Ögelman, A. Ecevit, E. Tasdemiroğlu, A new method for estimating solar radiation from bright sunshine data, *Solar Energy* 33 (6) (1984) 619-625.
- [52] B. Akinoğlu, A. Ecevit, A further comparison and discussion of sunshine-based models to estimate global solar radiation, *Energy* 15 (10) (1990) 865-872.
- [53] V. Bahel, H. Bakhsh, R. Srinivasan, A correlation for estimation of global solar radiation, *Energy* 12 (2) (1987) 131-135.
- [54] T. Samuel, Estimation of global radiation for Sri Lanka, *Solar Energy* 47 (5) (1991) 333-337.
- [55] N. Arslanoglu, Empirical modeling of solar radiation exergy for Turkey, *Applied Thermal Engineering* 108 (2016) 1033-1040.
- [56] S. Quoilin, M. Orosz, H. Hemond, V. Lemort, Performance and design optimization of a low-cost solar organic Rankine cycle for remote power generation, *Solar Energy* 85 (5) (2011) 955-966.
- [57] J. Wang, Z. Yan, P. Zhao, Y. Dai, Off-design performance analysis of a solar-powered organic Rankine cycle, *Energy Conversion and Management* 80 (2014) 150-157.
- [58] M. Borunda, O. Jaramillo, R. Dorantes, A. Reyes, Organic Rankine Cycle coupling with a Parabolic Trough Solar Power Plant for cogeneration and industrial processes, *Renewable Energy* 86 (2016) 651-663.
- [59] M. Yaghoubi, K. Azizian, A. Kenary, Simulation of Shiraz solar power plant for optimal assessment, *Renewable Energy* 28 (12) (2003) 1985-1998.
- [60] R. Tamme, D. Laing, W.-D. Steinmann, Advanced thermal energy storage technology for parabolic trough, *Journal of Solar Energy Engineering* 126(2) (2004) 794-800.
- [61] C. Kennedy, H. Price, Progress in development of high-temperature solar-selective coating, International Solar Energy Conference, Orlando, Florida USA, 2005.
- [62] V. Jebasingh, G.J. Herbert, A review of solar parabolic trough collector, *Renewable and Sustainable Energy Reviews* 54 (2016) 1085-1091.
- [63] D. Zhao, E. Xu, Z. Wang, Q. Yu, L. Xu, L. Zhu, Influences of installation and tracking errors on the optical performance of a solar parabolic trough collector, *Renewable Energy* 94 (2016) 197-212.
- [64] R. Forristall, Heat transfer analysis and modeling of a parabolic trough solar receiver implemented in engineering equation solver, National Renewable Energy Laboratory 2003.
- [65] W. Fuqiang, C. Ziming, T. Jianyu, Y. Yuan, S. Yong, L. Linhua, Progress in concentrated solar power technology with parabolic trough collector system: A comprehensive review, *Renewable and Sustainable Energy Reviews* 79 (2017) 1314-1328.
- [66] S.A. Kalogirou, Solar thermal collectors and applications, *Progress in energy and combustion science* 30 (3) (2004) 231-295.

- [67] R.V. Padilla, G. Demirkaya, D.Y. Goswami, E. Stefanakos, M.M. Rahman, Heat transfer analysis of parabolic trough solar receiver, *Applied Energy* 88 (12) (2011) 5097-5110.
- [68] A.M. de Oliveira Siqueira, P.E.N. Gomes, L. Torrezani, E.O. Lucas, G.M. da Cruz Pereira, Heat transfer analysis and modeling of a parabolic trough solar collector: an analysis, *Energy Procedia* 57 (2014) 401-410.
- [69] E.M. Mokheimer, Y.N. Dabwan, M.A. Habib, S.A. Said, F.A. Al-Sulaiman, Techno-economic performance analysis of parabolic trough collector in Dhahran, Saudi Arabia, *Energy Conversion and Management* 86 (2014) 622-633.
- [70] A. Mwesigye, İ.H. Yılmaz, J.P. Meyer, Numerical analysis of the thermal and thermodynamic performance of a parabolic trough solar collector using SWCNTs-Therminol® VP-1 nanofluid, *Renewable Energy* 10 (2017) S0960148117310108.
- [71] O.K. Sadaghiyani, M.S. Boubakran, A. Hassanzadeh, Energy and exergy analysis of parabolic trough collectors, *INTERNATIONAL JOURNAL OF HEAT AND TECHNOLOGY* 36 (1) (2018) 147-158.
- [72] A. Mwesigye, J.P. Meyer, Optimal thermal and thermodynamic performance of a solar parabolic trough receiver with different nanofluids and at different concentration ratios, *Applied Energy* 193 (2017) 393-413.
- [73] A.K. Hussein, Applications of nanotechnology to improve the performance of solar collectors—recent advances and overview, *Renewable and Sustainable Energy Reviews* 62 (2016) 767-792.
- [74] A. Mwesigye, Z. Huan, J.P. Meyer, Thermal performance and entropy generation analysis of a high concentration ratio parabolic trough solar collector with Cu-Therminol® VP-1 nanofluid, *Energy conversion and management* 120 (2016) 449-465.
- [75] A.A. AlZahrani, I. Dincer, Energy and exergy analyses of a parabolic trough solar power plant using carbon dioxide power cycle, *Energy Conversion and Management* 158 (2018) 476-488.
- [76] E. Bellos, C. Tzivanidis, Parametric investigation of supercritical carbon dioxide utilization in parabolic trough collectors, *Applied Thermal Engineering* 127 (2017) 736-747.
- [77] M. Chafie, M.F.B. Aissa, A. Guizani, Energetic end exergetic performance of a parabolic trough collector receiver: An experimental study, *Journal of Cleaner Production* 171 (2018) 285-296.
- [78] J. Guo, X. Huai, Z. Liu, Performance investigation of parabolic trough solar receiver, *Applied Thermal Engineering* 95 (2016) 357-364.
- [79] E. Bellos, C. Tzivanidis, A detailed exergetic analysis of parabolic trough collectors, *Energy Conversion and Management* 149 (2017) 275-292.
- [80] J. Guo, X. Huai, Multi-parameter optimization design of parabolic trough solar receiver, *Applied Thermal Engineering* 98 (2016) 73-79.
- [81] F.A. Al-Sulaiman, Exergy analysis of parabolic trough solar collectors integrated with combined steam and organic Rankine cycles, *Energy Conversion and Management* 77 (2014) 441-449.
- [82] S.A. Kalogirou, S. Karellas, V. Badescu, K. Braimakis, Exergy analysis on solar thermal systems: a better understanding of their sustainability, *Renewable Energy* 85 (2016) 1328-1333.
- [83] R.V. Padilla, A. Fontalvo, G. Demirkaya, A. Martinez, A.G. Quiroga, Exergy analysis of parabolic trough solar receiver, *Applied Thermal Engineering* 67 (1) (2014) 579-586.
- [84] S. Tyagi, S. Wang, M. Singhal, S. Kaushik, S. Park, Exergy analysis and parametric study of concentrating type solar collectors, *International Journal of Thermal Sciences* 46(12) (2007) 1304-1310.
- [85] H. Nezammahalleh, Exergy analysis of DSG parabolic trough collectors for the optimal integration with a combined cycle, *International Journal of Exergy* 16 (1) (2015) 72-96.
- [86] F. Chen, M. Li, P. Zhang, X. Luo, Thermal performance of a novel linear cavity absorber for parabolic trough solar concentrator, *Energy Conversion and Management* 90 (2015) 292-299.
- [87] İ. Ceylan, A. Ergun, Thermodynamic analysis of a new design of temperature controlled parabolic trough collector, *Energy Conversion and Management* 74 (2013) 505-510.

- [88] A. Bejan, *Advanced engineering thermodynamics*, John Wiley & Sons, Hoboken, N.J., 2006.
- [89] G.P. Beretta, E.P. Gyftopoulos, Electromagnetic radiation: a carrier of energy and entropy, *Journal of Energy Resources Technology* 137 (2) (2015) 021005.
- [90] Y. Liu, P. Hu, Q. Zhang, Z. Chen, Thermodynamic and optical analysis for a CPV/T hybrid system with beam splitter and fully tracked linear Fresnel reflector concentrator utilizing sloped panels, *Solar Energy* 103 (2014) 191-199.
- [91] G.E. McDonald, Spectral reflectance properties of black chrome for use as a solar selective coating, *Solar Energy* 17(2) (1975) 119-122.
- [92] J. Sweet, R. Pettit, M. Chamberlain, Optical modeling and aging characteristics of thermally stable black chrome solar selective coatings, *Solar Energy Materials* 10(3-4) (1984) 251-286.
- [93] M. Geyer, E. Lüpfert, R. Osuna, A. Esteban, W. Schiel, A. Schweitzer, E. Zarza, P. Nava, J. Langenkamp, E. Mandelberg, EUROROUGH-Parabolic trough collector developed for cost efficient solar power generation, 11th International symposium on concentrating solar power and chemical energy technologies, 2002, pp. 04-06.
- [94] A. Rabl, *Active solar collectors and their applications*, Oxford University Press on Demand 1985.
- [95] O. García-Valladares, N. Velázquez, Numerical simulation of parabolic trough solar collector: Improvement using counter flow concentric circular heat exchangers, *International Journal of Heat and Mass Transfer* 52 (3-4) (2009) 597-609.
- [96] A. Hachicha, I. Rodríguez, R. Capdevila, A. Oliva, Heat transfer analysis and numerical simulation of a parabolic trough solar collector, *Applied Energy* 111 (2013) 581-592.
- [97] S. Adhikari, Seasonal and spatial variation of solar radiation in Nepal Himalayas, *Journal of Hydrology and Meteorology* 8 (1) (2016) 1-9.
- [98] S. Racharla, K. Rajan, Solar tracking system—a review, *International Journal of Sustainable Engineering* 10 (2) (2017) 72-81.
- [99] H. Khorasanizadeh, K. Mohammadi, A. Mostafaiepour, Establishing a diffuse solar radiation model for determining the optimum tilt angle of solar surfaces in Tabass, Iran, *Energy Conversion and Management* 78 (2014) 805-814.
- [100] M. Rizwan, M. Jamil, S. Kirmani, D. Kothari, Fuzzy logic based modeling and estimation of global solar energy using meteorological parameters, *Energy* 70 (2014) 685-691.
- [101] S. Kaplanis, J. Kumar, E. Kaplani, On a universal model for the prediction of the daily global solar radiation, *Renewable Energy* 91 (2016) 178-188.
- [102] M.S. Mecibah, T.E. Boukelia, R. Tahtah, K. Gairaa, Introducing the best model for estimation the monthly mean daily global solar radiation on a horizontal surface (Case study: Algeria), *Renewable and Sustainable Energy Reviews* 36 (2014) 194-202.
- [103] K. Mohammadi, S. Shamshirband, M.H. Anisi, K.A. Alam, D. Petković, Support vector regression based prediction of global solar radiation on a horizontal surface, *Energy Conversion and Management* 91 (2015) 433-441.
- [104] Z. Ramedani, M. Omid, A. Keyhani, S. Shamshirband, B. Khoshnevisan, Potential of radial basis function based support vector regression for global solar radiation prediction, *Renewable and Sustainable Energy Reviews* 39 (2014) 1005-1011.
- [105] R. Yacef, A. Mellit, S. Belaid, Z. Şen, New combined models for estimating daily global solar radiation from measured air temperature in semi-arid climates: application in Ghardaia, Algeria, *Energy Conversion and Management* 79 (2014) 606-615.
- [106] A.K. Yadav, S. Chandel, Solar radiation prediction using Artificial Neural Network techniques: A review, *Renewable and Sustainable Energy Reviews* 33 (2014) 772-781.
- [107] H.N. Mohammed, M.P. Mengüç, Solar radiation exergy and quality performance for Iraq and Turkey, *International Journal of Exergy* 25 (4) (2018) 364-385.
- [108] L. Ancarani, Datasheet of PTMx collector. 22 December, 2017 [lancarani@soltigua.com].
- [109] J.A. Duffie, W.A. Beckman, *Solar engineering of thermal processes*, John Wiley and Sons 2013.
- [110] İ.H. Yılmaz, M.S. Söylemez, Thermo-mathematical modeling of parabolic trough collector, *Energy Conversion and Management* 88 (2014) 768-784.

- [111] H.M. Güven, R.B. Bannerot, Determination of error tolerances for the optical design of parabolic troughs for developing countries, *Solar Energy* 36 (6) (1986) 535-550.
- [112] R. Bannerot, Derivation of Universal Error Parameters for Comprehensive Optical Analysis of Parabolic Troughs¹, *Journal of Solar Energy Engineering* 108 (1986) 275.
- [113] T. Tesfamichael, E. Wäckelgård, Angular solar absorptance and incident angle modifier of selective absorbers for solar thermal collectors, *Solar Energy* 68(4) (2000) 335-341.
- [114] Y.A. Çengel, M.A. Boles, *Thermodynamics : an engineering approach*, McGraw-Hill, New York, 2011.
- [115] T.L. Bergman, F.P. Incropera, D.P. DeWitt, A.S. Lavine, *Fundamentals of heat and mass transfer*, 7th ed., John Wiley and Sons 2011.
- [116] V. Gnielinski, On heat transfer in tubes, *International Journal of Heat and Mass Transfer* 63 (2013) 134-140.
- [117] R.W. Fox, A.T. McDonald, P.J. Pritchard, *Fluid mechanics*, 8th ed., John Wiley and Sons, Asia 2012.
- [118] J.R. Davis, *Alloy digest sourcebook: stainless steels*, ASM international 2000.
- [119] S.A. Kalogirou, A detailed thermal model of a parabolic trough collector receiver, *Energy* 48 (1) (2012) 298-306.
- [120] S. Song, M. Yovanovich, Correlation of thermal accommodation coefficient for engineering surfaces, *ASME HTD* 69 (1987) 107-116.
- [121] D.R. Lide, *CRC Handbook of Chemistry and Physics*, 12J204 (2012).
- [122] J.R. Howell, M.P. Mengüç, Radiative transfer configuration factor catalog: A listing of relations for common geometries, *Journal of Quantitative Spectroscopy and Radiative Transfer* 112 (5) (2011) 910-912.
- [123] V. Dudley, G. Kolb, M. Sloan, D. Kearney, SEGS LS2 solar collector—Test results, Report of Sandia National Laboratories, Report No. SANDIA94-1884 (1994).
- [124] Z. Tang, X.-P. Zhao, Z.-Y. Li, W.-Q. Tao, Multi-scale numerical analysis of flow and heat transfer for a parabolic trough collector, *International Journal of Heat and Mass Transfer* 106 (2017) 526-538.
- [125] N. Singh, S. Kaushik, R. Misra, Exergetic analysis of a solar thermal power system, *Renewable Energy* 19(1) (2000) 135-143.
- [126] R. Petela, Exergy analysis of the solar cylindrical-parabolic cooker, *Solar Energy* 79 (3) (2005) 221-233.
- [127] H. Transmission, by WH McAdams, McGraw-Hill Book Co., New York 214 (1942).
- [128] A. Suzuki, General theory of exergy-balance analysis and application to solar collectors, *Energy* 13 (2) (1988) 153-160.
- [129] K.B. Stolarsky, Generalizations of the logarithmic mean, *Mathematics Magazine* 48 (2) (1975) 87-92.
- [130] D. Zwillinger, *CRC standard mathematical tables and formulae*, CRC press 2002.

APPENDIX A: SURFACE AREAS

Figure 6.8 shows two surface areas regarding heat exchange by radiation heat transfer. The first reflector area S_{ref} is determined by the length of the parabolic arc from using coordinates of the end of the arc as [130]:

$$S_{ref} = \sqrt{4x_c^2 + y_c^2} + \frac{y_c^2}{2x_c^2} \ln \frac{2x_c + \sqrt{4x_c^2 + y_c^2}}{y_c} \quad (\text{A.1})$$

The second surface is the outer surface of the glass envelope. According to heat exchange, it can be divided into three parts. The first part is seen from only the sky, three unknowns x_a , y_a and y_b . It can also be determined from three relations: the proportional in a triangle, the equation of a circle and the equation of a line, respectively as:

$$\frac{x_c}{x_a} = \frac{y_b - y_c}{y_b - y_a} \quad (\text{A.2})$$

$$x_a^2 + (y_a - F)^2 = \left(\frac{d_5}{2}\right)^2 \quad (\text{A.3})$$

$$\frac{x_a}{\sqrt{\left(\frac{d_5}{2}\right)^2 - x_a^2}} = \frac{y_a - y_c}{x_c - x_a} \quad (\text{A.4})$$

The length of the circular arc between points a and a' is as follows:

$$S_{aa'} = d_5 \sin^{-1} \frac{2x_a}{d_5} \quad (\text{A.5})$$

The second part of the outer surface of glass is seen from only the reflector and the three unknowns x_n , y_n and y_s . This part can be determined from the three following relations:

$$\frac{x_c + x_n}{x_n} = \frac{y_n - y_c}{y_n - y_s} \quad (\text{A.6})$$

$$x_n^2 + (F - y_n)^2 = \left(\frac{d_5}{2}\right)^2 \quad (\text{A.7})$$

$$\frac{x_n}{\sqrt{\left(\frac{d_5}{2}\right)^2 - x_n^2}} = \frac{y_n - y_c}{x_c + x_n} \quad (\text{A.8})$$

The length of the circular arc between points n and n' is as:

$$S_{mi} = d_5 \sin^{-1} \frac{2x_n}{d_5} \quad (\text{A.9})$$

The right and left side of glass present the surface seen from the sky and reflector and can be determined as:

$$2S_{ai} = \pi d_5 - S_{aa} - S_{mi} \quad (\text{A.10})$$

VITA

Hayder Noori Mohammed Mohammed has received his PhD in Mechanical Engineering, Özyeğin University, Istanbul, Turkey in 2018, He received his BSc and MSc degrees in Mechanical Engineering from the University of Technology, Baghdad, Iraq in 1991 and 1995, respectively. From 1996 to 2009, he worked as lecturer in Higher Institute of Mechanical Occupations, Benghazi, Libya. After that, he worked at the University of Kerbala as an Assistant Lecturer before starting his Ph.D. study there, where he stayed from 2009 to 2013. Since 2013, he is working on his PhD thesis at the Center for Energy, Environment, and Economy (CEEE), Özyeğin University, Istanbul, Turkey under the supervision of Professor Dr. M. Pinar Mengüç. His research focuses on radiative heat transfer, and about the energy/exergy performance of concentrating solar power systems.

He has contributed to the EU FP7 BRICKER project as a member of CEEE, Özyeğin University during his Ph.D. study. This project was built with the help of the European Union at the campus of Adnan Menderes University, Aydin, Turkey.

He has published 2 papers in International Journal of Exergy, and has one conference paper. Also, he has two papers under review. As shown below.

Part	Paper name	Conference/Journal
Spectral Expression for Maximum Efficiency of Solar Radiation	Exergy Efficiency for Thermal Radiation Transfer	International Conference on Energy and Thermal Engineering: Istanbul 2017 (Accepted and Presented)
Spectral Radiative of Selective Coating for CSP Systems	Radiative Energy and Exergy Analyses of Spectrally-Selective Surfaces for CSP Systems	International Journal of Exergy (Vol. 27, No. 1, pp. 81-104, 2018)
Prediction Solar Radiation Exergy and Quality Performance	Solar Radiation Exergy and Quality Performance for Iraq and Turkey	International Journal of Exergy (Vol. 25, No. 4, pp. 364-385, 2018)
Radiative Exergy Performance Analyses of a CSP System	Radiative Exergy Performance Analyses of a CSP System	Energy Conversion and Management (Submitted in July 2018)